

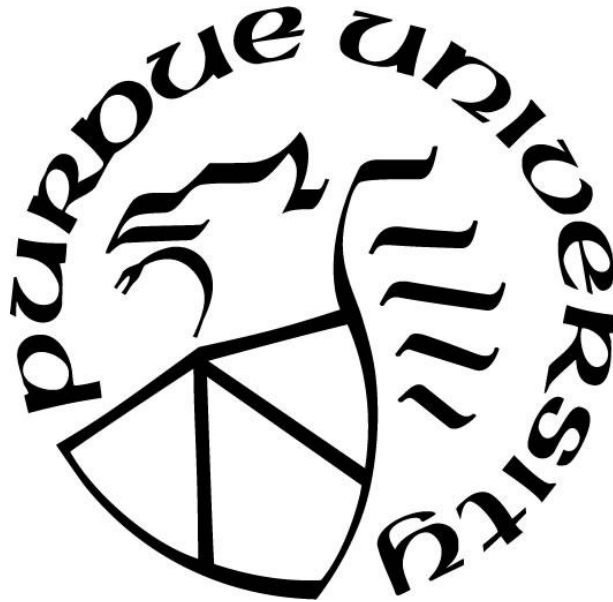
**MICROSTRUCTURAL INVESTIGATIONS OF SAMARIUM-DOPED  
ZIRCONIUM DIBORIDE FOR HYPERSONIC APPLICATIONS**

by  
**Anneliese Brenner**

**A Dissertation**

*Submitted to the Faculty of Purdue University  
In Partial Fulfillment of the Requirements for the degree of*

**Doctor of Philosophy**



School of Materials Engineering

West Lafayette, Indiana

May 2019

**THE PURDUE UNIVERSITY GRADUATE SCHOOL  
STATEMENT OF COMMITTEE APPROVAL**

Dr. Rodney Trice, Chair

Department of Materials Science and Engineering

Dr. Kevin Trumble

Department of Materials Science and Engineering

Dr. Wolfgang Reinheimer

Department of Materials Science and Engineering

Dr. Eric Kvam

Department of Materials Science and Engineering

**Approved by:**

Dr. David Bahr

Head of the Graduate Program

*This thesis is in dedication to: my dad James Laskowski, my husband Steven Brenner, my daughter Aurora, and baby number 2.*

## **ACKNOWLEDGMENTS**

I would like to acknowledge my advisor and committee members for helping and supporting me throughout these past four years, my lab mates Andrew Schlup and Jorge Ramirez-Valesco for their helpful conversations and assistance in sintering and ablation, my family for their support, and especially my husband for his support, tolerance, and never giving up on me. I would also like to gratefully acknowledge the financial support of Dr. Ali Sayir of the Airforce Office of Scientific Research (AFOSR Grant # FA9550-16-1-0039). Most importantly I could not have survived these past 4 years without the help from my Lord and Savior, Jesus Christ.

## TABLE OF CONTENTS

LIST OF TABLES .....	8
LIST OF FIGURES .....	9
NOMENCLATURE .....	12
ABSTRACT.....	13
1. INTRODUCTION .....	15
1.1 Motivation for Use of Ultra-High Temperature Ceramic as Leading-Edge Material .....	15
1.2 Importance of Emittance in Ultra-High Temperature Ceramics and Factors that Effect Emittance .....	17
1.3 Effect of Wavelength on Spectral Emittance.....	18
1.4 Effect of Surface Roughness and Porosity on Emittance Ultra-High Temperature Ceramics .....	18
1.5 Limitations of ZrB <sub>2</sub> /SiC Systems.....	21
1.6 Effect of Surface Roughness and Porosity on Ablation Performance Ultra-High Temperature Ceramics .....	23
1.7 Modifying ZrB <sub>2</sub> /SiC with Rare-Earth Oxides.....	24
1.8 Our Goal on how to Optimize Sm-Doped ZrB <sub>2</sub> /SiC .....	26
2. EXPERIMENTAL PROCEDURES .....	28
2.1 Suspension Preparation and Process for Spray Drying.....	28
2.2 Chemical Infiltration of Powder .....	28
2.3 Pressing and Sintering Sm-doped ZrB <sub>2</sub> /SiC Powders .....	29
2.4 Pressing and Solid-State Reaction Sintering of c <sub>1</sub> -Sm <sub>0.2</sub> Zr <sub>0.8</sub> O <sub>1.9</sub> .....	31
2.5 Polishing and Adding Surface Roughness to Sintered Billets .....	32
3. ANALYTICAL AND EXPERIMENTAL EQUIPMENT AND PROCEDURES .....	33
3.1 Microstructural and Phase Analysis.....	33
3.2 Density Evaluation of Billets .....	34
3.3 Oxyacetylene Ablation Tests .....	35
3.4 Spectral Emittance Testing .....	36
3.5 Linear Thermal Expansion Measurements .....	38

4. IN-SITU OXIDE SCALE INVESTIGATION OF SAMARIUM-DOPED ZIRCONIUM DIBORIDE/ SILICON CARBIDE BILLETS .....	39
4.1 Results.....	39
4.1.1 Pre-ablated Microstructure and Phase Assemblage.....	39
4.1.2 Weight Gain and Heating Profile as a Function of Ablation Time .....	41
4.1.3 Phase Make-up After Ablation .....	43
4.1.4 Microstructure Changes with Ablation.....	44
4.2 Discussion.....	47
4.2.1 First observation: Development of the Oxide Scale Morphology as a Function of Time .....	48
4.2.1.1 Post 10s of Ablation .....	48
4.2.1.2 Post 60s of Ablation .....	50
4.2.1.3 Post 300s of Ablation .....	51
4.2.2 Second Observation: Sm-doped Samples form SZO from $\text{Sm}_2\text{O}_3$ and $\text{ZrO}_2$ and Glass Transportation.....	54
4.3 Conclusion .....	55
5. MICROSTRUCTURAL EFFECTS ON ABLATION AND EMITTANCE BEHAVIOR OF SAMARIUM-DOPED ZIRCONIUM DIBORIDE/ SILICON CARBIDE CERAMICS .....	57
5.1 Results.....	57
5.1.1 As Sintered Microstructure and Phase Analysis.....	57
5.1.2 Post-ablation Properties of Sm-doped ZBS with Different Roughness and Porosities .....	61
5.1.2.1 Samples with Different Surface Roughness .....	61
5.1.2.2 Samples with Different Porosities .....	63
5.1.3 Post-laser Heated Microstructures of of Sm-Doped ZBS with Different Surface Roughness and Porosities .....	65
5.1.4 Spectral Emittance of Sm-doped ZBS with Different Surface Roughness and Porosities.....	68
5.2 Discussion.....	71
5.2.1 Increase in Surface Roughness and Porosity Results in Higher Surface Temperatures .....	71

5.2.2	Surface Roughness Does Not Make a Difference in Post-Ablation Topographical Microstructure Due to Glass Formation, but Does Affects Sm in Oxide Scale .....	73
5.2.3	Increasing Porosity Results in Glass Pools on Surface and Decrease in Sm-Depletion Region .....	74
5.2.4	Post Laser Heated Billets of Different Surface Roughnesses and Porosity Result in Same Microstructure .....	75
5.2.5	Spectral Emittance of Sm-ZBS with Different Surface Roughness and Porosities...	78
5.3	Conclusion .....	79
6.	FABRICATION AND ABLATION TESTING OF CUBIC-SAMARIUM(0.2) ZIRCONIUM(0.8) OXYGEN(1.9).....	81
6.1	Prior Studies on $c_1\text{-Sm}_{0.2}\text{Zr}_{0.8}\text{O}_{1.9}$ .....	81
6.2	Results.....	83
6.2.1	Post-Sintered Phases .....	83
6.2.2	Pre-Ablation Results .....	85
6.2.3	Post-Ablation Results and Discussion .....	87
6.3	Conclusion .....	91
7.	SUMMARY AND FUTURE WORK .....	93
7.1	Summary of Studies Presented .....	93
7.2	Suggestions for Future Work .....	95
	APPENDIX.....	97
	REFERENCES .....	98
	VITA .....	104
	PUBLICATIONS.....	105

## LIST OF TABLES

Table 2.1 Table of ramp rate, hold temperature, and hold time for SZO heated in a furnace .....	31
Table 2.2 Pre-tested billet naming convention, density, open porosity, and surface roughness. .	32
Table 3.1 Samples maximum temperature reached during laser heating. ....	37
Table 5.1 Measured densities, porosities, surface roughness of pre-heated billets and max temperatures reached during oxyacetylene ablation. ....	57
Table 5.2 Phases present in pre-ablated and post-laser-ablated billets as well as max temperature reached at each power condition.....	59
Table 6.1 Table showing ramp rate, hold temperature, hold time, and phases present after sintering for powders heated in a furnace in air.....	83

## LIST OF FIGURES

Figure 1.1 3D model of surface temperature experienced by leading edge at Mach 7. <sup>4</sup>	15
Figure 1.2 Surface energy balance of a leading-edge material. <sup>5</sup>	16
Figure 2.1 SEM images of a) undoped ZrB <sub>2</sub> /SiC spray dried powders and b) 5mol% Sm-doped ZrB <sub>2</sub> /SiC granules post sieving.	29
Figure 2.2 Green bodies of pressed Sm-doped ZBS sandwiched between SiC plates. A 250g graphite weight on top of the stack was for stability. Total billets in furnace was 14.	30
Figure 3.1 Raw atomic force microscopy images of the samples with different surface roughness and porosities.	34
Figure 3.2 Set up of the oxyacetylene ablation rig.	35
Figure 3.3 Experimental set-up of RHINO lab at AFRL.	36
Figure 3.4 Schematic of where billet was heated and where the spectral radiance was collected. Surface features of sample were on the side where spectral radiance was collected.	36
Figure 4.1 SEM micrographs at different magnifications for pre-ablated billets, 10s post ablated, 60s post ablated, and 300s post ablated. The magnified excerpt image in b) shows ZrB <sub>2</sub> grains (red) surrounded by SmB <sub>2</sub> C <sub>2</sub> matrix (yellow) with patches of SiC (purple). Excerpt BSE image in c) shows the magnified surface of the convectional cell containing oxide islands dispersed in a glassy phase.	40
Figure 4.2 XRD of a) pre- and post-ablated billets after b)10s, c) 60s, and d) 300s.	41
Figure 4.3 Time vs. temperature graph of ablated samples 10s, 60s, and 300s. Optical images are a) before ablation, b) 10s post ablation, c) 60s post ablation, and d) 300s post ablation.	43
Figure 4.4 BSE cross-sectional images of a) 10s ablated, c) 60s ablated, and c) 300s ablated billets. Boxed areas correspond to higher magnified images (images b, d, and f) showing crystalline regions and an intergranular glassy phase.	45
Figure 4.5 Cross-sectional EDS analysis of billets after 10s, 60s, and 300s of ablation.	47
Figure 4.6 EDS analysis post 10s of ablation in Zone 1 of a convectional cell that contains an oxidizing ZrB <sub>2</sub> grain as well as the formation of the intergranular Sm-doped silicate glassy phase.	50
Figure 4.7 EDS analysis of post 300s of ablation of a) round dendrites, b) higher magnification of a), c) oxide island region, and d) large uniform crystalline phase with dendrites on top.	52
Figure 5.1 SEM images of pre- and post-ablated billet surfaces D1R1, D1R2, and D1R3.	58
Figure 5.2 SEM images of of pre- ablated cross-sections of a) D1R1, b) D1R2, and c) D3R1 as well as post-ablated billet surfaces d) D1R1, e) D2R1, and f) D3R1.	60

Figure 5.3 XRD of a) pre-ablated billets, b) post-ablated billets of different surface roughness, and c) post-ablated billets of different density percent. ....	62
Figure 5.4 EDS analysis of D1R1, D2R1, and D3R1.....	63
Figure 5.5 EDS analysis of D1R1, D2R1, and D3R1.....	64
Figure 5.6 SEM SE micrographs of post-laser ablated a) D1R2, b)D1R3, c)D2R1, and d)D3R1. ....	65
Figure 5.7 XRD of pre- and post-ablated billet surfaces of D1R2.....	66
Figure 5.8 EDS analysis of D1R1 after 60s of holding at 900W. Table shows the compositions of the crystalline and amorphous phases. ....	67
Figure 5.9 Spectrometer side where radiance data was collected and b) laser ablated side where sample was heated. ....	68
Figure 5.10 Emittance vs wavelength graphs of a) different surface roughness at 2100°C, b) different porosities at 2100°C, c) different surface roughness at 1600°C, and d) different porosities at 1600°C.....	69
Figure 5.11 Emittance as a function of wavelength at different time intervals for D1R2.....	70
Figure 5.12 Emittance as a function of temperature for samples of a) different surface roughness and b) porosities. ....	71
Figure 5.13 ZrO <sub>2</sub> -Sm <sub>2</sub> O <sub>3</sub> phase diagram. <sup>53</sup> C <sub>1</sub> -Sm <sub>0.2</sub> Zr <sub>0.3</sub> O <sub>1.9</sub> is denoted by C <sub>1</sub> in phase diagram. Temperature on horizontal axis is in °C. ....	76
Figure 6.1 XRD analysis of Sm <sub>x</sub> Zr <sub>1-x</sub> O <sub>2x-1</sub> , where x is the samarium concentration of x=1 to x=5. <sub>63</sub> .....	82
Figure 6.2 SEM-BSE images of samples with different hold times at 1700°C. Dark cloudy regions are debris from the furnace and not part of the actual sample. ....	84
Figure 6.3 Optical images showing a) pre-ablation and b) post-ablation SZO billets. Differences in coloration are due to camera lighting.....	85
Figure 6.4 SEM-BSE cross-sectional images of the billet. EDS scans reveal small grain pockets are rich in Zr and lacking Sm. ....	86
Figure 6.5 XRD patterns of the billet a) pre-ablated and b) post ablated. All peaks correspond to SZO. ....	86
Figure 6.6 SEM images showing a) pre-ablation microstructure, b) higher magnification of a), c) post-ablation microstructure, and d) higher magnification of c). ....	87
Figure 6.7 EM-BSE image of the cross-section of the post-ablated SZO billet.....	88
Figure 6.8 CTE graph of the samples conducted at Purdue compared to those performed by Liu. et. al. <sup>63</sup> .....	90

Figure 6.9 Depiction of how the sample was clamped and heated in the ablation rig. Due to wear of the graphite plates, sample was clamped tighter on the front of the sample (torch side)..... 91

## NOMENCLATURE

<u>List of Abbreviations</u>		<u>Variables</u>	
AFM	atomic force microscopy	$\varepsilon$	emittance
EDS	electron dispersive spectroscopy	$\rho$	density
CTE	coefficient of thermal expansion	$\mu$	micron
g	grams	$\theta$	angle
LTE	linear thermal expansion	$q_{\text{chem}}$	chemical heat flux
mm	milimeter	$q_{\text{conv}}$	convection heat flux
REO	rare-earth oxide	$q$	heat flux
rpm	rotation per minute	$A$	surface area
s	second(s)	$c_p$	specific heat
sccm	standard cubic centimeter	$D(T)$	thermal diffusivity
SEM	scanning electron microscopy	$K_{\text{th}}(T)$	thermal conductivity
slpm	standard liter per minute	$L_0$	initial length
Sm	samarium	$L_1$	final length
SZO	$\text{c}_1\text{-Sm}_{0.2}\text{Zr}_{0.8}\text{O}_{1.9}$	$T$	temperature
TBC	thermal barrier coating	$T_{\infty}$	surrounding temperature
TEM	transmission electron microscopy	$T_o$	ambient temperature
TGA	thermogravimetric analysis	$T_w$	wall temperature
UHTC	ultra-high temperature ceramic	$\Delta T$	change in temperature
XRD	ray diffraction	$\Delta L$	length difference
YSZ	yttria stabilized zirconia	$\sigma$	Stefan-Boltzmann constant
ZBS	$\text{ZrB}_2/\text{SiC}$		

## ABSTRACT

Author: Brenner, Anneliese, E. PhD

Institution: Purdue University

Degree Received: May 2019

Title: Microstructural Investigations of Sm-Doped ZrB<sub>2</sub> for Hypersonic Applications

Committee Chair: Rodney Trice

Sharp leading edges required for hypersonic vehicles improve the maneuverability as well as reduce aerodynamic drag. However, due to the sharp design, increased surface temperatures require materials that can withstand these extreme conditions. Ultra-high temperature ceramics are a material group being considered for the leading-edge material, specifically ZrB<sub>2</sub>/SiC (ZBS) which has a high thermal shock resistance, melting temperature, and thermal conductivity. Studies done by Tan et. al. has shown that adding samarium (Sm) as a dopant to ZBS has an emittance of 0.9 at 1600°C and develop oxide scales that have excellent ablation performance. However, it remained unknown how the Sm doped oxide scale formed as well as how the emittance and ablation performance are affected by the microstructure. This study investigates the oxide scale development of 3 mol% doped Sm-ZBS billets as well as how differences in microstructure affect the emittance and ablation performance. Samples were prepared via chemical infiltration of samarium nitrate into spray-dried powders of 80 vol.% ZrB<sub>2</sub>/20 vol.% SiC; powders were then pressed into billets and pressureless sintered. Samples cut and polished from these billets were then oxidized for 10, 60, or 300 s, respectively, using an oxyacetylene torch. X-ray diffraction was used to determine the sequence of oxidation of Sm-ZBS, beginning with the formation of ZrO<sub>2</sub> and Sm<sub>2</sub>O<sub>3</sub>. The final oxide scale was determined to be c<sub>1</sub>-Sm<sub>0.2</sub>Zr<sub>0.8</sub>O<sub>1.9</sub>, with a melting temperature exceeding 2500°C. SEM and EDS were also used to investigate the microstructural formation that occurs from the bursting of convection cells. Samples with different microstructures

revealed similar topographical microstructures post-ablation due to the sequence of the oxide formation. However, samples with rougher surfaces and higher porosities had a higher concentration of trapped glass in the cross-sectional oxide scale. It was also found that due to differences in heating the sample during emittance testing compared to ablation testing, the oxide developed was identical for all the samples. It was also found that variances in microstructure had no effect on the spectral emittance of Sm-ZBS at ultra-high temperatures. The fabrication of  $c_1$ - $\text{Sm}_{0.2}\text{Zr}_{0.8}\text{O}_{1.9}$  (SZO) as a bulk billet was also investigated to use as a thermal barrier coating (TBC) in replacement of Sm-ZBS.

## 1. INTRODUCTION

### 1.1 Motivation for Use of Ultra-High Temperature Ceramic as Leading-Edge Material

Sharp leading-edge designs for hypersonic vehicles improve performance by reducing aerodynamic drag as well as improve maneuverability. These leading-edge systems are required to operate at ultra-high temperatures in extreme environments where they must withstand corrosion, high chemical reactivity, and high heat flux to name a few.<sup>2</sup> However, sharp edges lead to increased convective heating due to the high enthalpy bow shock layer resulting in temperatures exceeding 2000°C.<sup>1,3</sup> It can be seen in Figure 1.1 the leading edge of a hypersonic vehicle going Mach 7 can get to ~2700K compared to the rest of the system which remains significantly cooler. Just behind the leading edge the temperature reaches ~1900K.<sup>4</sup>

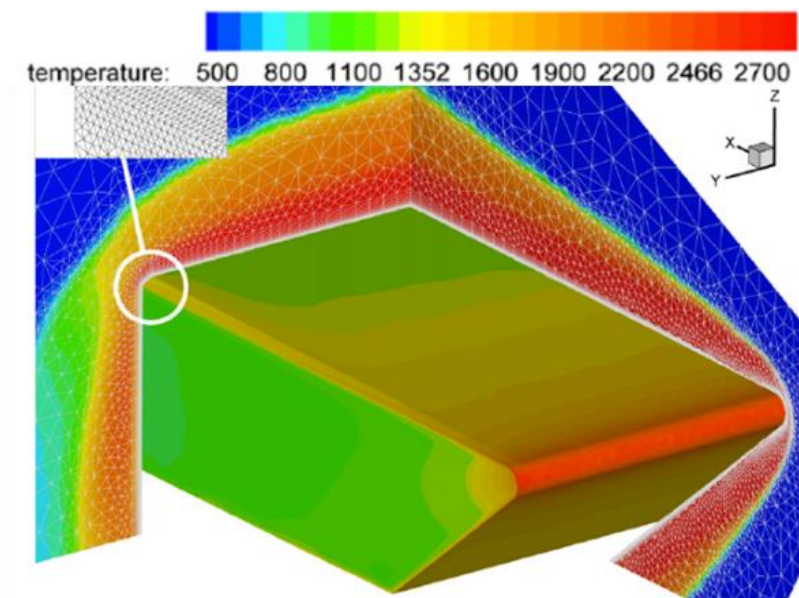


**Figure 1.1 3D model of surface temperature experienced by leading edge at Mach 7.**<sup>4</sup>

The system is also heated through chemical heating which arises from the recombination of dissociated air molecules (such as  $O_2$  and  $N_2$ ) on the surface. The dissociation of air molecules

is known to happen at Mach 5 and above.<sup>5</sup> Figure 1.2 illustrates the thermodynamic heat transfer balance of heating and cooling of the leading-edge system. The system heats through convective heating and chemical heating, as described previously, while it cools itself through conduction and radiation. While the material property thermal conductivity helps distribute the heat away from the tip of the leading edge to cool the system, the radiance cools the system by re-radiating heat back out to the environment. The material property relating to the radiance is emissivity ( $\epsilon$ ).<sup>5</sup>

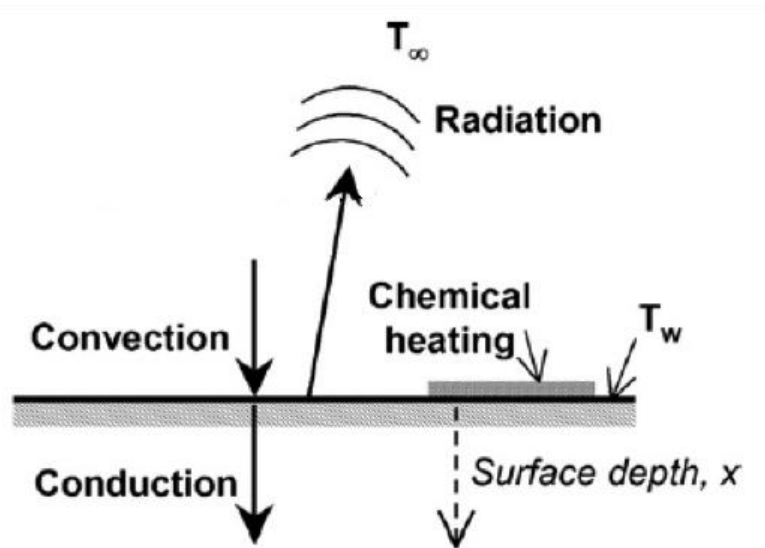


**Figure 1.2 Surface energy balance of a leading-edge material.**<sup>5</sup>

To survive these extreme conditions, the material for the leading edge must have a high thermal conductivity, thermal shock resistance, emittance, and melting temperature.<sup>5</sup> Ultra-high temperature ceramics (UHTC), such as  $\text{HfB}_2$ ,  $\text{ZrB}_2$ ,  $\text{SiC}$ ,  $\text{TaC}$ , and  $\text{ZrN}$ , are among the materials being considered for leading edges because of their high melting temperature. In specific  $\text{ZrB}_2$  is being considered which has a high melting point, thermal shock resistance, and thermal conductivity at  $1500^\circ\text{C}$  and above.<sup>2,3,5</sup>

## 1.2 Importance of Emittance in Ultra-High Temperature Ceramics and Factors that Effect Emittance

Emissivity is defined as the ratio of the total energy radiated from a material and a black body material at the same temperature. A black body material is one that absorbs and emits all energy and has an emittance equal to 1.<sup>9,10</sup> However, most materials are grey bodies and have emittances less than 1.<sup>9</sup> Emissivity is usually considered a fundamental property of optically polished materials. If the material has a rough surface and/or porosity, then the emissivity is considered an emittance of that sample.<sup>11</sup>

Emittance depends on the emissivity of a material, surface structure, and the surface temperature which in turn can be influenced by wavelength and surface parameters.<sup>7,8</sup> According to Avdoshenko and Strachan<sup>12</sup> in a modeling study on UHTC, emissivity of these materials also is dependent on point defects, coating thickness, ionic state, and f-shell states besides surface structure at high temperatures. Emissivity is not purely an intrinsic property; it is dependent on the structures and surface state.<sup>13</sup> According to Kirchoff's law, for a given wavelength and temperature we can assume the emissivity is equal to the absorption.<sup>7</sup> For our purposes it is assumed the emissivity is equal to the absorption.

As mentioned in Section 1.1, a leading edge is cooled through material properties of both thermal conductivity and emittance. Although thermal conductivity is important, emittance can play just as critical of a role in the cooling of a leading-edge system.<sup>5</sup> It has also been stated by Guzzoni<sup>6</sup> and Alfano et. al.<sup>7</sup> that radiation heat transfer is the only method for heating and cooling in space application making it an important material property to consider. As the emittance is increased there is a significant decrease in the surface temperature of the material as suggested by Glass<sup>6</sup> who assumes that if the thermal conductivity is 0 for a material.

### **1.3 Effect of Wavelength on Spectral Emittance**

One factor that can affect the emittance of a material is the wavelength. It is affected by the fact that an element on the surface radiates in all directions, however more so depending on the temperature and wavelength. Any radiation emitted is continually varying as wavelength is changed and the magnitude of emitted radiation increases with increasing temperature.<sup>9,15</sup> At high temperatures, the atoms in the material of interest are vibrating. The sum of the directions of vibration affect the absorbance of the material. At thermal equilibrium, the absorbance is equal to the emittance according to Kirchhoff's Law. The vibrational direction also is affected by the wavelength. At wavelengths in the  $\sim 1\text{-}10\ \mu\text{m}$  range is the sum of the directions of vibrations. As some wavelengths activate the more or less vibrational directions, the absorbance follows the same way. Therefore, in emittance vs. wavelength graphs we see a jagged pattern, hinting at the sum of vibrational directions being activated. However, when larger wavelengths are reached, the sum of the vibrations is considered to be almost 1, increasing the absorbance. At these larger wavelengths the material acts similar to a black body reaching emittances of  $\sim 1$ .<sup>67</sup>

### **1.4 Effect of Surface Roughness and Porosity on Emittance Ultra-High Temperature Ceramics**

As mentioned in Section 1.2, surface roughness and porosity can affect the emittance of ceramics. The emittance has the likelihood to be increased by porosity and surface roughness by increasing the area for absorption to occur from the radiation being scattered by the slopes and tips. A higher absorption leads to higher emittance. However, if there is too much porosity or surface roughness, then there is less material for absorption to occur decreasing the emittance.<sup>14,15</sup> Research on how porosity and surface roughness affect emittance of UHTC materials has been

inconclusive. In a study done on C/SiC composites, an increase in porosity was found to decrease the emittance of the material up to 1600°C as seen in Figure 1.3a.<sup>14</sup>

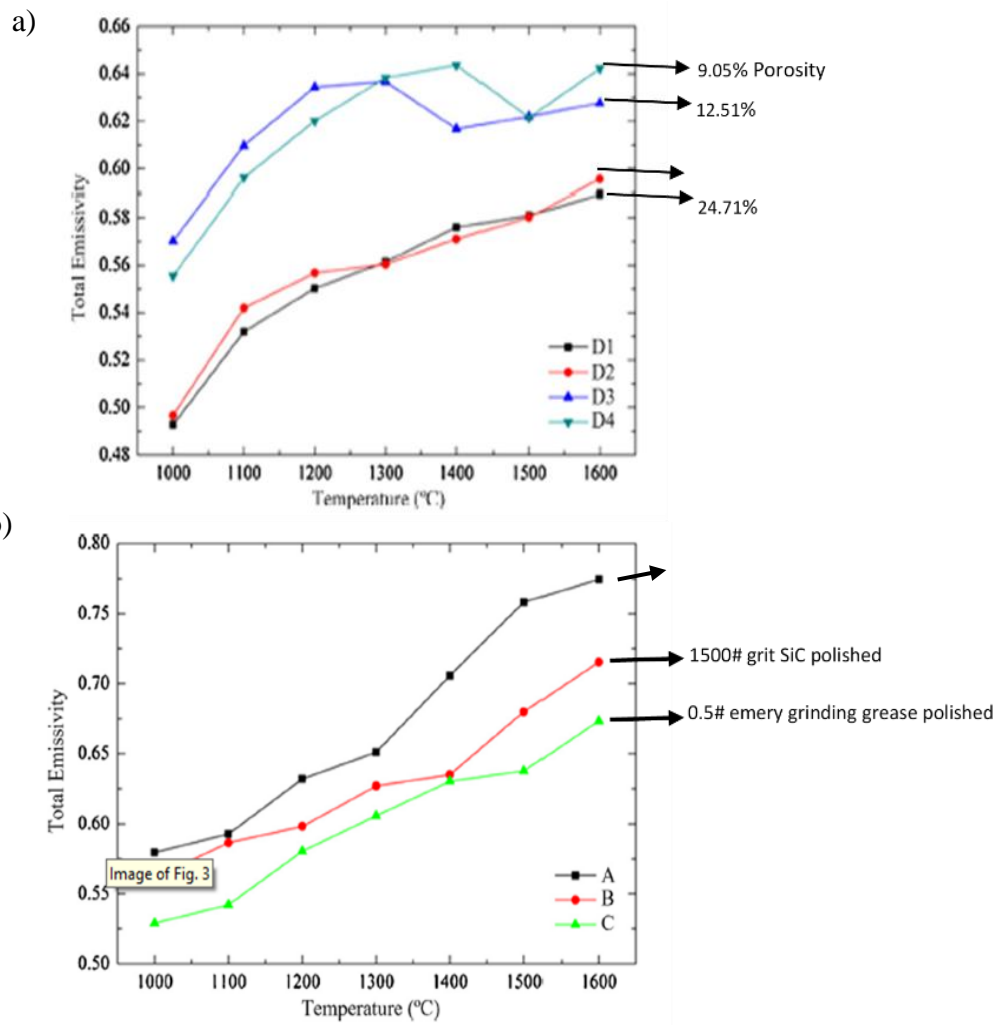


**Figure 1.3 Total Emissivity as a function of temperature for a) different porosities and b) different surface roughness of C/SiC composites.<sup>14</sup>**

It can be clearly seen that as porosity is increased, emittance overall decreased. However, in the same study an increase in surface roughness was found to increase the emittance.<sup>14</sup> It is clear in Figure 1.3b that as surface roughness increased (indicated by the grit number used to polish) the emittance increased. In a similar study done on ZrB<sub>2</sub>, HfB<sub>2</sub>, and HfC the porous ceramics (denoted

by p) behaved with a better emittance as a function of temperature up to 1800°C as seen in Figure 1.4.<sup>16</sup> This was also the case for  $ZrB_2$  and  $ZrO_2$  in a spectral emittance study performed at 1500°C in the 1000-6500nm ( $1\mu\text{m}$ - $6.5\mu\text{m}$ ) range.<sup>17</sup>

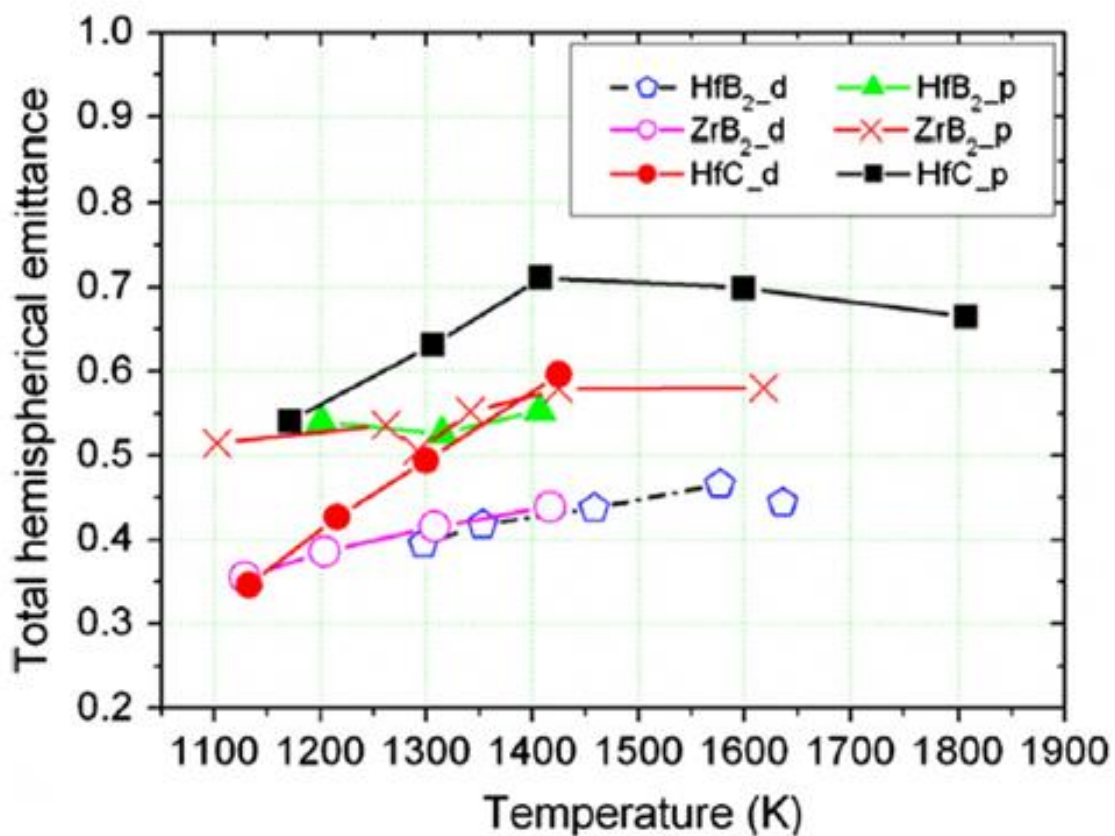
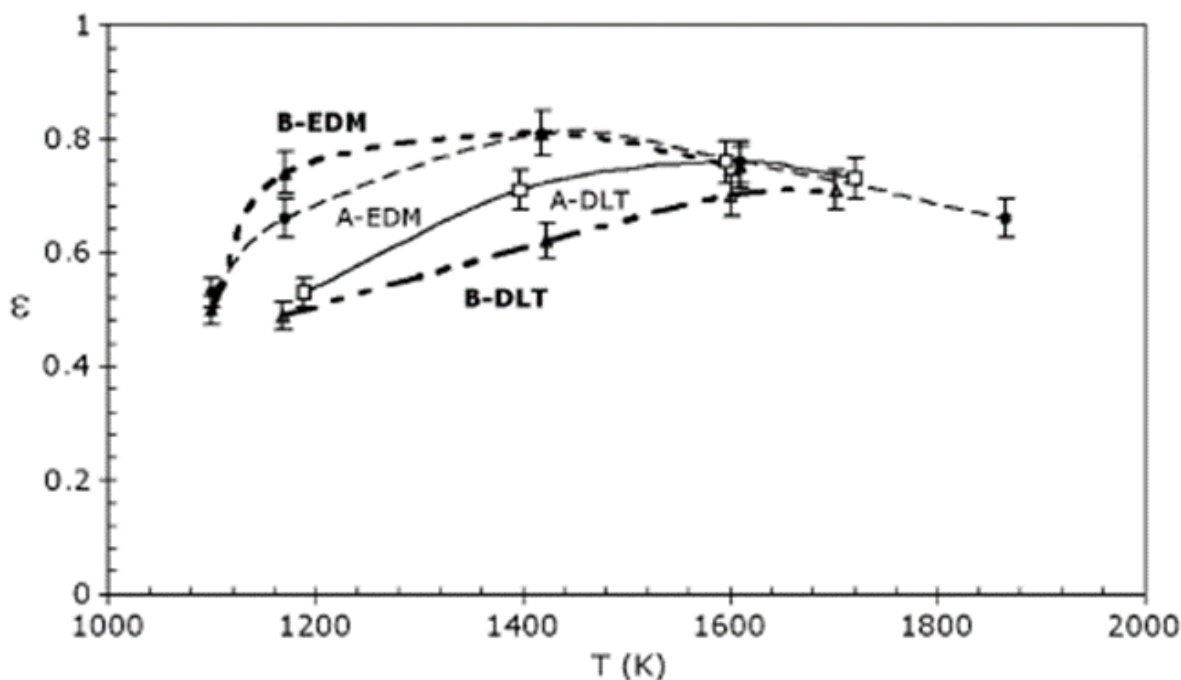


Figure 1.4 Total hemispherical emittance as a function of temperature for  $ZrB_2$ ,  $HfB_2$ , and  $HfC$  that are dense (d) and porous (p).<sup>16</sup>

However, for other UHTC materials, the opposite was found. McMahon<sup>6</sup> stated that for rare earth oxides (such as  $\text{Sm}_2\text{O}_3$  and  $\text{Tm}_2\text{O}_3$ ), surface roughness had no effect on the emittance of the samples. This was also the conclusion of Scattia et. al.<sup>17</sup> for  $\text{ZrB}_2/\text{SiC}$  and  $\text{HfB}_2/\text{ZrB}_2/\text{SiC}$  ceramics. The study concluded that heating above  $1500^\circ\text{C}$  the surface roughness had no effect on emittance as seen in Figure 1.5. However, below  $1600^\circ\text{C}$ , those that were electron discharged machined (EDM), which had the highest surface roughness, behaved with a higher emittance than diamond tool machined (DM) with a lower surface roughness.<sup>16</sup>



**Figure 1.5** Emissivity values for  $\text{ZrB}_2/\text{SiC}$  (A) and  $\text{ZrB}_2/\text{SiC}/\text{HfB}_2$  (B) materials that have been roughened with electrical discharge machining (EDM) and diamond tool machining (DLT. Surface roughness' are 0.58, 0.14, 0.98, and 0.14 for A-EDM, A-DLT, B-EDM, and B-DLT respectively<sup>11</sup> The bold lines are material B while the light lines are material A.<sup>18</sup>

### 1.5 Limitations of $\text{ZrB}_2/\text{SiC}$ Systems

Although promising,  $\text{ZrB}_2$  oxidizes to porous  $\text{ZrO}_2$  which leads to deeper oxygen penetration of the leading-edge material instead of acting as a protecting oxide layer. This transition leads to

spallation of the material. The addition of ~20-30 vol% SiC to ZrB<sub>2</sub> (ZBS) forms a protective oxide layer of silica (SiO<sub>2</sub>) on the surface which extends the maximum operation temperature of ZrB<sub>2</sub> to ~1600°C.<sup>18</sup> A diagram of how ZBS oxidizes in a furnace is illustrated in Figure 1.6.<sup>18</sup> At room temperature (RT)-700°C the ZBS system remains unoxidized as seen in Figure 1.6.a. At ~700°C, ZrB<sub>2</sub> starts to oxidize to crystalline ZrO<sub>2</sub> and B<sub>2</sub>O<sub>3</sub> glass which acts as a protectant on the surface from further oxidation of the ZBS as seen in Figure 1.3.b. As the B<sub>2</sub>O<sub>3</sub> is evaporated, it is replenished with more from beneath the surface. This occurs from the expansion of ZrB<sub>2</sub> to ZrO<sub>2</sub>, which forces the glass through pores and in between ZrO<sub>2</sub> grains. After 1100°C up to 1400°C, the B<sub>2</sub>O<sub>3</sub> starts to volatilize rapidly and the SiC begins to react with oxygen and form SiO<sub>2</sub> glass. The SiO<sub>2</sub> also reacts with the B<sub>2</sub>O<sub>3</sub> to form a borosilicate glass which has a higher viscosity and helps protect the underlying ZBS from further oxygen penetration as seen in Figure 1.6.c. Dissolved ZrO<sub>2</sub> is also present in the borosilicate glass, helping to increase the viscosity. As the glass evaporates, the ZrO<sub>2</sub> precipitates out and eventually grows into larger grains.<sup>18</sup> Above 1400°C, the volatilization of B<sub>2</sub>O<sub>3</sub> inhibits it from acting as a protective phase and SiO<sub>2</sub> becomes the only protectant in glass form. At these temperatures the active oxidation of SiC to SiO<sub>2</sub> progresses to form a SiC depletion region as shown in Figure 1.6.d. At 1600°C SiO<sub>2</sub> becomes increasingly volatile, exposing the porous ZrO<sub>2</sub> leading to further oxygen penetration.<sup>13</sup> Although ZBS has shown promising results, 1600°C is far from operating successfully at 2000°C.

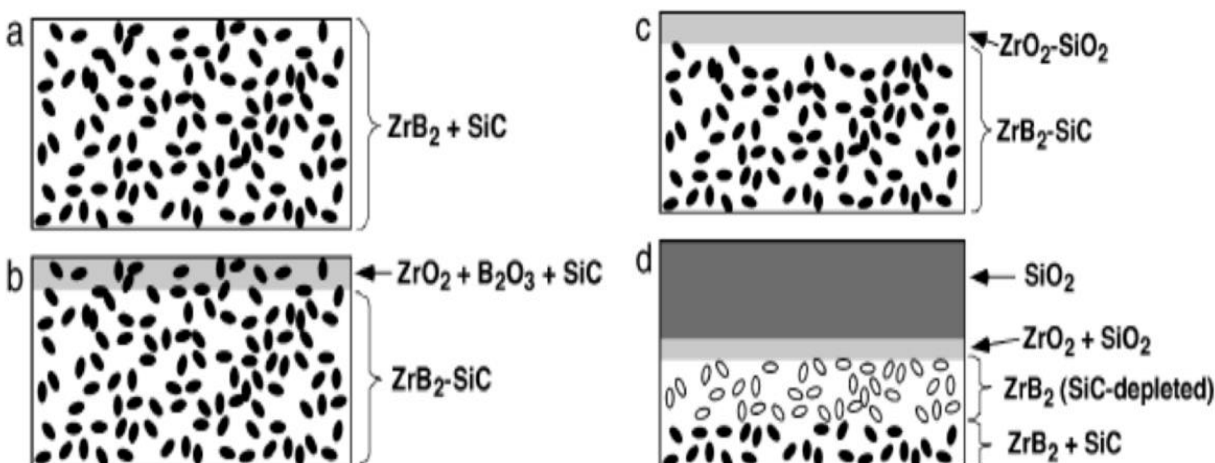


**Figure 1.6** Schematic of the oxidation of ZrB<sub>2</sub>/SiC as a function of temperature. At room temperature a), 700°C-1100°C b), 1100°C-1400°C c), and 1400°C-1600°C.<sup>18</sup>

### 1.6 Effect of Surface Roughness and Porosity on Ablation Performance Ultra-High Temperature Ceramics

Little research has been done in how UHTC ablation performance, with regards to surface oxide scale, is affected by surface roughness and porosity.<sup>20-22</sup> Studies performed by Li et. al.<sup>20,21</sup> on C-C/ZrC and ZBS/C-C/ZrC ablated above 2000°C in an oxy-acetylene rig have shown that samples with lower porosity result in better ablation performance resulting from a denser oxide scale. In another study on porous laser-ablated ZBS, the porous sample resulted in a thin silica glassy layer that acted as a protectant on top of the ZrO<sub>2</sub>.<sup>22</sup> This suggests that porosity had little effect on the ablation performance.

The effect of surface roughness on UHTC thermal barrier coatings (TBC) ablation performance remains a mystery. To the authors knowledge there have been none to date. However, there have been a few studies regarding how surface roughness affects the surface temperature and turbulence during hypersonic flight. As Mach number increases, the average surface roughness a leading edge can tolerate before inducing turbulent conditions decreases.<sup>23,25</sup> For hypersonic

conditions leading edges with smooth features are ideal as they are designed for laminar flow. Surface roughness has the potential to trip the boundary layer flow causing turbulence.<sup>1,23</sup> This in turn increases the temperature the surface experiences.<sup>25</sup> Rostamy et. al.<sup>26</sup> measured wall jets on both rough and smooth surfaces and found that having a roughened surface increases the skin friction from 15%-30%. And although surface roughness on a leading edge at hypersonic speeds have little to no effect on flow field in form of heat flux which can also increase surface temperature, increase in heat signatures relating to vortical structures in boundary layer are seen.<sup>26,28</sup> The same reasoning can also be applied to lower densities. Lowering the density increases the porosity, which also increases the surface roughness.

### **1.7 Modifying ZrB<sub>2</sub>/SiC with Rare-Earth Oxides**

Studies done by McMahon and Wilder<sup>12</sup> have shown that Samarium (Sm) and Thulium (Tm) show high emittances in the visible wavelength range. To maximize the emittance of ZBS, studies performed by Tan et. al.<sup>29-32</sup> have shown that adding samarium (Sm) dopant to the ZBS system increases the emittance as well as improves ablation performance compared to ceramics comprised only of ZBS. The Sm dopant improved ablation performance by forming a stable oxide scale of  $c_1\text{-Sm}_{0.2}\text{Zr}_{0.8}\text{O}_{1.9}$  (SZO), which has a melting point above 2500°C, making it capable of withstanding extreme temperature conditions during hypersonic flight.<sup>30,31</sup> In a study where the total hemispherical emittance was tested on a 5 mol% Sm-doped ZBS plasma sprayed coating, it

was found to have an emittance of 0.9 at 1600°C.<sup>29</sup> The same study also showed that all the samples tested with Sm performed with higher emittances than un-doped ZBS, as depicted in Figure 1.7.

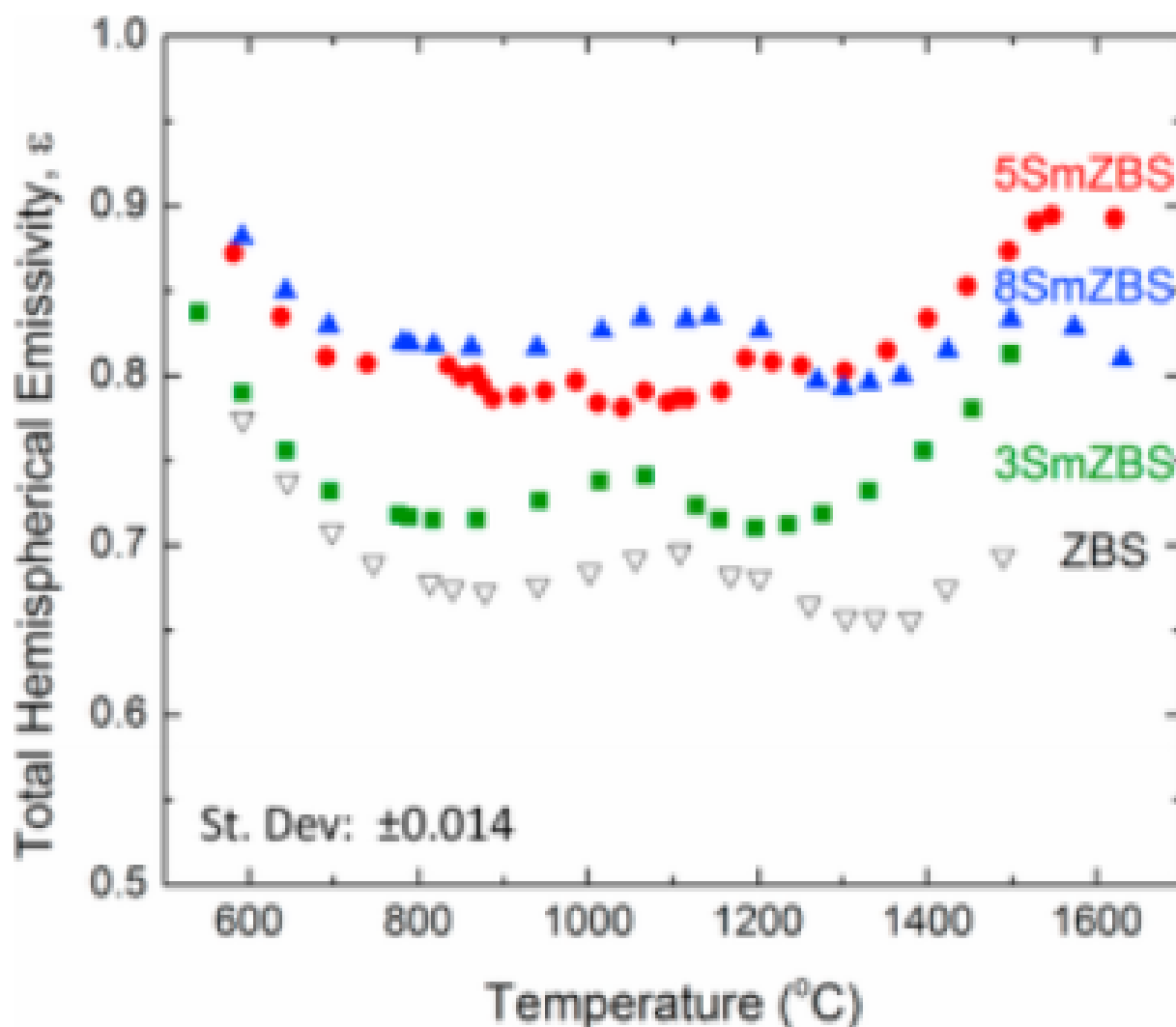


**Figure 1.7 Total hemispherical emissivity vs temperature graph of ZBS samples doped with and without Sm.<sup>11</sup>**

This increase in total hemispherical emittance is believed to be due to localized  $f$ -shell states of the  $\text{Sm}^{+3}$  making it have a high absorption in the visible wavelength region.<sup>11</sup>  $\text{Tm}^{+3}$  is expected to behave the same way. Some results shown by Tan et. al. has indicated this may be the case as seen where Tm dopant displayed a similar emittance to Sm.<sup>32</sup>

It was also found by Tan et. al.<sup>31</sup> that the optimal Sm concentration to add to ZBS was 5mol%, as seen in Figure 1.7. However, with increasing Sm concentration, differences in microstructure are apparent, as seen in Figure 1.8.<sup>30</sup> As described in Section 1.2 and 1.3, microstructure can affect the emittance of materials.

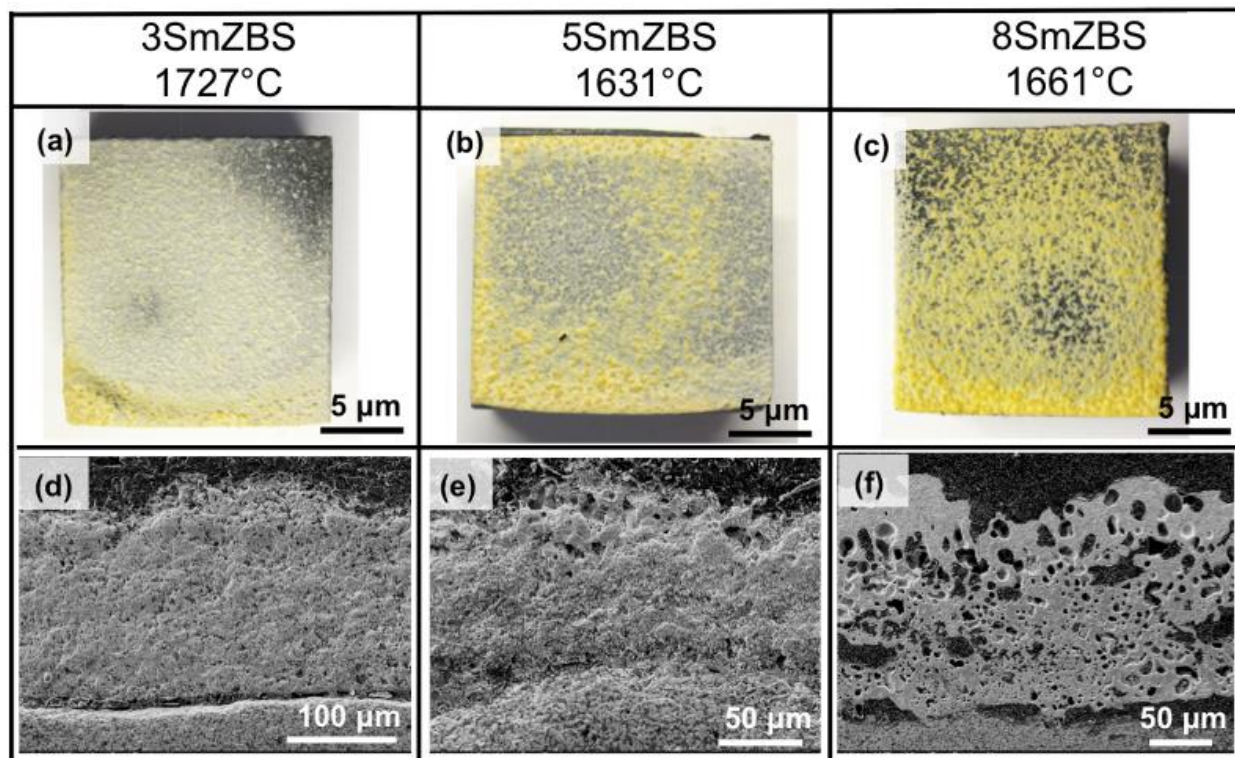


**Figure 1.8** Optical images for post ablated a) 3SmZBS, b) 5SmZBS, and c) 8SmZBS. SEM images for post ablated microstructural cross-sections of a) 3SmZBS, b) 5SmZBS, and c) 8SmZBS.<sup>30</sup>

### 1.8 Our Goal on how to Optimize Sm-Doped ZrB<sub>2</sub>/SiC

In the SmZBS system (and for most UHTC), it is unknown how microstructure affects both the emittance and ablation performance. Tan et. al. found that there were differences in emittances with different Sm concentrations (Figure 1.9); however, their beginning microstructure was also different. This leaves the question of how the microstructure affecting the emittance and ablation performance at ultra-high temperatures. In Figure 1.8, as Sm concentration increases, the size and

number of the pores also increases, indicating there may be an increase in the release of a volatile byproduct. With the formation of volatile products, the studies also left the question of why we need Si in the system and would it be possible to just form the SZO structure as a TBC. Thus, these questions were deemed important to investigate. In this study, the oxide scale of 3mol% Sm-doped ZBS billets were ablated using an oxyacetylene torch for 10s, 60s, and 300s in order to determine how the oxide scale develops. Different surface finishes, porosities, and Tm concentrations were also ablated for 60s using an oxyacetylene torch to investigate how the microstructure is affecting the ablation performance. The samples emittances were also tested at the RHINO lab at the Air Force Research Laboratories using a laser heating set-up in air. Lastly the formation of pure SZO was also investigated to determine if it would make a good TBC.

## 2. EXPERIMENTAL PROCEDURES

The following chapter describes the technique used in preparing the Sm-doped ZrB<sub>2</sub>/SiC billets. Calculations for chemical dopant concentration were found using same method as Tan in previous samarium-doped studies.<sup>32</sup>

### 2.1 Suspension Preparation and Process for Spray Drying

The purpose of spray drying was to create large, porous agglomerates of ZrB<sub>2</sub> and SiC in preparation for doping with Sm. Spray-dried granules were prepared from a suspension that consisted of 80 vol.% ZrB<sub>2</sub> (3–5 μm, Grade A, HC Starck, Munich, Germany), 20 vol.% α-SiC (1.4 μm, Grade UF-05, HC Starck, Munich, Germany), 0.4 wt.% dispersant (Darvan 821A, R.T. Vanderbilt Company, Inc., Norwalk, USA), 2 wt.% PVA binder (Celvol 203, Celanese Corporation, Dallas, USA) and DI water. Spray drying was performed by Arch Instant Spray Drying Services, Brunswick, GA using a lab spray dryer (APV Anhydro Model S1, Anhydro Inc, Soeborg, Denmark) with the atomizer rotating at ~30,000 rpm. The inlet temperature used was 250°C with an outlet temperature of ~100°C-110°C. All spray drying was performed in air. The resulting average spray-dried particle size was ~50 μm.

### 2.2 Chemical Infiltration of Powder

A chemical infiltration method was used to dope the ZBS spray dried powder with Sm and Tm dopant. In this process, 10 mol.% samarium nitrate hexahydrate (99.9% pure Sm(NO<sub>3</sub>)<sub>3</sub>·6H<sub>2</sub>O, Sigma-Aldrich, St. Louis, USA) was dissolved into isopropyl alcohol. This comes to 11.7 wt% or ~3.5 mol% (35% of the actual 10mol%) of actual Sm<sup>+3</sup> incorporated into the granules as the other 6.5 mol% contain the nitrate and hydrate. The resulting solution was then infiltrated into the porous

spray-dried  $\text{ZrB}_2/\text{SiC}$  granules via rotating on a ball mill for 2 hrs. Next, the solvent was removed via a rotary evaporator (BM 200, Yamato Scientific America Inc., Santa Clara, USA) at  $100^\circ\text{C}$  under high pressure. This powder was heated at  $400^\circ\text{C}$  in air for an hour to remove residual moisture and nitrates. Tan et al.<sup>30</sup> showed that below  $400^\circ\text{C}$  both the ZBS and the Sm-doped powders did not have any weight gain. As the normalized weight gain was approximately zero below  $400^\circ\text{C}$ , it suggests that the oxidation of the powders has little effect during the heat treatment at  $400^\circ\text{C}$ . The first weight gain inflections start near  $600^\circ\text{C}$  due to the oxidation of  $\text{ZrB}_2$  to form  $m\text{-ZrO}_2$  and  $\text{B}_2\text{O}_3$  glass.<sup>30</sup> Subsequently, the dried mixture was crushed and sieved using a 325 mesh sieve ( $45\ \mu\text{m}$  aperture) to eliminate large agglomerates. Powders before and after doping can be seen in Figure 2.1.

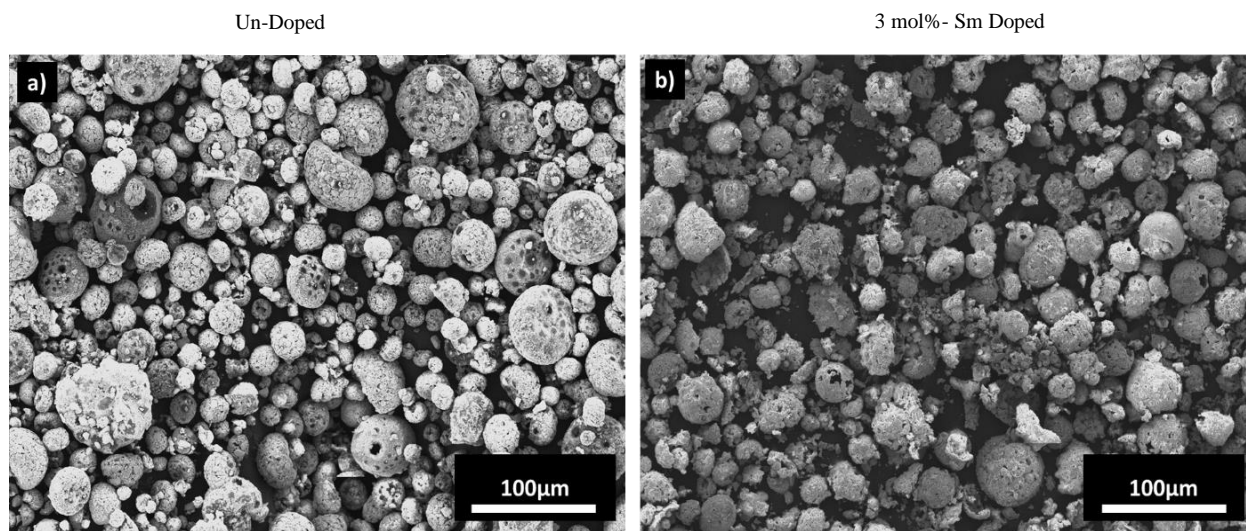


**Figure 2.1 SEM images of a) undoped  $\text{ZrB}_2/\text{SiC}$  spray dried powders and b) 5mol% Sm-doped  $\text{ZrB}_2/\text{SiC}$  granules post sieving.**

### 2.3 Pressing and Sintering Sm-doped $\text{ZrB}_2/\text{SiC}$ Powders

The doped powder was then pressed into  $38\text{mm} \times 38\text{mm} \times 5\text{mm}$  billets at 82 MPa at room temperature. Green density of the samples was  $\sim 4.0\ \text{g}/\text{cm}^3$  (70%). The billets were then arranged and sandwiched between two SiC plates layered with graphite and sprayed

with boron nitride. The purpose of the SiC plates was to avoid bloating of the samples due to outgassing during sintering. Set up of the samples in the furnace can be seen in Figure 2.2.

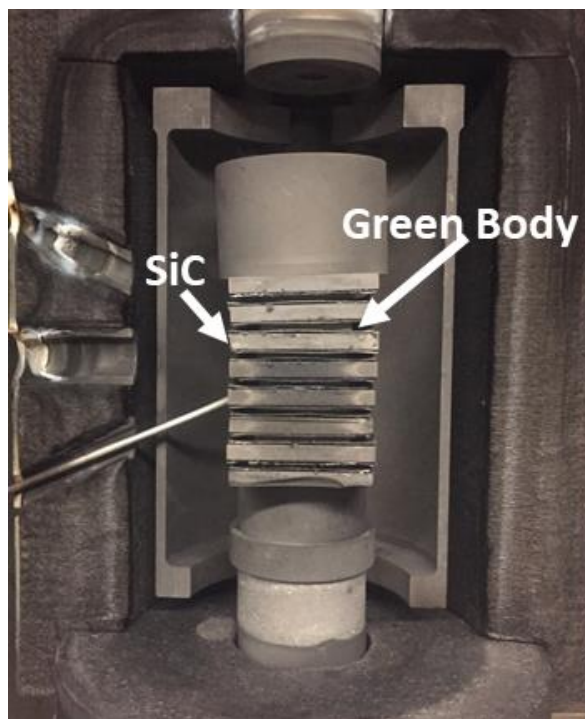


**Figure 2.2 Green bodies of pressed Sm-doped ZBS sandwiched between SiC plates. A 250g graphite weight on top of the stack was for stability. Total billets in furnace was 14.**

The pressed billets were then sintered in argon, as seen in Figure 2.2, at 2000°C for 15 minutes (Series System VI, Centorr Vacuum Industries, Nashua, USA). A 1-hr hold at 1650°C, prior to reaching 2000°C, was programmed into the heating cycle to evaporate the boron glass formed from the boron nitride. The densities of the sintered billets were  $87\pm 2\%$  as measured by Archimedes' method; a theoretical density of  $6.36 \text{ g/cm}^3$  was used for the calculations. The billets had a linear shrinkage of  $\sim 20\%$  in the width and length and  $\sim 13\%$  shrinkage in the thickness. Samples with densities of 79% and 69% were also fabricated by lowering the hold temperature to 1925°C and 1850°C respectively. The composition of the billets was measured by mass spectroscopy (NSL Analytical Services Inc., Cleveland, USA) and comprised of 29.8 mol% (67.6

wt%) Zr, 56.7% (15.6 wt%) B, 7% (2.2 wt%) C, 0.5% (0.4 wt%) Si, 3% (11.2 wt%) Sm, 2.8% (1.2 wt%) O, and 0.2% (1.8 wt%) impurities. As noted earlier the starting mol% Sm doped into the billets was ~3.5 mol% the ~0.5 mol% loss is likely occurred during powder handling or sintering.

#### 2.4 Pressing and Solid-State Reaction Sintering of $c_1\text{-Sm}_{0.2}\text{Zr}_{0.8}\text{O}_{1.9}$

$c_1\text{-Sm}_{0.2}\text{Zr}_{0.8}\text{O}_{1.9}$  (SZO) billets were fabricated by mixing 11mol%  $\text{Sm}_2\text{O}_3$  (3 $\mu\text{m}$ , 99.9% pure  $\text{Sm}_2\text{O}_3$ , Sigma-Aldrich, St. Louis, USA) and 89mol%  $\text{ZrO}_2$  (5 $\mu\text{m}$ , 99.9% pure  $\text{Sm}_2\text{O}_3$ , Sigma-Aldrich, St. Louis, USA) in a ball mill with yttrium stabilized zirconica (YSZ) milling media for 2 hours. The powder was then mixed by shaking for 10 seconds and put back on the ball mill for another 2 hours. The mixed powder was then pressed into 38mm x 38mm x 5mm billets at 300 kPa at room temperature. The green body was then placed on a YSZ substrate and heated in a furnace in air. The different heating conditions can be found in Table 2.1.

**Table 2.1 Table of ramp rate, hold temperature, and hold time for SZO heated in a furnace**

Sample	Ramp rate	Hold Temperature	Hold Time
1	10°C/min	1700°C	1 hr
2	10°C/min	1700°C	2hr
3	10°C/min	1700°C	3 hr
4	10°C/min	1700°C	4 hr
5	10°C/min	1700°C	5 hr
6	10°C/min	1700°C	10 hr
7	5°C/min	1700°C	1 hr
8	5°C/min	1700°C	2 hr
9	5°C/min	1700°C	3 hr
8	10°C/min-nano powder	1700°C	5 hr
9	10°C/min	1600°C	1 hr
10	10°C/min	1500°C	1 hr
11	10°C/min	1400°C	1 hr

## 2.5 Polishing and Adding Surface Roughness to Sintered Billets

Billets were then cut to 25.4mm x 25.4 mm and polished using an automatic polisher (GPX Series Advanced Autopolisher, LECO Corp., St. Joseph, USA) to an  $R_a$  of  $0.4\pm 0.1\mu\text{m}$  which was measured via atomic force microscopy (AFM) (Dimension 5000 AFM, Bruker, Santa Barbara, USA). Samples where surface finish was varied were then abraded for 10s on the automatic polisher using diamond solutions of  $3\mu\text{m}$  and  $6\mu\text{m}$  to achieve  $R_a$  values of  $0.9\pm 0.2\mu\text{m}$  and  $1.4\pm 0.3\mu\text{m}$ . Table 2.2 presents the names, and microstructural properties of the pre-tested billets. As the R number increases, so does the surface roughness and as the D number increases, the open porosity does as well. For example, D1R2 has a larger surface roughness than D1R1 while D2R1 has a higher open porosity than D1R1.

**Table 2.2 Pre-tested billet naming convention, density, open porosity, and surface roughness.**

<b>Sample</b>	<b>Density (%)</b>	<b>Open Porosity(%)</b>	<b>Ra (<math>\mu\text{m}</math>)</b>
D1R1	87	7.5	$0.4\pm 0.1$
D1R2	87	7.5	$0.9\pm 0.2$
D1R3	87	7.5	$1.4\pm 0.3$
D2R1	79	14	$1.0\pm 0.2$
D3R1	69	24	$1.1\pm 0.2$

### 3. ANALYTICAL AND EXPERIMENTAL EQUIPMENT AND PROCEDURES

#### 3.1 Microstructural and Phase Analysis

Before performing the microstructural analysis, the samples were coated with a thin layer of Au/Pd. A scanning electron microscope coupled with energy dispersive spectroscopy (SEM/EDS) (Quant 650 FEG, Thermo Fischer Scientific, Hillsboro, USA) was used to characterize coating topography in the as-sprayed conditions after each cycle. EDS analysis and mapping was also collected at 30kV using a working distance of 10mm. The cross-sectioning was cut using a surface grinder (G38P 60NC, Supertec, Noida, India) in the plunge setting at a rate of 1 $\mu$ m per swipe. Polishing of the samples was performed using an automatic polisher (GPX Series Advanced Autopolisher, LECO Corp., St. Joseph, USA).

X-ray diffraction (XRD) (D8 Focus, Bruker Corporation, Billerica, USA) was used to investigate the phases present in the billets after sintering, post oxyacetylene ablation, and post laser heating. Billets were exposed to Cu K $\alpha$  radiation for 2 $\theta$  values of 20°-80° using a step size of 0.02° and a scan rate of 5°/minute. Samples were aligned in the XRD to analyze the regions where the ablation flame was most intense.

AFM (Dimension 500 AFM, Bruker, Santa Barbara, USA) was used to measure the pre-ablated average surface roughness ( $R_a$ ) of the specimens over a 300+  $\mu$ m<sup>2</sup> area. The  $R_a$  value obtained by the AFM takes the average of the hills and valleys of the sample for calculation. Contact mode was used with a speed of 350 points/second. It should be noted that porosity influenced the  $R_a$  values for both the samples of varying surface roughness and porosity. Due to the fact that it is the area as a whole that affects the emittance, the average surface of the sample

was taken into consideration, including the large pores. Figure 3.1 shows the AFM images acquired to obtain the  $R_a$  results.

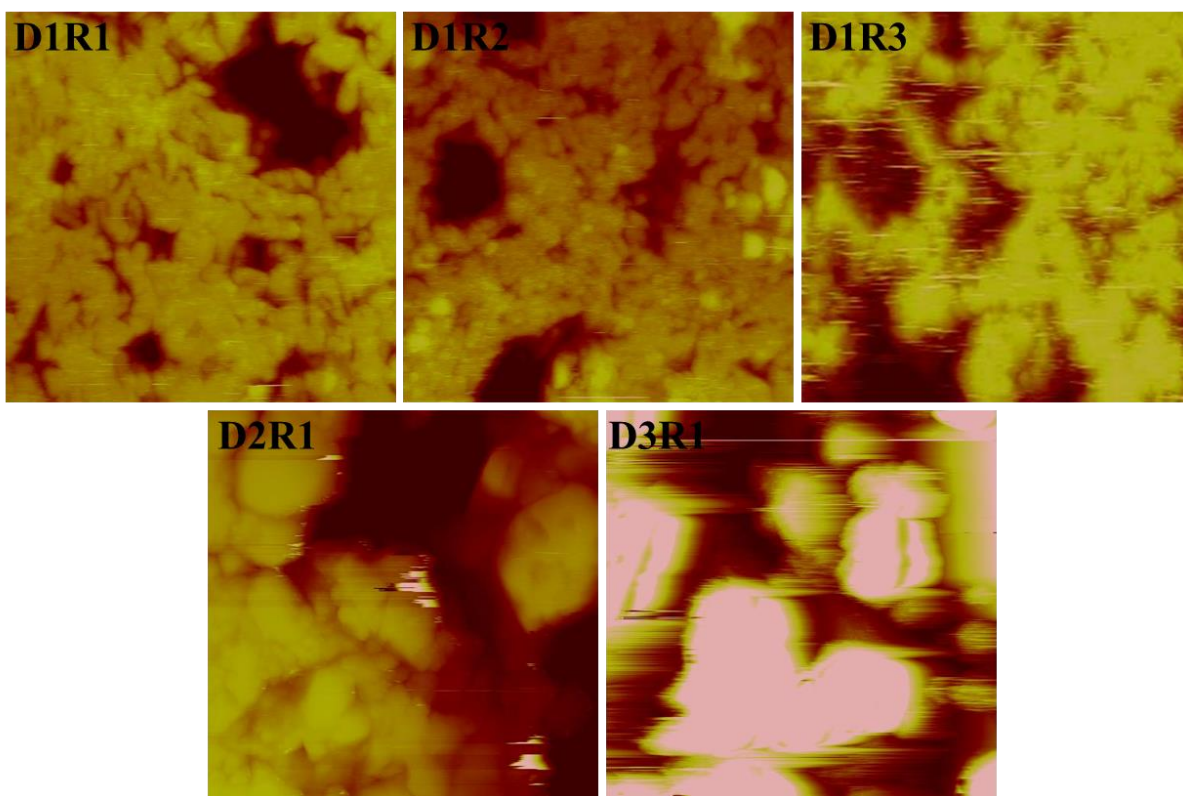


**Figure 3.1** Raw atomic force microscopy images of the samples with different surface roughness and porosities.

### 3.2 Density Evaluation of Billets

The billets densities were measured using Archimedes' method as described in the ASTM B962-17 standard.<sup>33</sup> The theoretical density was calculated using the rule of mixtures method for  $ZrB_2$  ( $6.085 \text{ g/cm}^3$ ),  $SiC$  ( $3.21 \text{ g/cm}^3$ ),  $Sm_2O_3$  ( $8.35 \text{ g/cm}^3$ ),  $ZrO_2$  ( $6.09 \text{ g/cm}^3$ ), and  $Tm_2O_3$  ( $8.60 \text{ g/cm}^3$ ). The theoretical density for Sm-doped ZBS was  $6.36 \text{ g/cm}^3$ , SmTm-doped ZBS was  $6.80 \text{ g/cm}^3$ , and for Tm-doped ZBS was  $6.57 \text{ g/cm}^3$ . The theoretical density for  $c_1\text{-Sm}_{0.2}\text{Zr}_{0.8}\text{O}_{1.9}$  was  $6.67 \text{ g/cm}^3$ .

### 3.3 Oxyacetylene Ablation Tests

The test rig was constructed using ASTM 285-082 as a standard.<sup>34</sup> Setup of the ablation rig can be seen in Figure 3.2 The ablation torch (Victor Technologies, St. Louis, USA) used a 5 mm orifice and a separation distance of 20 mm between the sample and the torch tip was kept as a constant. Front and back face temperatures as a function of time were measured using a one-color pyrometer (OS3750, Omega Engineering Inc., Stamford, CT, USA), which was connected to a data logger and thermocouple respectively. The emittance setting for the pyrometer was set to 0.9 as the true emittance of the samples were unknown. The pyrometer has the capability to be in one- or two-color mode as well as can measure surface temperature between 400°C and 3000°C. An oxygen rich environment was simulated using an oxygen: acetylene ratio of 12:10 slpm to imitate an oxidizing environment, such as re-entry. Test specimens were exposed to the flame for either 10s, 60s, or 300s. Time began when sample hit the flame at the specified distance and was monitored manually. The heat flux was measured to be 452 W/cm<sup>2</sup> using a thermogage circular foil heat flux gauge (TG1000-4, Vatell Corp., Christiansburg, VA).

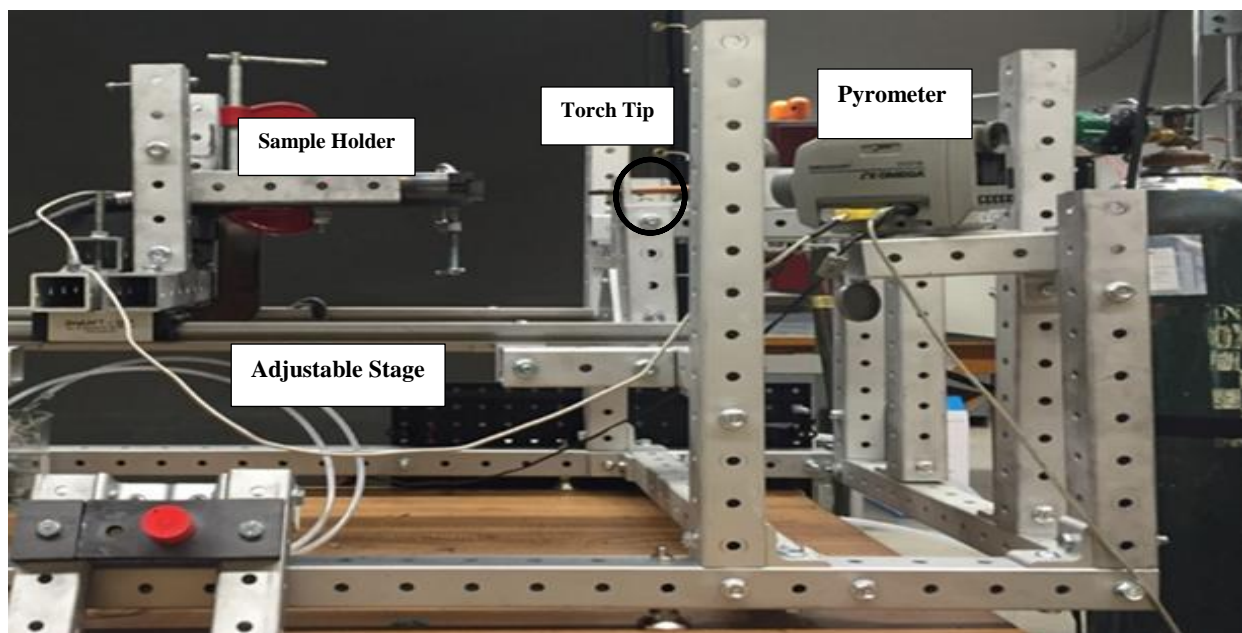


Figure 3.2 Set up of the oxyacetylene ablation rig.

### 3.4 Spectral Emittance Testing

Emittance testing was performed at the RHINO lab at the Air Force Research Laboratory (AFRL). The billets were held in a graphite holder and heated with a laser on the back side of the billet. A schematic of how the sample was heated can be seen in Figure 3.3. Spectral radiance in the 1500nm-5000nm (1.5 $\mu$ m-5 $\mu$ m) range was collected at an angle of  $\sim 45^\circ$  on the front side (spectrometer side) of the billet where the different surface features were. Set up of the samples can be seen in Figure 3.4

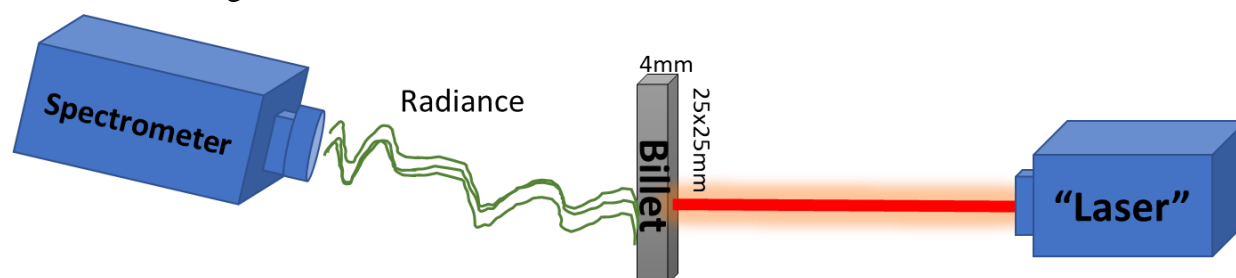


Figure 3.4 Schematic of where billet was heated and where the spectral radiance was collected. Surface features of sample were on the side where spectral radiance was collected.

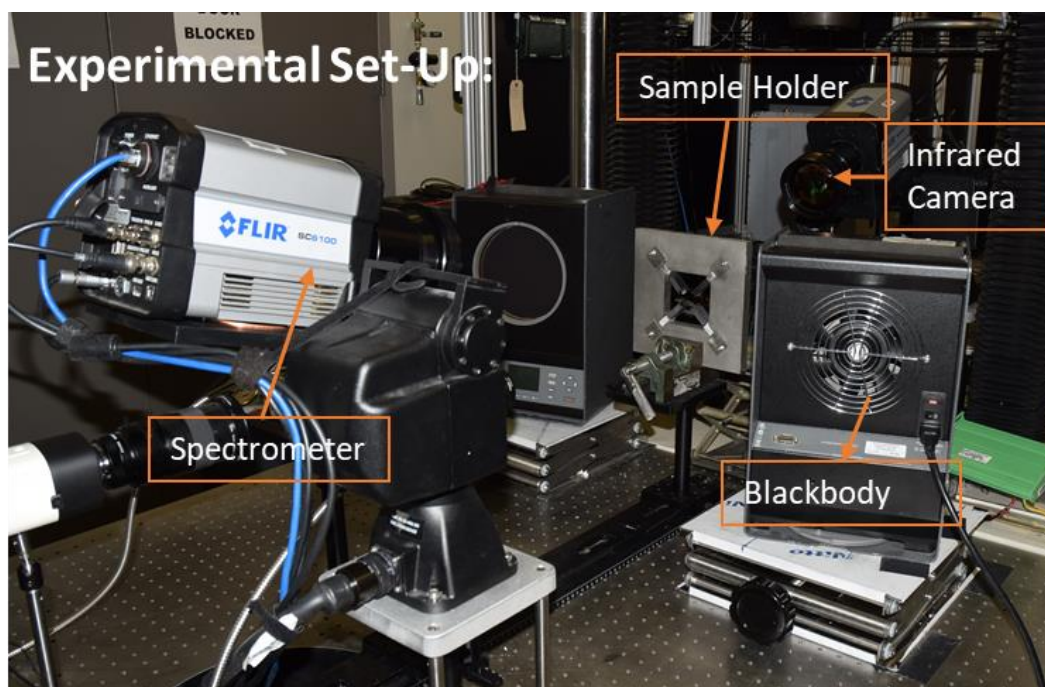


Figure 3.3 Experimental set-up of RHINO lab at AFRL.

The samples were held at a power of either 700W, 800W, or 900W for 60s. The total heating time was 80s. The maximum temperatures reached by the samples can be seen in Table 3.1. A MatLab code by Pena et. al.<sup>35</sup> using the plankian form of the Saukuma-Hattori equation (Equation 3.1) was used to extract the emittance and temperature data from the radiance data collected by the spectrometer.<sup>35,36</sup>

**Table 3.1 Samples maximum temperature reached during laser heating.**

Sample	Max Temperature Reached (°C)		
	700W	800W	900W
D1R1	2108	2094	2226
D1R2	1878	2009	2133
D1R3	1937	2041	2179
D2R1	2197	2407	2327
D3R1	1990	2142	2231
SmTm	1669	2112	1792
Tm		1701	1933

$$\text{Equation 3.1 } T = [\varepsilon^{-1/4}] * \left[ \frac{c^2}{A \cdot \ln\left(\frac{C}{L_\lambda}\right)} - \frac{B}{A} \right]$$

T represents the maximum temperature reached,  $\varepsilon$  is the emittance of the sample,  $L_\lambda$  is the spectral radiance, A is the wavelength, and B and C are constants. B remains constant across all wavelengths while C decreases slightly across the wavelengths. Essentially the equation with the emittance set to 1 is solved 6 times to perform a black body calibration as well as to extract the

constants B and C. The emittance term is then added back into equation 3.1 and set to 0.3 (the emittance of the resulting phase post laser heating) and solved for the true temperature in the 3500nm-4000nm wavelength range. The 3500nm-4000nm wavelength range was chosen because this is where the spectral radiance data was most stable. From there the equation is then back solved to extract out the emittance.<sup>35</sup> Wavelengths in the range of 1700nm-4000nm (1.7 $\mu$ m-4.0 $\mu$ m) was used in the MatLab code as outside this range the noise in the spectrometer covered the data. It should also be noted that any error in the calculations was likely due to the emittance setpoint (0.3). For an emittance set point of 0.1 higher or lower than the reported value (for example set to either 0.2 or 0.4), the emittance graphs would be shifted by an average of  $0.11 \pm 0.005$  standard error. If the emittance set point were to be set to 0.6 (~the average emittance of ZrB<sub>2</sub>) the graphs would be shifted by an average of  $0.30 \pm 0.004$ . Calculations for the standard error were under the 95% confidence interval.

### 3.5 Linear Thermal Expansion Measurements

A dilatometer (2016STD, Orton, Westerville, USA) was used to measure the linear thermal expansion (LTE) of c<sub>1</sub>-Sm<sub>0.2</sub>Zr<sub>0.8</sub>O<sub>1.9</sub>. Sintered samples ~24mm in length with a 8mm diameter were heated to 1600°C in air at a heating rate of 5°C/min. The LTE ( $\Delta L/L_0$ ) and coefficient of thermal expansion (CTE,  $\alpha_L$ ) were measured using equations 3.2 and 3.3 respectively.  $\Delta L$  is the change in length,  $L_0$  is the initial length of the sample,  $L_1$  is the final length, and  $\Delta T$  is the change in temperature (K).

$$\text{Equation 3.2} \quad \frac{\Delta L}{L_0} = \frac{L_1 - L_0}{L_0}$$

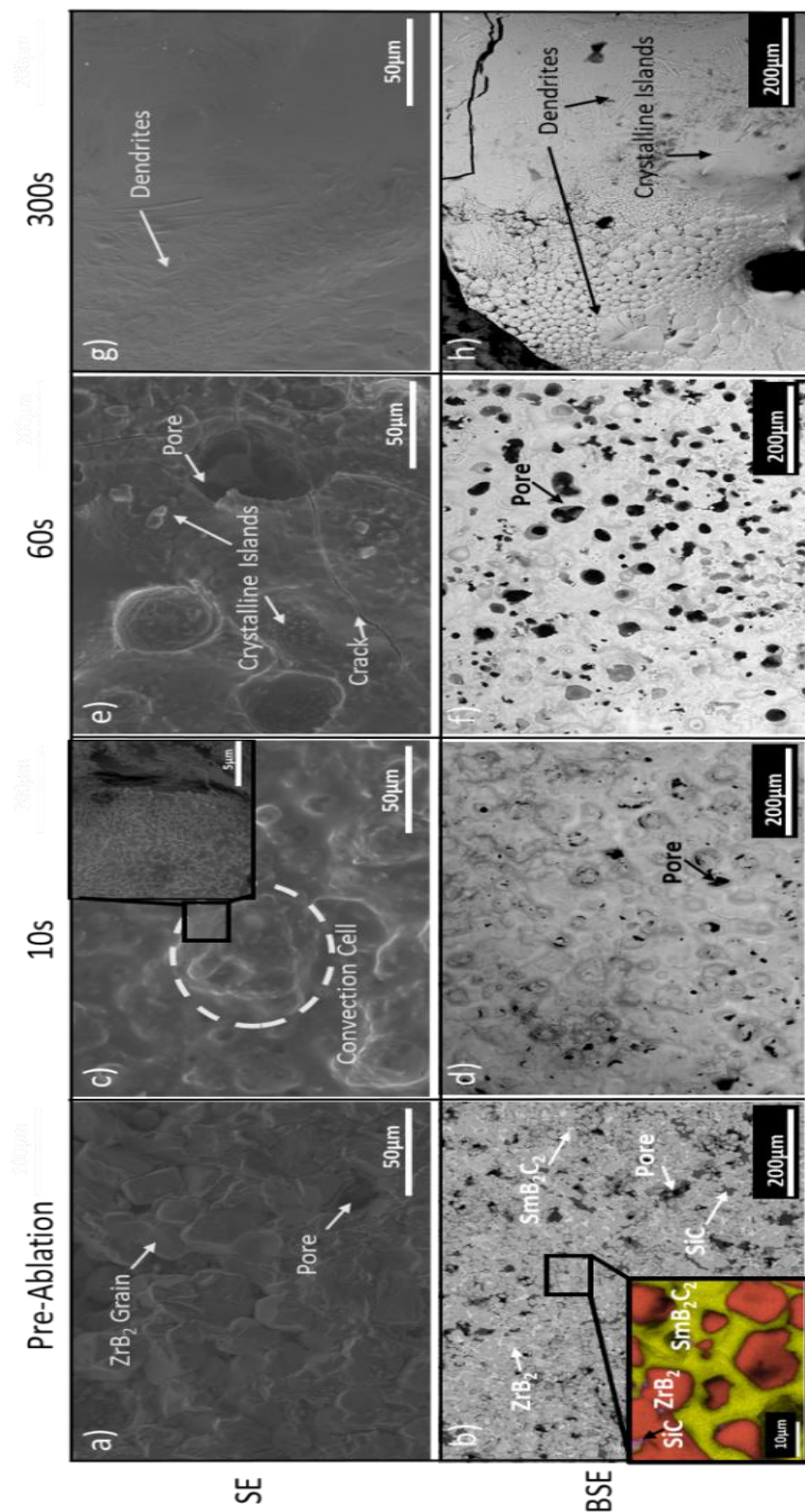
$$\text{Equation 3.3} \quad \alpha_L = \frac{1}{L_0} \frac{\Delta L}{\Delta T}$$

## **4. IN-SITU OXIDE SCALE INVESTIGATION OF SAMARIUM-DOPED ZIRCONIUM DIBORIDE/ SILICON CARBIDE BILLETS**

### **4.1 Results**

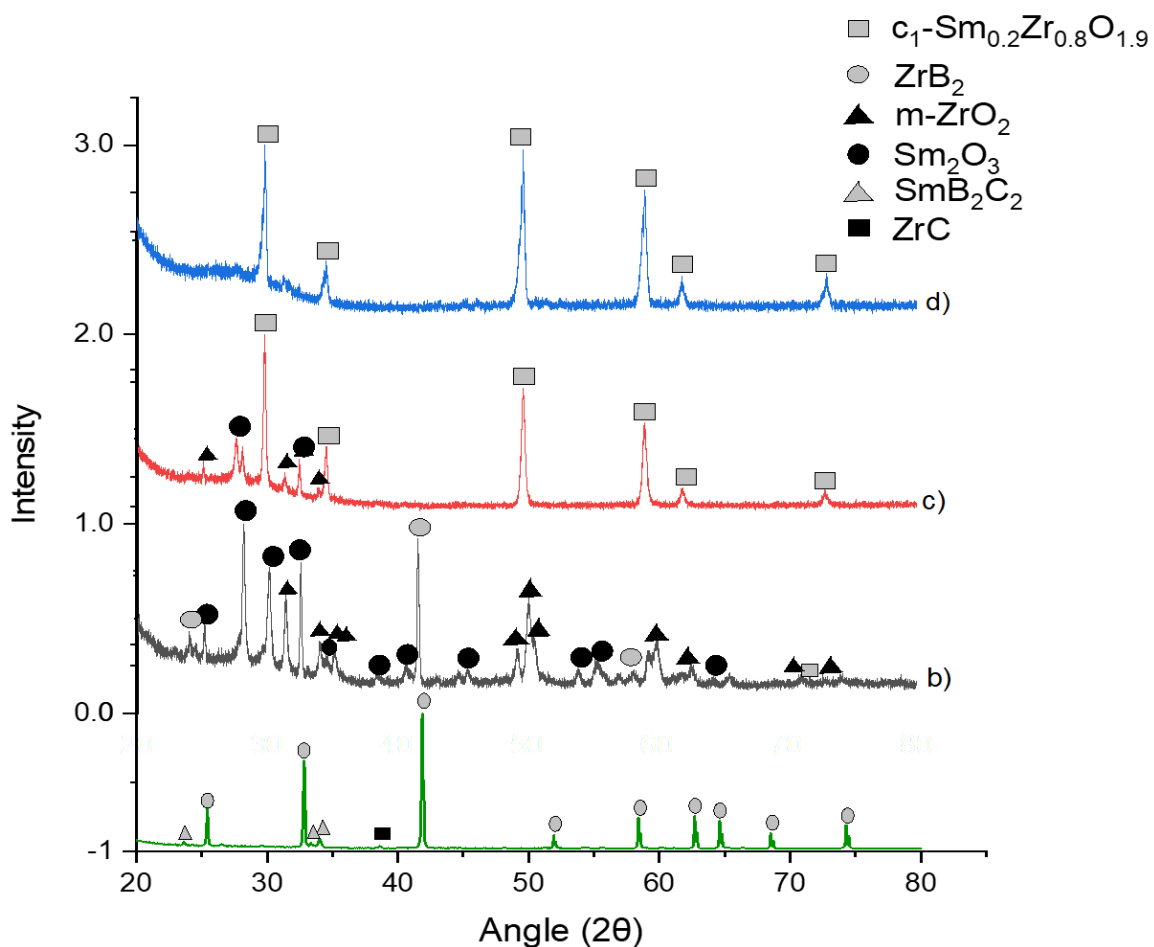
#### **4.1.1 Pre-ablated Microstructure and Phase Assemblage**

Figure 4.1a show the pre-ablated microstructure of the 87% dense ceramic billet. As expected, there are porous and dense regions visible. Figure 1b shows the BSE image of the pre-ablated billet, which contains several distinct phases corresponding to  $ZrB_2$ ,  $SmB_2C_2$ , and SiC as seen in XRD (Figure 4.2a). The increased magnification inset image in Figure 4.1b shows the  $ZrB_2$  grains are surrounded  $SmB_2C_2$ , with some SiC noted.



**Figure 4.1 SEM micrographs at different magnifications for pre-ablated billets, 10s post ablated, 60s post ablated, 300s post ablated. The magnified excerpt image in (b) shows  $ZrB_2$  grains (red) surrounded by  $SmB_2C_2$  matrix (yellow) with patches of SiC (purple). Excerpt BSE image in (c) shows the magnified surface of the convection cell containing oxide islands dispersed in a glassy phase.**

In Figure 4.2a the predominant phase is  $\text{ZrB}_2$ , with small peaks correlating to the  $\text{SmB}_2\text{C}_2$  matrix. A small  $\text{ZrC}$  peak is also visible in the pre-ablated XRD scan. The oxidation of the  $\text{SiC}$  to  $\text{SiO}$  and  $\text{CO}$  during sintering, coupled with the degradation of  $\text{Sm}_2\text{O}_3$  from the pre-sintered powders in the reducing atmosphere providing the oxygen for the oxidation of  $\text{SiC}$ , is believed to result in the formation of the  $\text{ZrC}$ ,  $\text{SmB}_2\text{C}_2$ , and loss of  $\text{SiC}$  in the billets. Similar reactions also occurred with pressurless sintered  $\text{Y}_2\text{O}_3/\text{SiC}$ .<sup>37</sup>



**Figure 4.2 XRD of a) pre- and post-ablated billets after b) 10s, c) 60s, and d) 300s.**

#### 4.1.2 Weight Gain and Heating Profile as a Function of Ablation Time

Figure 4.3 shows the front-face sample temperature as a function of ablation time for 10, 60, and 300s holds. The temperature reached after 10, 60, and 300s was 1494°C, 1656°C, and 1870°C,

respectively. As the emittance of the oxide scale formed is unknown, the pyrometer emittance setting was set to 0.9, which is believed to be higher than the actual emittance ( $\epsilon$ ) of the oxide. Due to the 0.9  $\epsilon$  set point, it is believed the actual temperatures reached are higher than measured by the pyrometer. The weight gained after 10s, 60s, and 300s was 0%, 0.8%, and 2.6%, respectively. The inset optical image in Figure 4.3b shows a white oxide scale after a 10 sec hold, with this surface not much different from the pre-ablated image shown in Figure 4.3a. As shown in Figures 4.3c (60s hold) and Figure 4.3d (300s hold), the oxide scale becomes increasingly more yellow as the ablation time increases. It is important to note that the crack in Figure 4.3c is a result of excessive force used when billet was removed from the sample holder and is not a result of thermal shock. The dotted circles on the optical images indicate where XRD and SEM/EDS analysis were performed.

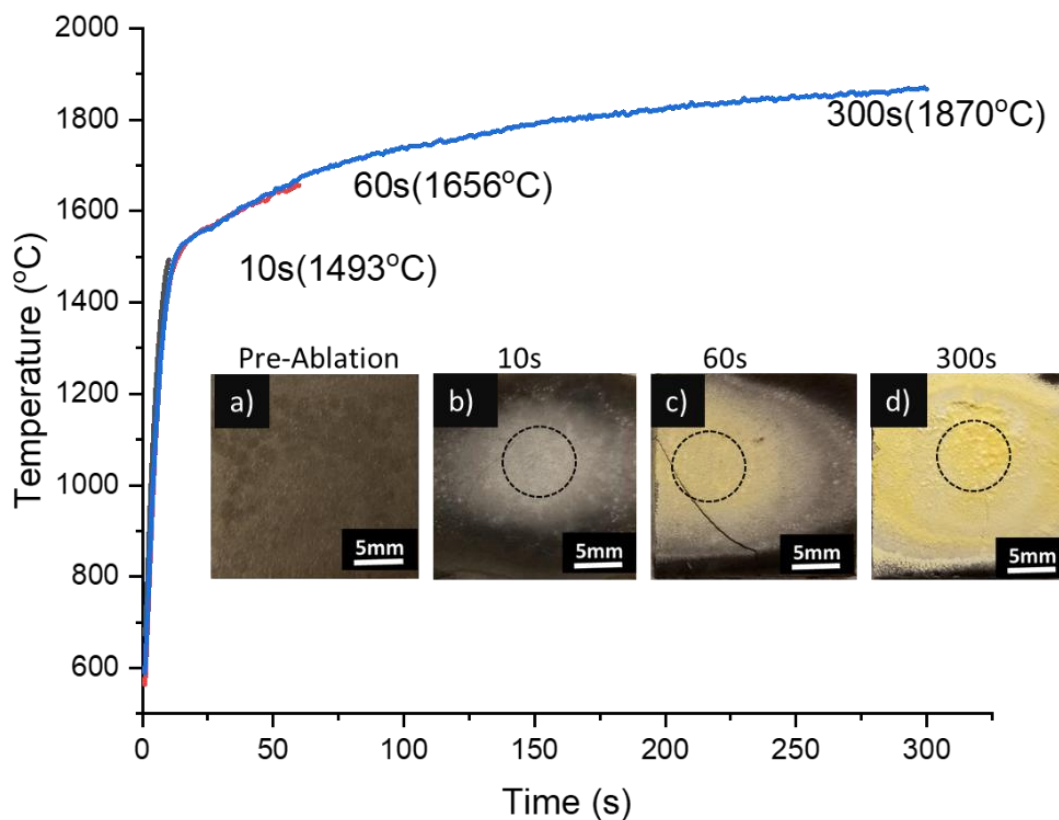


**Figure 4.3 Time vs. temperature graph of ablated samples 10s, 60s, and 300s. Optical images are a) before ablation, b) 10s post ablation, c) 60s post ablation, and d) 300s post ablation.**

#### 4.1.3 Phase Make-up After Ablation

XRD analysis, presented in Figure 4.2b, shows the phases present after 10s change from  $\text{ZrB}_2$  and  $\text{SmB}_2\text{C}_2$  to  $\text{Sm}_2\text{O}_3$  and  $m\text{-ZrO}_2$  with residual  $\text{ZrB}_2$ . Thus, a 10s exposure is enough to begin the oxidation process. Furthermore, the presence of an amorphous hump at low  $2\theta$  suggests a glassy phase is present on the surface. As shown in Figure 4.2c the phases present on the surface after 60s of ablation are a  $c_1\text{-Sm}_{0.2}\text{Zr}_{0.8}\text{O}_{1.9}$  (SZO),  $\text{Sm}_2\text{O}_3$ , and  $m\text{-ZrO}_2$ . XRD results after 300s, as shown in Figure 4.2d, shows a single-crystalline phase, SZO, as well as an amorphous hump.

#### 4.1.4 Microstructure Changes with Ablation

Figures 4.1c-d show the formation of convectional cells surrounded by what appears to be a glassy phase after 10s of ablation. A convection cell is formed through the oxidation of  $ZrB_2/SiC$  to  $ZrO_2$  and borosilicate glass. The Zr- and Sm-doped glass is pushed to the surface from the oxidation of  $ZrB_2$  to  $ZrO_2$ , forming the protrusions on the surface as seen in Figure 4.1c-d.<sup>38</sup> These cells burst due to the surge in pressure from the liquid with increased time and heating due to the pressure induced by volume expansion of the oxidation products as well as the evaporation of the glass and the oxidation of C (in the SiC) to CO or  $CO_2$ . Once the glass reaches the surface, the boria and silica glass evaporate, and the remaining high concentrations of Zr and Sm can form  $ZrO_2$  and  $Sm_2O_3$ , respectively. These appear as crystalline phases on the surface. As shown in Figures 4.1e-f, the process of oxidation of the  $ZrB_2$ , SiC, and the  $SmB_2C_2$  continues. The oxidation penetrates deeper into the sample and the developed glassy phase is transported to the surface. Eventually the cell bursts due to evaporation of the glass and/or production of CO or  $CO_2$ . This appears to be more prevalent after 60s. Figures 4.1g-h show large pores, indicative of continuing oxidation, along with a large crystalline region present in the topography after 300s. Large grains and dendrites are visible after 300s as seen in Figure 4.1h, indicating a possible eutectic may have occurred between the glass and the crystalline phase.<sup>39</sup>

Figure 4.4 shows cross-sections of the samples after ablation. The oxide scale thickness increases from  $\sim 50\mu m$  after 10s to  $\sim 150\mu m$  after 60s as seen in Figure 4.4a and 4.4c, respectively. After 300s the oxide scale thickness increases to  $\sim 400\mu m$  as seen in Figure 4.4e. These oxide scales form three distinct zones: Zone 1 is the fully developed and reacted oxide scale, Zone 2 is a transition region where oxidation is continuing to occur, and Zone 3 is where the sample has begun to oxidize the  $SmB_2C_2$  matrix.

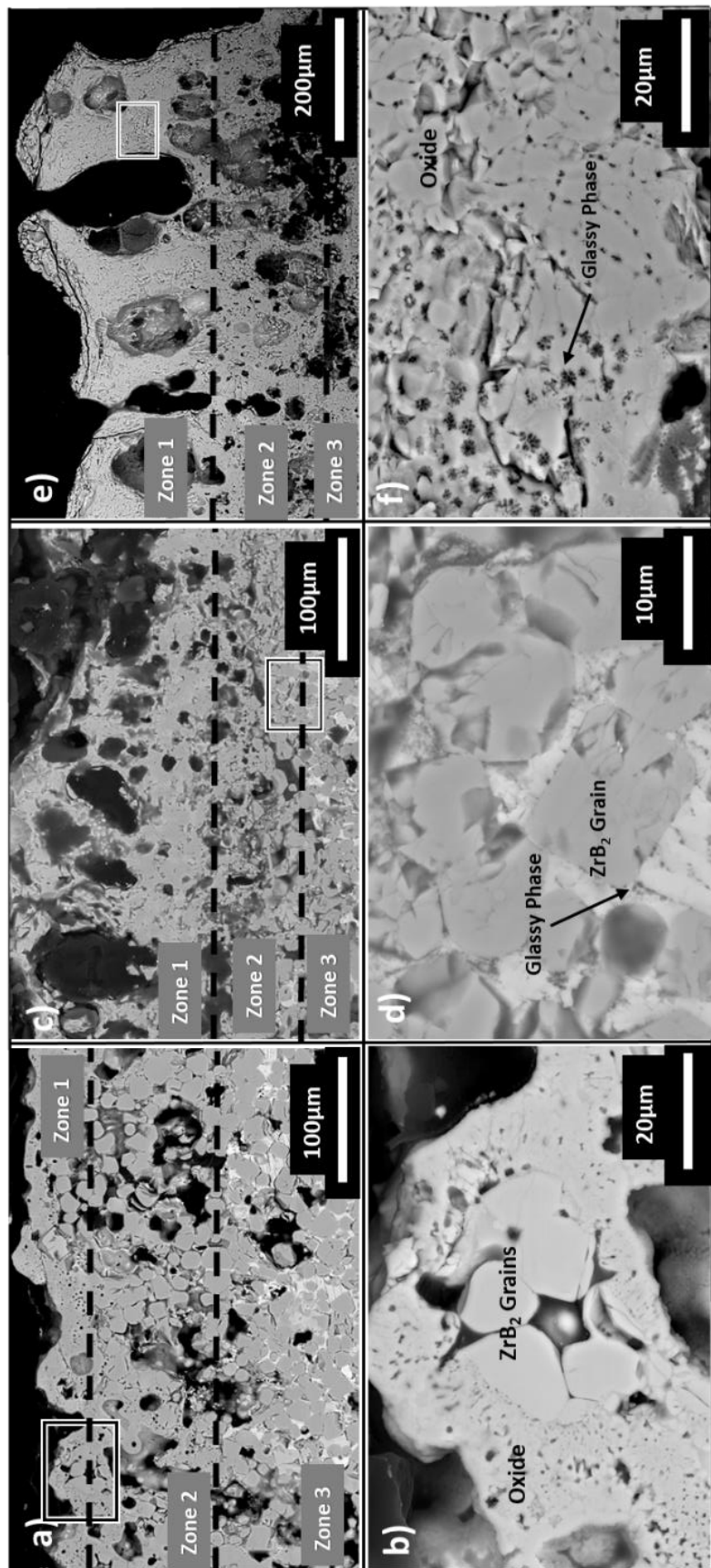


Figure 4.4 BSE cross-sectional images of a) 10s ablated, c) 60s ablated, and e) 300s ablated billets. Boxed areas correspond to higher magnified images (images b, d, and f) showing crystalline regions and an intergranular glassy phase.

EDS analysis of the billets after 10s, 60s, and 300s (see Figure 4.5) show differences in the distribution and concentration of Zr, O, and Sm with time and location. After 10s of ablation, the formation of a thin oxide scale can be seen in Figure 4.5 (see Zone 1). The main oxide scale in Zone 1 has a distinct microstructure where both the Zr and Sm appear to be homogeneously mixed compared to Zone 3, which has distinct regions of Zr that maintain the original  $ZrB_2$  square-grain morphology. As shown in Figure 4.5, a thin Zone 2 region is also observed after 10s in that the Zr and Sm regions are still distinct, but the  $ZrB_2$  grain is starting to transform into the oxide. After 60s of ablation, the primary oxide scale region (Zone 1) has become thicker as evidenced by the complete mixing of the Zr and Sm atoms in this region. XRD results, presented in Figure 4.2c, would indicate this region to be primarily SZO. Zone 2 can also be clearly seen as having a similar microstructure to Zone 1, however there are still regions of higher concentration of Zr and Sm. It should be noted that EDS shows evidence of small amounts of Sm in the higher Zr concentration regions in Zone 2. Near the bottom of Zone 2 there appears to be a region that is void of Sm atoms deemed a Sm-depletion region; however, the high Zr concentration regions in Zone 2 contain ~2 at% Sm indicating the Zr is slightly doped. After 60s of ablation, there is still an unoxidized  $ZrB_2$  region apparent with some oxidation of the  $SmB_2C_2$  matrix (Zone 3). After 300s of ablation the oxide scale has thickened to where two images (Figure 4.5 top and bottom) were needed to reveal microstructural features. After 300s of ablation, the main oxide scale (Zone 1) can be seen to have become thicker. Zone 2 was also observed to have thickened; a similar Sm atom depletion region was also observed.

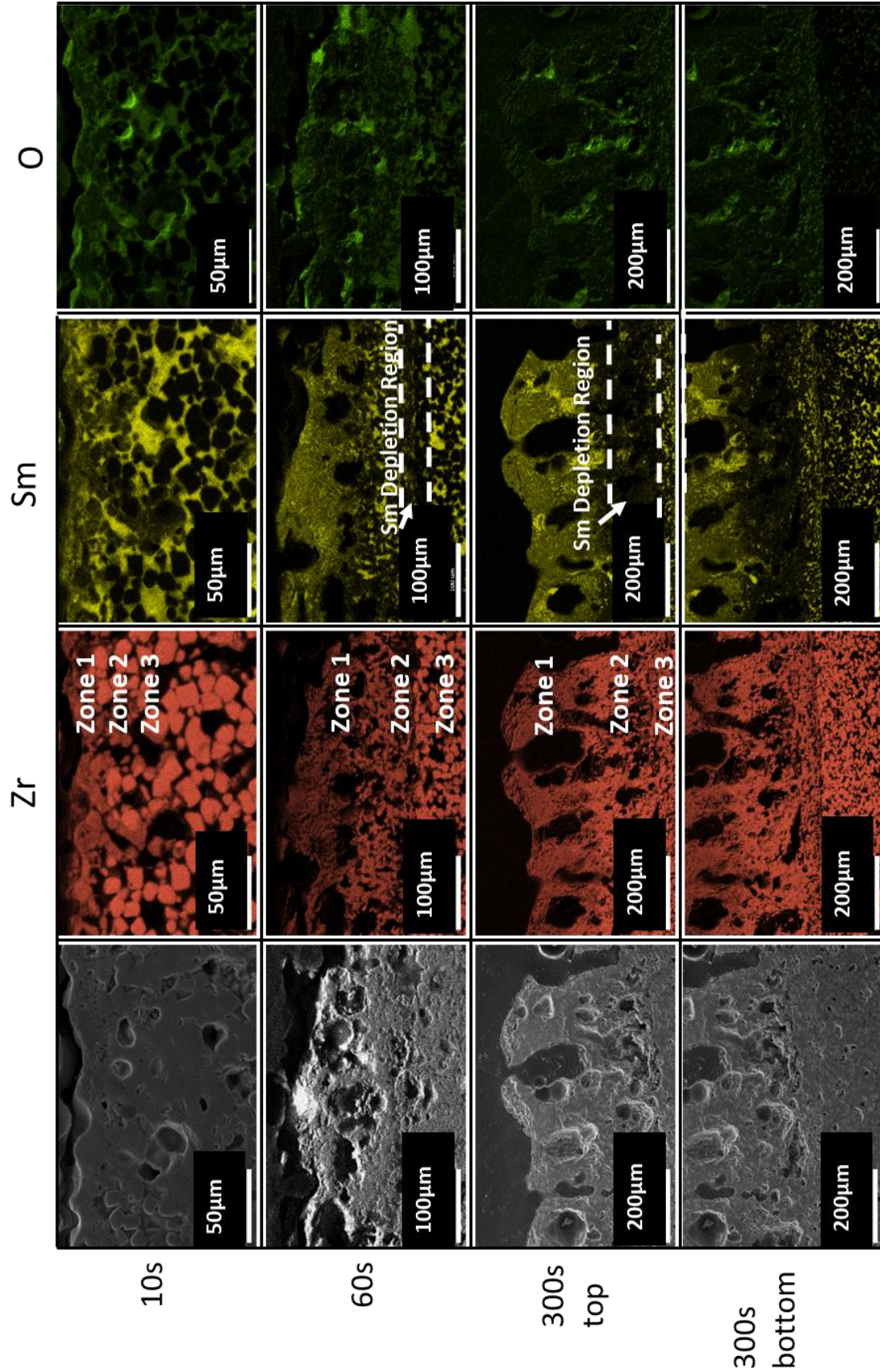


Figure 4.5 Cross-sectional EDS analysis of billets after 10s, 60s, and 300s of ablation.

## 4.2 Discussion

### 4.2.1 First observation: Development of the Oxide Scale Morphology as a Function of Time

#### 4.2.1.1 Post 10s of Ablation

In Figures 4.1c-d, the topographical microstructure after 10s of ablation consists of partially erupted convectional cells. Convectional cells like these were observed by Karlsdottir et. al.<sup>40</sup> in 15 vol% SiC-85 vol% ZrB<sub>2</sub> that were heated to 1550°C in air for 1 hr. They observed protrusions of islands of ZrB<sub>2</sub> in lagoons of SiO<sub>2</sub> that were a result of viscous fingering created by borosilicate liquid moving up through porous ZrO<sub>2</sub> columns and across a more viscous silica rich fluid. In EDS analysis of our system, B is not evident on the surface. However, this is likely due to the limitations of EDS as well as the high concentrations of the other elements present. Viscous fingering results from the the injection of a less viscous liquid into a higher viscous liquid in a porous medium.<sup>41,42</sup> Although Zr is known to be a substitute for Si or B in glass and increase its viscosity, in small quantities it lowers viscosity.<sup>39</sup>

Evidence of the rupture and formation of convectional cells can be seen in Figures 4.4a and 4.4b where angular ZrB<sub>2</sub> grains are transforming into what appears to be a porous oxide as described by Karlsdottir et. al.<sup>40</sup> The formation of the Zr-doped borosilicate glass occurs at a reaction interface, such as a grain boundary.<sup>19</sup> This is the case for our system as well, where the reaction interface can be seen in Figure 4.4d where the glass is beginning to form at the grain boundaries of ZrB<sub>2</sub>. It was suggested that the driving force for the liquid flow is from the volume increase due to oxidation of ZrB<sub>2</sub> to ZrO<sub>2</sub>.<sup>40</sup> In early oxidative stages, the Zr-rich borosilicate liquid flows through the pores of the primary oxidized ZrO<sub>2</sub> porous layer. Later the volume increase induces pressure and stress, leading to the rupture of the oxide scale where the liquid is then squeezed up to the surface and flows to form the convectional cells and their features. The rapid evaporation of boria results in rapid formation of precipitated zirconia and rapid formation of

convection cells.<sup>38</sup> The inset image in figure 4.1c shows small oxide islands dispersed in the glassy phase on a convectional cell. These are believed to be evidence of  $ZrO_2$  and  $Sm_2O_3$ , as seen in Figure 4.2b. Figure 4.6 shows cross-sectional EDS analysis after 10s of ablation of a  $ZrB_2$  grain nested in a convectional cell in Zone 1. Sm-doped Si can be seen between the grains together and the Zr starting to dissolve into the liquid. This confirms the travel path of the liquid. The lack of evidence of boria in Figure 4.6 is likely due to the rapid evaporation of the glass. It can also be seen that the oxygen rich region of the columns contains atoms of Zr and Sm. This is indicative of the viscous fingering described in Karlsdottir etl. al.<sup>40</sup> as well as evidence of the reaction interface for Sm-Zr borosilicate liquid.

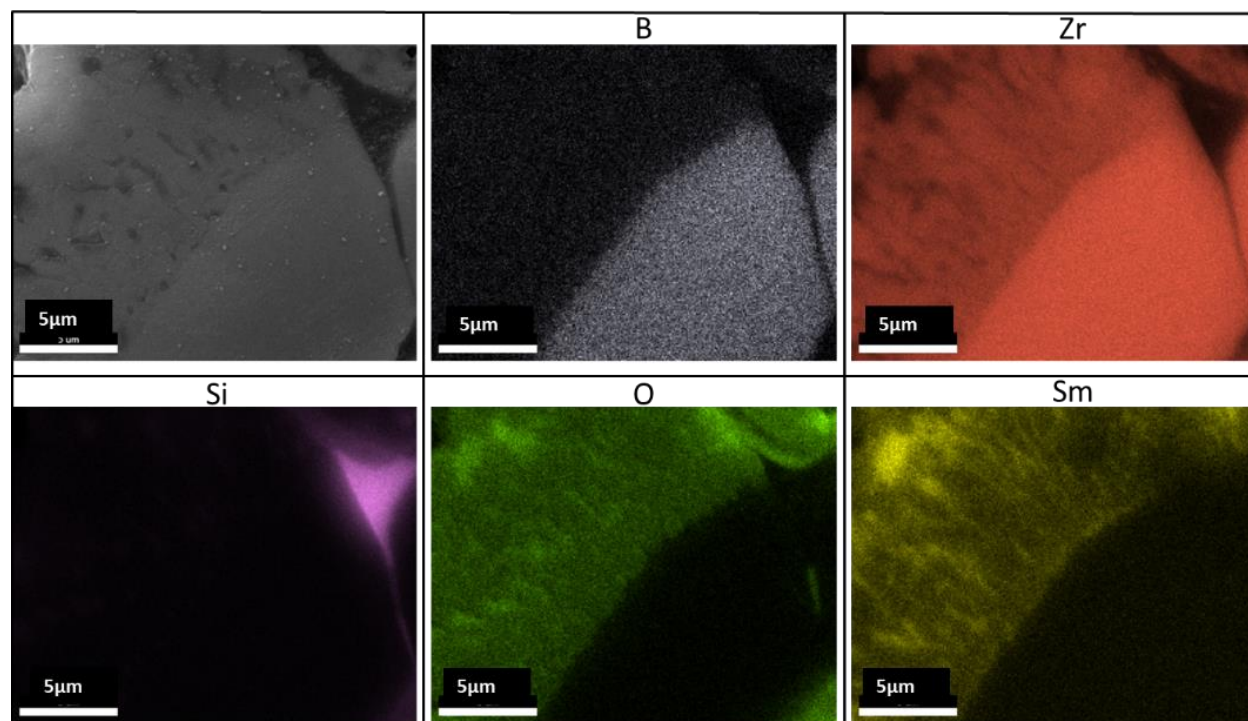


**Figure 4.6 EDS analysis post 10s of ablation in Zone 1 of a convective cell that contains an oxidizing  $ZrB_2$  grain as well as the formation of the intergranular Sm-doped silicate glassy phase.**

#### 4.2.1.2 Post 60s of Ablation

After 60s of ablation, it was observed in Figure 4.1e-f that the convective cells have erupted and large pores where the convective cells once inhabited populate the surface. When convective cells erupt, this reveals a new path for rapid inward oxygen diffusion, repeating the oxidative process described previously.<sup>38</sup> These pores are also indicative of the release of gaseous products such as CO or CO<sub>2</sub> and evaporated B<sub>2</sub>O<sub>3</sub>. This also reveals a pathway for rapid inward oxygen diffusion and again repeating the formation of evaporated B<sub>2</sub>O<sub>3</sub> and CO or CO<sub>2</sub>. This helps explain the increase in oxide scale thickness after 60s and 300s of ablation.

It can also be seen in Figure 4.1e that the oxide islands are larger. It is hypothesized that the oxide islands grow via two methods. The first is the islands start to coalesce with time. Second is grain growth out of the liquid from the formation of SZO out of Sm<sub>2</sub>O<sub>3</sub> and ZrO<sub>2</sub> which will be

described in Section 4.2. As the grains are added to by the liquid and time is increased, rapid grain growth occurs. In Figure 4.2c, after 60s of ablation the main phase present is  $c_1\text{-Sm}_{0.2}\text{Zr}_{0.8}\text{O}_{1.9}$  along with small phases of  $\text{Sm}_2\text{O}_3$  and  $\text{ZrO}_2$ . The large crystalline grains Figures 4.1e consist of mainly Zr, O, and Sm which correspond to the SZO phase seen in Figure 4.2c. A glassy phase consisting of a higher concentration of Sm and Si is also present on the surface, which correlates to the amorphous hump seen in Figure 4.2c.

#### 4.2.1.3 Post 300s of Ablation

After 300s several different microstructural features are present. From the low magnification SEM micrograph in Figure 4.1h there are large crystalline regions with massive pores, which appear to be indicative of coalescence of grains, as well as cracks (likely due to thermal shock). Crystalline regions correspond to SZO as it is the only crystalline phase present in Figure 4.2d. Cross-sectional results post 300s of ablation reveal the size of the pores increased with increased ablation time as seen in Figure 4.4e. Again, the formation of these pores is due to the buildup of evaporated glass and volatiles as well as from the continual convectional cell formation process.

When surface magnification is decreased, dendrites, islands, and large grains of SZO are present as seen in Figure 4.1h. Around each of the mentioned crystalline phases, there is Sm/Si/O glass with a small amount of Zr as depicted in Figure 4.7 of EDS of each of the mentioned regions. In the large continuously “smooth” crystalline region depicted in Figure 4.7d, glass dendrites are present on top of the grain. This suggests there was a low quantity of glass atop the surface of this zone that, when undercooled, formed the dendritic structure. This dendritic glass structure due to undercooling can also be seen in the zirconia-silica system.<sup>43</sup> In this large region there are also residual pockets of the Sm/Zr/Si/O glass only visible in BSE and EDS images. This suggests the

residual glass has a relatively high evaporation temperature. This similar behavior of the glass is also seen in ZBS doped with yttrium when  $Y_2Si_2O_7$  is formed.<sup>44</sup> SZO “islands” are also present in the sample and are surrounded by more of the glassy phase as well as seen in Figure 4.7c.

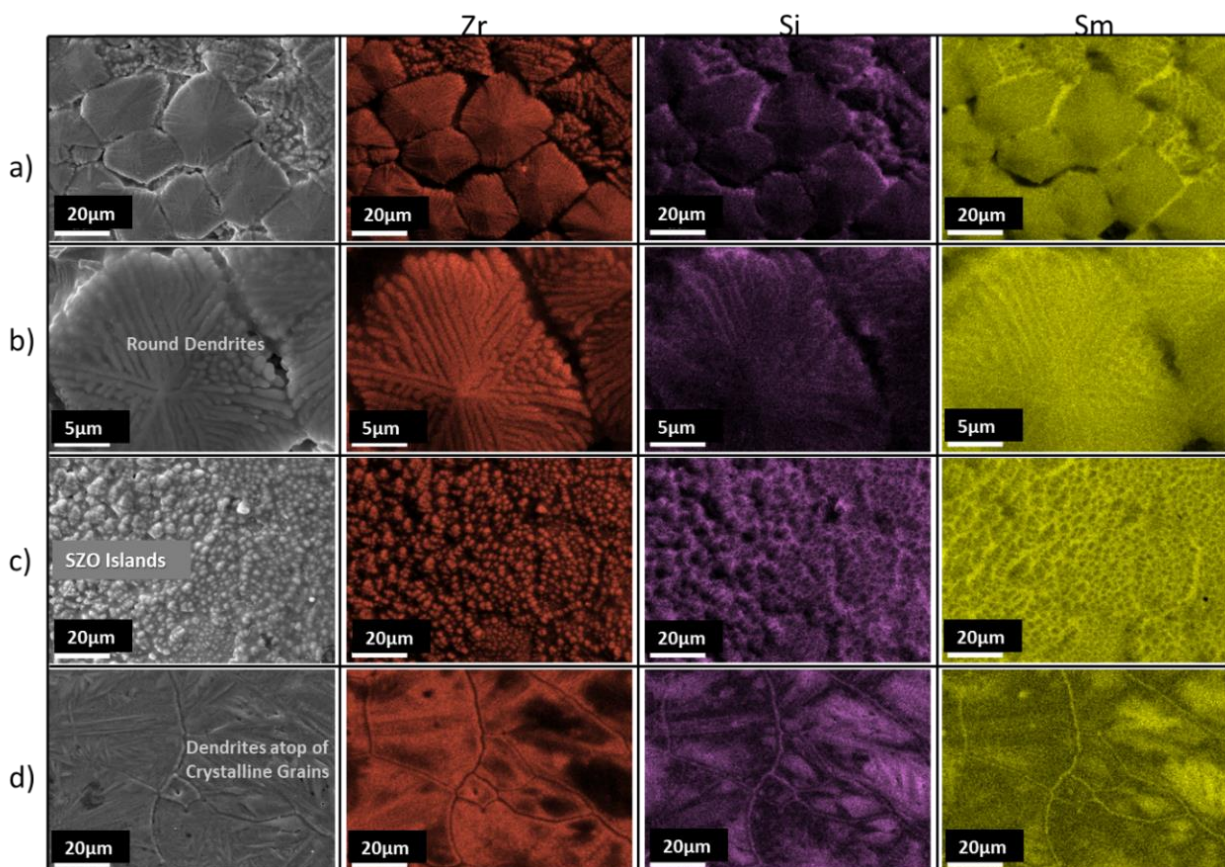


**Figure 4.7** EDS analysis of post 300s of ablation of a) round dendrites, b) higher magnification of a), c) oxide island region, and d) large uniform crystalline phase with dendrites on top.

In Figure 4.1h these islands appear to gradually form into the large crystalline region suggesting the coalescing of these islands is the reason for the formation of the large crystalline region. The large grains are also connected by crystalline dendrites.  $ZrO_2$  dendrites were also observed in 8hr furnace formed ZBS oxide scales at  $1600^\circ C$ .<sup>38</sup> It was suggested that the dendrites precipitated from super saturation of zirconia in Zr-doped borosilicate liquid and then coalesced

to form the main grains of  $ZrO_2$  islands.  $ZrO_2$  crystals deposited via a chemical vapor deposition in atmospheric pressure on a silicon substrate were found to destabilize and form a dendritic structure.<sup>45</sup> It is suggested that the destabilization of the oxide is also the case for our  $c_1$ - $Sm_{0.2}Zr_{0.8}O_{1.9}$  grain edges where the Si dominant amorphous glass is present.

There are also regions of round dendrite-like crystals surrounded by doped borosilicate glass as seen in Figure 4.7a-b. However, this network is different than those in the larger crystalline region. Similar dendrites were also observed in ablated ZBS doped with 5mol% Sm on an alumina substrate after 2 cycles of ablation.<sup>46</sup> In this study the flower-like dendrites of Sm-stabilized  $ZrO_2$  were formed via the deposition process of Sm/Al-stabilized  $ZrO_2$  precipitating from the lobes boria rich liquid surrounded by silica rich liquid.<sup>46</sup> In this system, a flower with petals pattern was not seen. Dendritic structures like these were also seen in liquid zirconia-silica systems.<sup>43</sup> The dendrites were said to arise as aggregated  $ZrO_2$  surrounded by two liquids of different Zr and Si compositions in turbulent conditions. However, the Zr containing dendrites observed in this study are clearly different than those observed in the previous studies. One possible explanation for the formation of a eutectic with the oxide and the Si containing glassy phase. The  $SiO_2$ - $ZrO_2$  phase diagram shows that  $SiO_2$  with 10mol%  $ZrO_2$  forms a eutectic at 1687°C.<sup>47</sup> Although we were higher in temperature (1870°C) we also have Sm in the system. It is suggested that in this crystalline region there was a significant amount of Sm-doped silicate glass on the surface. It is possible the glass reacted with the oxide to destabilize it and form a second liquid. As the system was cooled abruptly, the cooling rate was about the same in all directions and the eutectic microstructure was formed.

#### 4.2.2 Second Observation: Sm-doped Samples form SZO from $\text{Sm}_2\text{O}_3$ and $\text{ZrO}_2$ and Glass Transportation

As observed in Figures 4.2b and 4.2c,  $\text{Sm}_2\text{O}_3$  and m- $\text{ZrO}_2$  are present after 10s and 60s of ablation and are believed to be the first oxides to form. As shown in Figure 4.2, an amorphous hump is also present in the low  $2\theta$  region after 10s, 60s, and 300s of ablation indicating the formation of a glassy phase. The oxidation of the starting  $\text{SmB}_2\text{C}_2$  matrix and  $\text{ZrB}_2$  grains (see Figure 4.2a) results in the formation of these two oxides on the surface as well as Sm/Zr-doped  $\text{B}_2\text{O}_3/\text{SiO}_2$  (borosilicate) glass and likely gas phases to include CO or  $\text{CO}_2$ . After 10s the  $\text{SmB}_2\text{C}_2$  matrix appears to oxidize first in Zone 3 (Figure 4.5). After 10s of ablation the Sm containing matrix is clearly being oxidized, as O is only present with the Sm in Zone 3. The Zr rich regions, indicative of the  $\text{ZrB}_2$  grain, remain unoxidized. It is believed the Sm diffuses with the oxygen and dopes the Zr-rich region forming partially Sm-doped m- $\text{ZrO}_2$  (as Sm is present in the oxidized Zr region).

In Figure 4.6 it is clearly seen that the Sm and high O concentrations align in the oxidized portion of the  $\text{ZrB}_2$  grain. It can also be seen in the oxidized regions of the grain that the regions rich in Zr are doped with Sm. This is believed to be evidence of the grain transforming into partially Sm-doped m- $\text{ZrO}_2$  and  $\text{Sm}_2\text{O}_3$ . Although m- $\text{ZrO}_2$  and  $\text{Sm}_2\text{O}_3$  could not be distinguished in EDS analysis on the surface, it is believed they are in the form of nano-oxides in the glassy phase. Small oxide islands of about 500nm in the inset image in Figure 4.1c can be seen dispersed in the glassy phase and are believed to be  $\text{ZrO}_2$  and  $\text{Sm}_2\text{O}_3$ . This was the case for ablated  $\text{HfB}_2/\text{SiC}$  ceramics where nano-oxides of  $\text{HfO}_2$  were found emulsified in  $\text{SiO}_2$  glass.<sup>48</sup>

Because of the  $\text{Sm}_2\text{O}_3$  in the system studied presently, SZO develops on the surface as observed in XRD results after 60s (Figure 4.2c) as the primary oxide present, and after 300s as the single crystalline phase present (Figure 4.2d). This is due to the reaction of  $\text{Sm}_2\text{O}_3$  and  $\text{ZrO}_2$ . The

$\text{Sm}_2\text{O}_3/\text{ZrO}_2$  phase diagram shows that at  $1700^\circ\text{C}$  ~11 mol%  $\text{Sm}_2\text{O}_3$  is needed to react with  $\text{ZrO}_2$  to form SZO.<sup>49</sup> Although we only start out with 3 mol% Sm in the system, there is a concentration of 23 mol% Sm on the surface after 300s of ablation. Tan et. al.<sup>31</sup> also found a higher concentration of Sm on the surface of plasma sprayed coatings of Sm-doped ZBS after 60s of ablation at similar conditions.

The increase in Sm is due to the Sm-doped amorphous glassy phase being forced to the surface through the formation, flow, and bursting of convectional cells (described more fully in Section 4.2.1). Cross-sectional analysis in Figure 4.5 revealed a depletion region of Sm between Zones 2 and 3 after 60s of ablation. Zone 2 depicts an active oxidation region compared to Zone 1 where the oxide is finished forming. As the Sm incorporates into the Si rich regions and as the oxidation of  $\text{ZrB}_2$  to  $\text{ZrO}_2$  occurs (although slightly Sm-doped according to EDS), the Sm is still being pushed up to the surface forming the gap seen in Figure 4.5. The formation of this liquid depletion region is also seen in  $\text{ZrB}_2/\text{SiC}$  and  $\text{HfB}_2/\text{SiC}$  systems for Si regions.<sup>19,48,49</sup> Evidence of the glass being forced through pores and grain boundaries can be seen after 60s and 300s in Figure 4.5 from the higher concentration of Sm in Zone 1. The glassy phase located at grain boundaries in Zone 1 is also evident in Figure 4.4f. This increase of Sm-doped silica provides enough Sm to form the SZO phase. As the billet is oxidized and  $\text{B}_2\text{O}_3$  and  $\text{SiO}_2$  evaporates the surface, the Sm concentration increases. This evaporation allows for the  $\text{Sm}_2\text{O}_3$  and  $\text{ZrO}_2$  to react and form SZO.

### 4.3 Conclusion

The microstructural evolution of ablated samarium-doped zirconium diboride/silicon carbide was investigated to understand the formation of the  $c_1\text{-Sm}_{0.2}\text{Zr}_{0.8}\text{O}_{1.9}$  oxide layer and its constituent components. It was found that SZO phase is formed by first forming oxides of  $\text{Sm}_2\text{O}_3$  and  $\text{ZrO}_2$  due to the oxidation of  $\text{ZrB}_2$  and the samarium containing matrix. Samarium also seems

to be transported with the oxygen during ablation in what is believed to be an oxide in to the zirconium regions as well as incorporate into the amorphous Si regions. As the Sm incorporates into and transports with the silica glass it forms a depletion region as well as provides enough Sm to form  $c_1\text{-Sm}_{0.2}\text{Zr}_{0.8}\text{O}_{1.9}$ . The formation of convectional cells and the coalescing of the oxides proceeds to have grain growth and dendritic structures formed from a possible eutectic with the amorphous phase.

## 5. MICROSTRUCTURAL EFFECTS ON ABLATION AND EMITTANCE BEHAVIOR OF SAMARIUM-DOPED ZIRCONIUM DIBORIDE/SILICON CARBIDE CERAMICS

### 5.1 Results

#### 5.1.1 As Sintered Microstructure and Phase Analysis

The density, open porosity, average surface roughness, and maximum ablation temperature of the different billets are listed in Table 5.1. The pre-tested topography in Figure 5.1a shows a relatively smooth surface with some porosity which is expected. Figure 5.1b and 5.1c reveal rougher surfaces compared to Figure 5.1a. This coincides with increasing R number (surface roughness) in Table 5.1. The same trend can also be seen for density or D number.

**Table 5.1 Measured densities, porosities, surface roughness of pre-heated billets and maximum temperatures reached during oxyacetylene ablation.**

<b>Sample</b>	<b>Density (%)</b>	<b>Open Porosity (%)</b>	<b>Ra (<math>\mu\text{m}</math>)</b>	<b>Max Ablation Temperature (<math>^{\circ}\text{C}</math>)</b>
D1R1	87	7.5	0.4 $\pm$ 0.1	1656
D1R2	87	7.5	0.9 $\pm$ 0.2	1768
D1R3	87	7.5	1.4 $\pm$ 0.3	1818
D2R1	79	14	1.0 $\pm$ 0.2	1763
D3R1	69	24	1.1 $\pm$ 0.2	1855

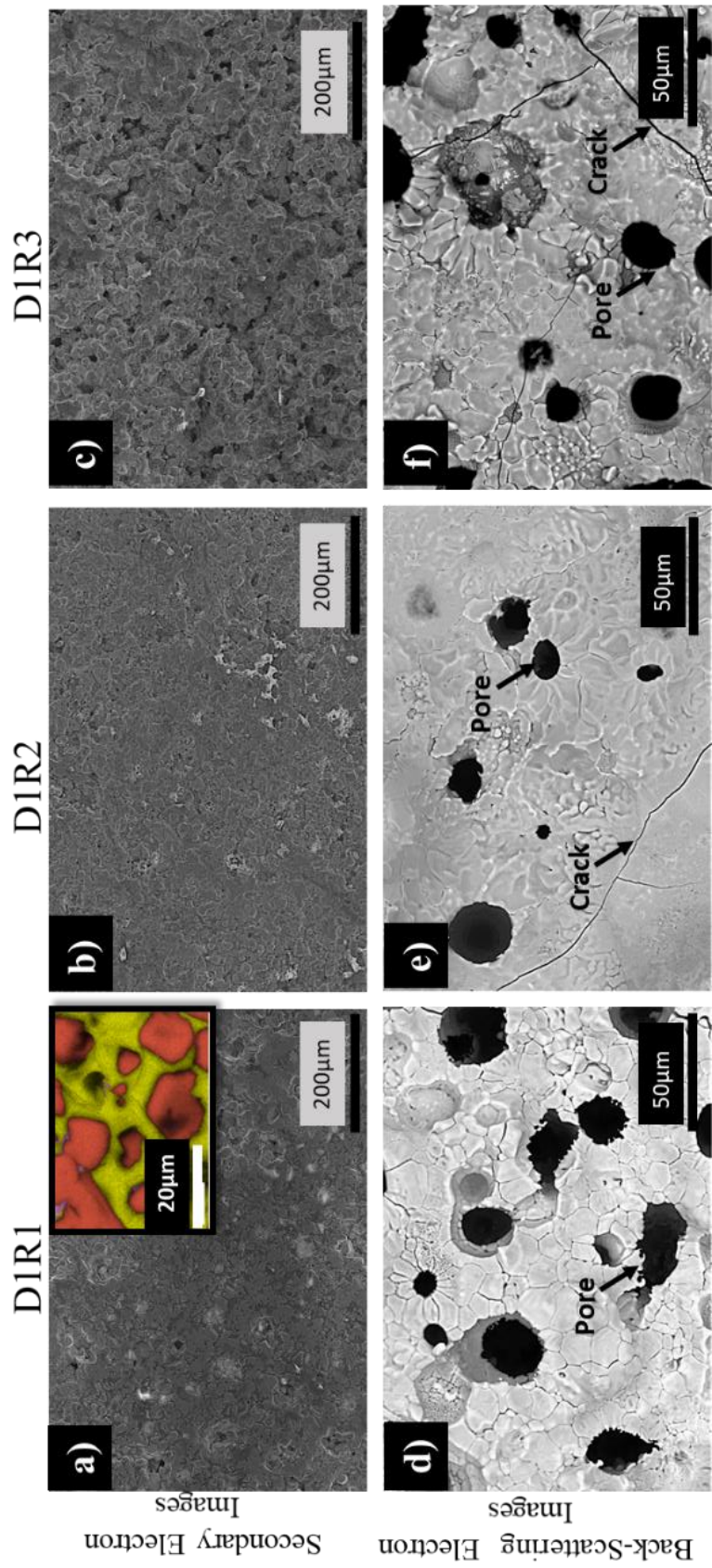


Figure 5.1 SEM images of pre- and post-ablated billet surfaces DIR1, DIR2, and DIR3.

The cross-section of the sample in Figure 5.2a reveals a denser microstructure compared to Figure 5.2b and 5.2c. The pre-ablation phases present in the different samples are listed in Table 5.2 as well as shown in Figure 5.3a. Pre-ablation of D1R1, D1R2, and D1R3 show the main crystalline phase is  $ZrB_2$  with small peaks corresponding to  $SmB_2C_2$  and  $ZrC$ . The oxidation of the  $SiC$  to  $SiO$  and  $CO$  during sintering coupled with the degradation of  $Sm_2O_3$  from the pre-sintered powders in the reducing atmosphere is believed to result in the formation of the  $ZrC$ ,  $SmB_2C_2$ ,  $SmBO_3$ , and loss of  $SiC$  in the billets. Similar reactions also occurred with pressureless sintered  $Y_2O_3/SiC$ .<sup>38</sup> The excerpt image seen in Figure 5.2a shows the  $ZrB_2$  grains are surrounded by a  $SmB_2C_2$  matrix. Little pockets of  $SiC$  are seen; however,  $ZrC$  and  $SmBO_3$  could not be distinguished in EDS. Pre-ablation of D2R1 show the same phases present, however with the addition of minuscule peaks of  $SmBO_3$ . D3R1 show similar phases present as D2R1; however, the intensity of the  $ZrC$  peaks have increased. It is believed the sintering temperature used to obtain a 69% density for D3R1 was the optimal temperature to form the  $ZrC$ .<sup>50</sup>

**Table 5.2 Phases present in pre-ablated and post-laser-ablated billets as well as maximum temperature reached at each power condition.**

Sample	Pre-ablation Phases	Post-Ablation Phases	Max Temperature Reached (°C) Per Power		
			700W	800W	900W
D1R1	$ZrB_2$ , $SmB_2C_2$ , $ZrC$	$m-ZrO_2$ , $Sm_2O_3$ , $c_1-Sm_{0.2}Zr_{0.8}O_{1.9}$	2108	2094	2226
D1R2	$ZrB_2$ , $SmB_2C_2$ , $ZrC$	$m-ZrO_2$ , $Sm_2O_3$ , $c_1-Sm_{0.2}Zr_{0.8}O_{1.9}$	1878	2009	2133
D1R3	$ZrB_2$ , $SmB_2C_2$ , $ZrC$	$m-ZrO_2$ , $Sm_2O_3$ , $c_1-Sm_{0.2}Zr_{0.8}O_{1.9}$	1937	2041	2179
D2R1	$ZrB_2$ , $SmB_2C_2$ , $ZrC$ , $SmBO_3$	$m-ZrO_2$ , $Sm_2O_3$ , $c_1-Sm_{0.2}Zr_{0.8}O_{1.9}$	2197	2407	2327
D3R1	$ZrB_2$ , $SmB_2C_2$ , $ZrC$ , $SmBO_3$	$m-ZrO_2$ , $Sm_2O_3$ , $c_1-Sm_{0.2}Zr_{0.8}O_{1.9}$	1990	2142	2231

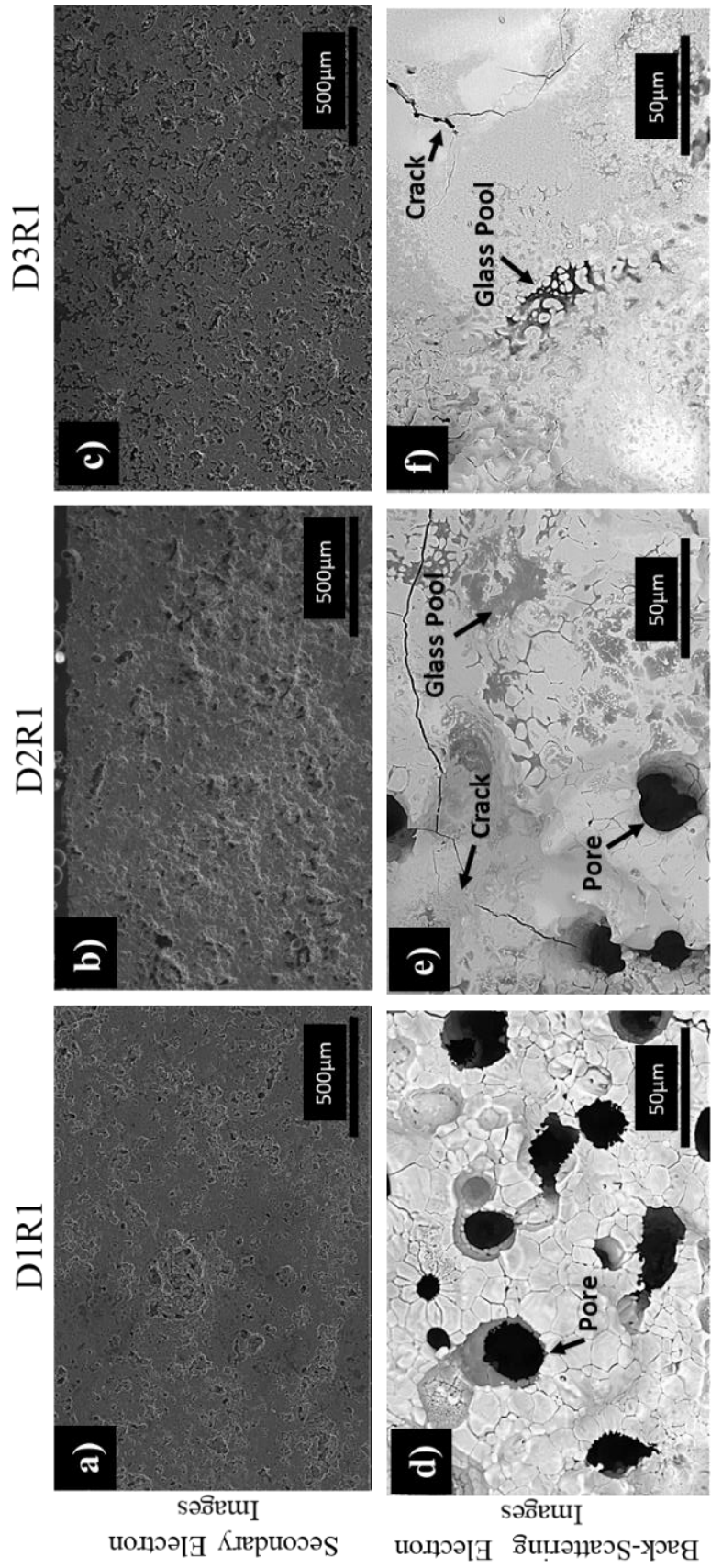
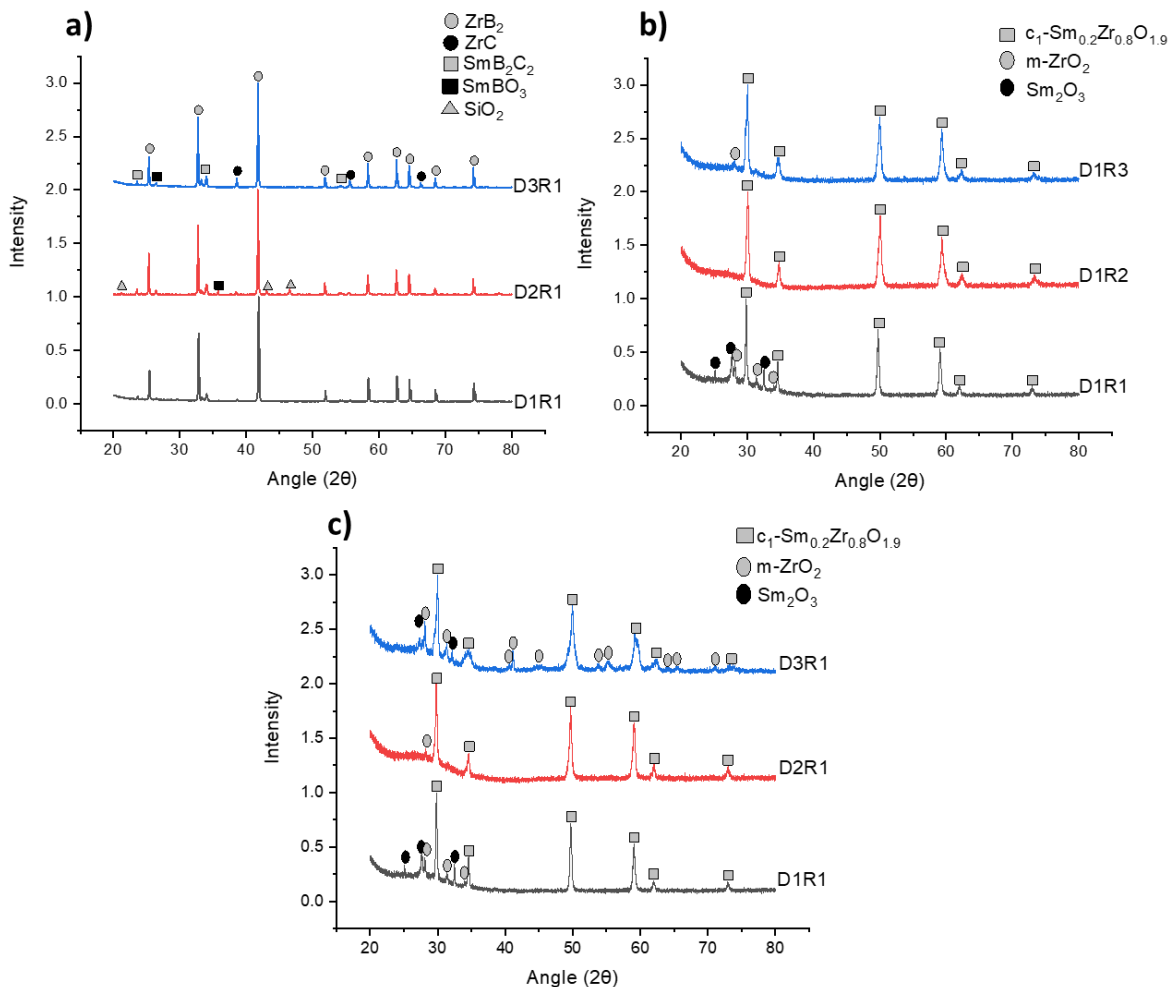


Figure 5.2 SEM images of pre-ablated cross-sections of a) D1R1, b) D2R1, and c) D3R1 as well as post-ablated billet surfaces d) D1R1, e) D2R1, and f) D3R1.

## 5.1.2 Post-ablation Properties of Sm-doped ZBS with Different Roughness and Porosities

### 5.1.2.1 Samples with Different Surface Roughness

The post ablated surfaces of D1R1, D1R2, and D1R3 show there is little difference in microstructure as seen in Figure 5.11d-f. Large crystalline grains can be seen lightly covered by a glassy phase that is also present between the grain boundaries. Large pores dispersed throughout the surface also help to make up a rough topography, indicative of the release of gaseous products such as CO, CO<sub>2</sub>, and evaporated glass from oxidation. XRD results in Figure 5.3b show the main phase present post 60s of ablation for D1R1-D1R3 is  $c_1\text{-Sm}_{0.2}\text{Zr}_{0.8}\text{O}_{1.9}$  (SZO). The samples also show an amorphous hump in Figures 5.3b and 5.3c, which is consistent with the glassy phase observed in Figures 5.1d-f. D1R1 and D1R3 show evidence of the formation of m-ZrO<sub>2</sub> and Sm<sub>2</sub>O<sub>3</sub>. These oxides are the first to form in this system and proceed to combine to form SZO as described in Chapter 4.



**Figure 5.3 XRD of a) pre-ablated billets, b) post-ablated billets of different surface roughness, and c) post-ablated billets of different density percent.**

Cross-sectional micrographs seen in Figure 5.4 show oxide thicknesses of  $\sim 200\mu\text{m}$ ,  $\sim 300\mu\text{m}$ , and  $\sim 300\mu\text{m}$  for D1R1, D1R2, and D1R3, respectively. EDS analysis of the cross-sectional regions in Figure 5.4 show three distinct zones: Zone 1, which is the main oxide scale, Zone 2, which is the transition region and an area of active oxidation, and Zone 3, where the SmB<sub>2</sub>C<sub>2</sub> starts to oxidize, but the ZrB<sub>2</sub> grains remain untouched. In Zone 1 the Sm and Zr elements can be seen dispersed amongst each other indicating the formation of SZO. In Zone 2, there is a higher concentration of Zr that is slightly doped with Sm as seen by the brighter red, with a depleted Sm

concentration surrounding the Zr rich regions. This coincides with the Si depleted region as Sm is found to incorporate into the Si containing glassy phase, which is pushed up to the surface during oxidation as described in Chapter 4. As surface roughness increases, the Sm depleted region becomes larger as seen in Figure 5.4.

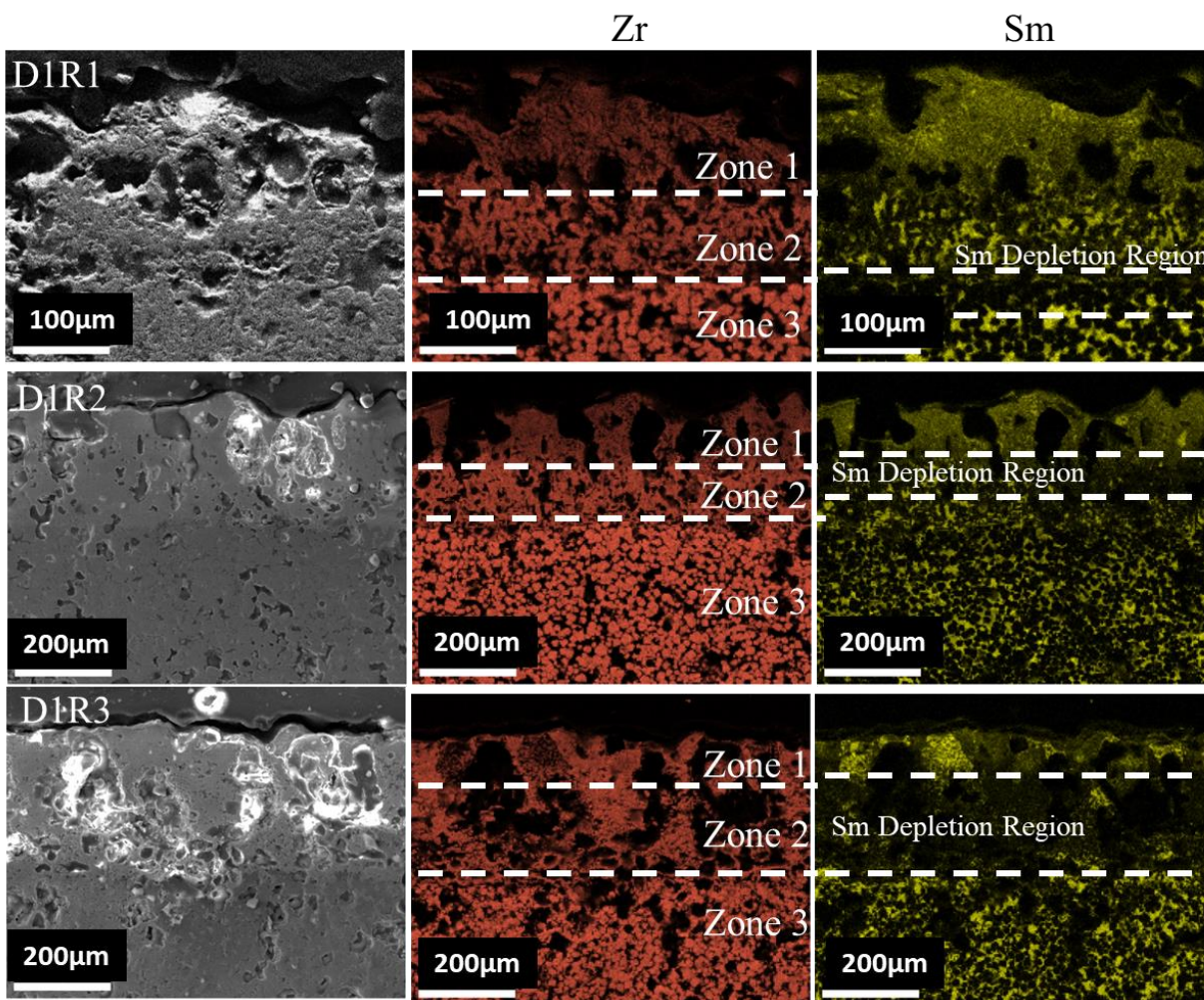


**Figure 5.4 EDS analysis of D1R1, D2R1, and D3R1.**

### 5.1.2.2 Samples with Different Porosities

The post-ablated surfaces of D1R1, D2R1, and D3R1 in Figure 5.2d-f show the higher porosity samples have pools of glass amongst the crystalline regions compared to D1R1, which has the glassy phase dispersed evenly across the surface. The XRD post ablation in Figure 5.3c

shows D1R1 and D3R1 have remnant m-ZrO<sub>2</sub> and Sm<sub>2</sub>O<sub>3</sub> present, more so D3R1 with numerous peaks correlating to m-ZrO<sub>2</sub>. This excess m-ZrO<sub>2</sub> in D3R1 is believed to be due to a higher quantity of ZrC pre-ablation. However, all samples show the main phase present is SZO. Cross-sectional images in Figure 5.5 reveal oxide thicknesses to be ~200μm for both D1R1 and D2R1, and D3R1 to be ~400μm. As starting open porosity increases, larger amounts of trapped glass are seen in Zone 1, indicated by the high Sm concentration as well as the disappearance of the Sm-depletion region as seen in Figure 5.5.

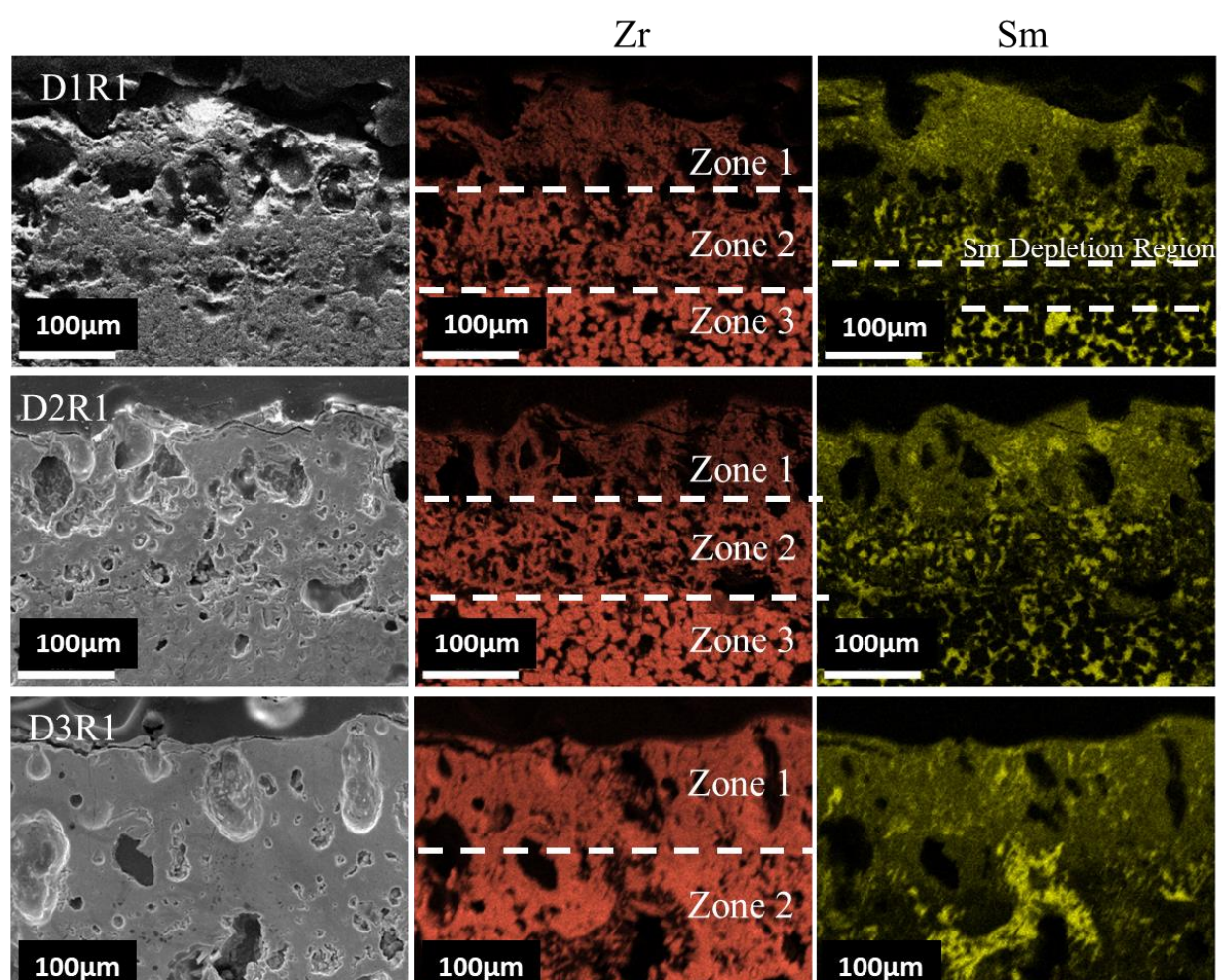


Figure 5.5 EDS analysis of D1R1, D2R1, and D3R1.

### 5.1.3 Post-laser Heated Microstructures of of Sm-Doped ZBS with Different Surface Roughness and Porosities

The post ablated surfaces of the samples with different surface roughness and porosities show there is little difference in microstructure as seen in Figure 5.6 except for D3R1 (Figure 5.6d). Crystalline grains can be seen surrounded by a glassy phase. Post ablation XRD in Figure 5.7 reveals the crystalline regions to be  $m\text{-ZrO}_2$ . Two small peaks also correspond to  $\text{Sm}_2\text{O}_3$  and  $c_1\text{-Sm}_{0.2}\text{Zr}_{0.8}\text{O}_{1.9}$ . Although only one of the samples is shown, all the billets tested resulted in the same XRD pattern.

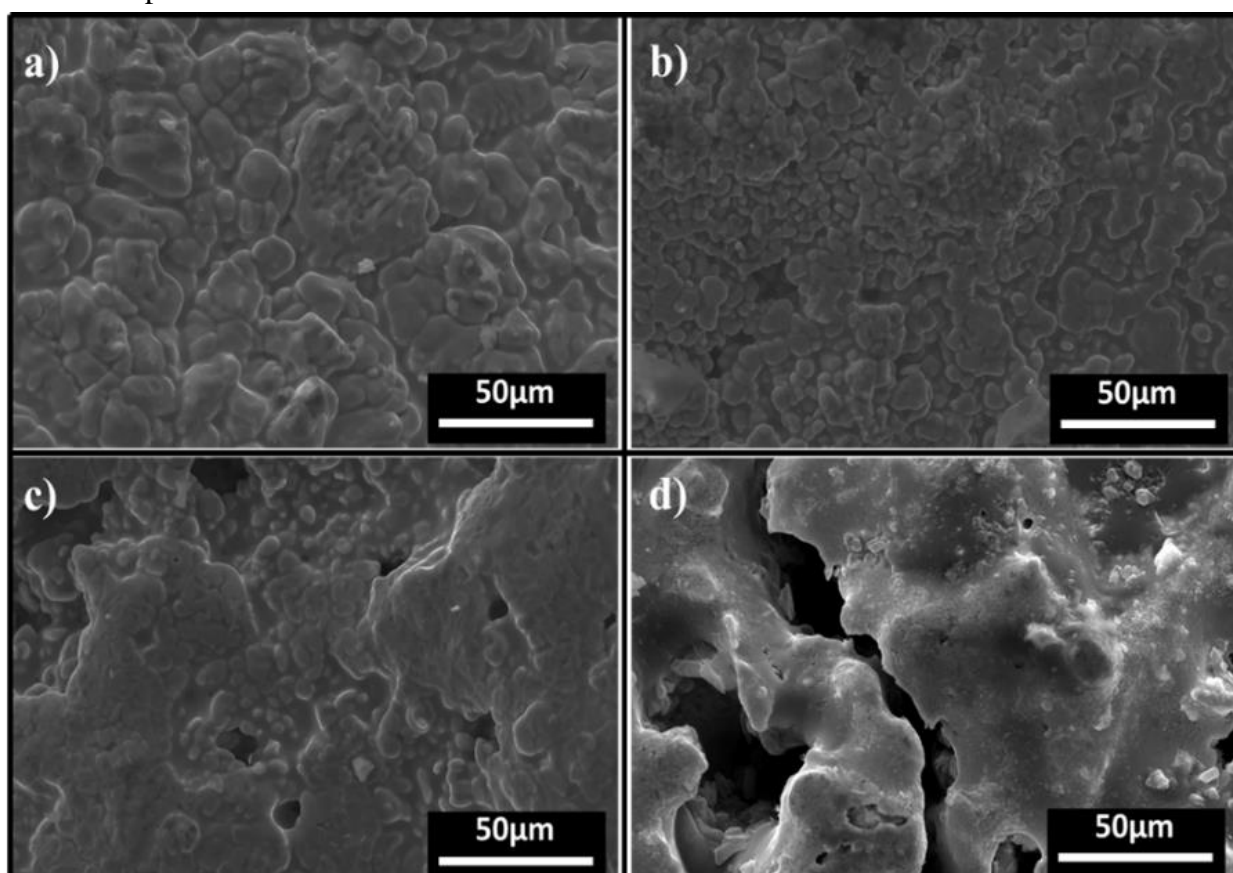
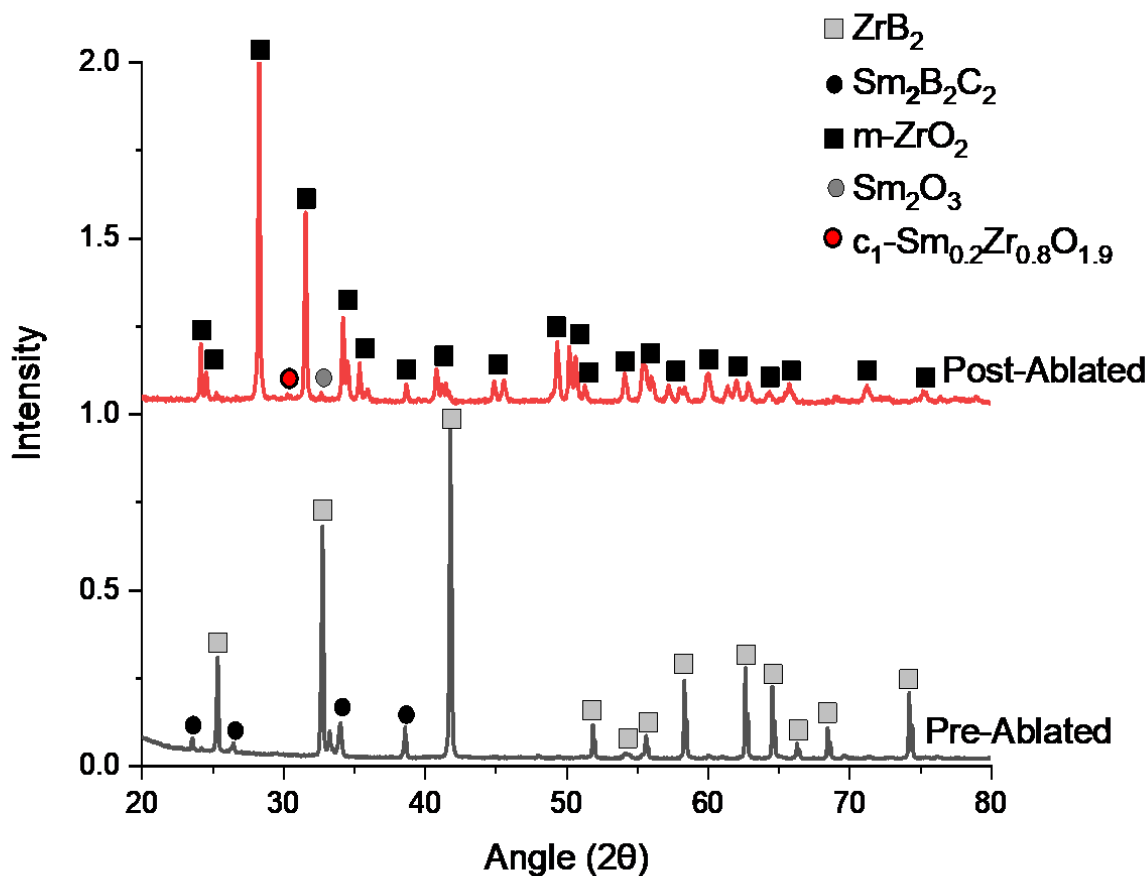


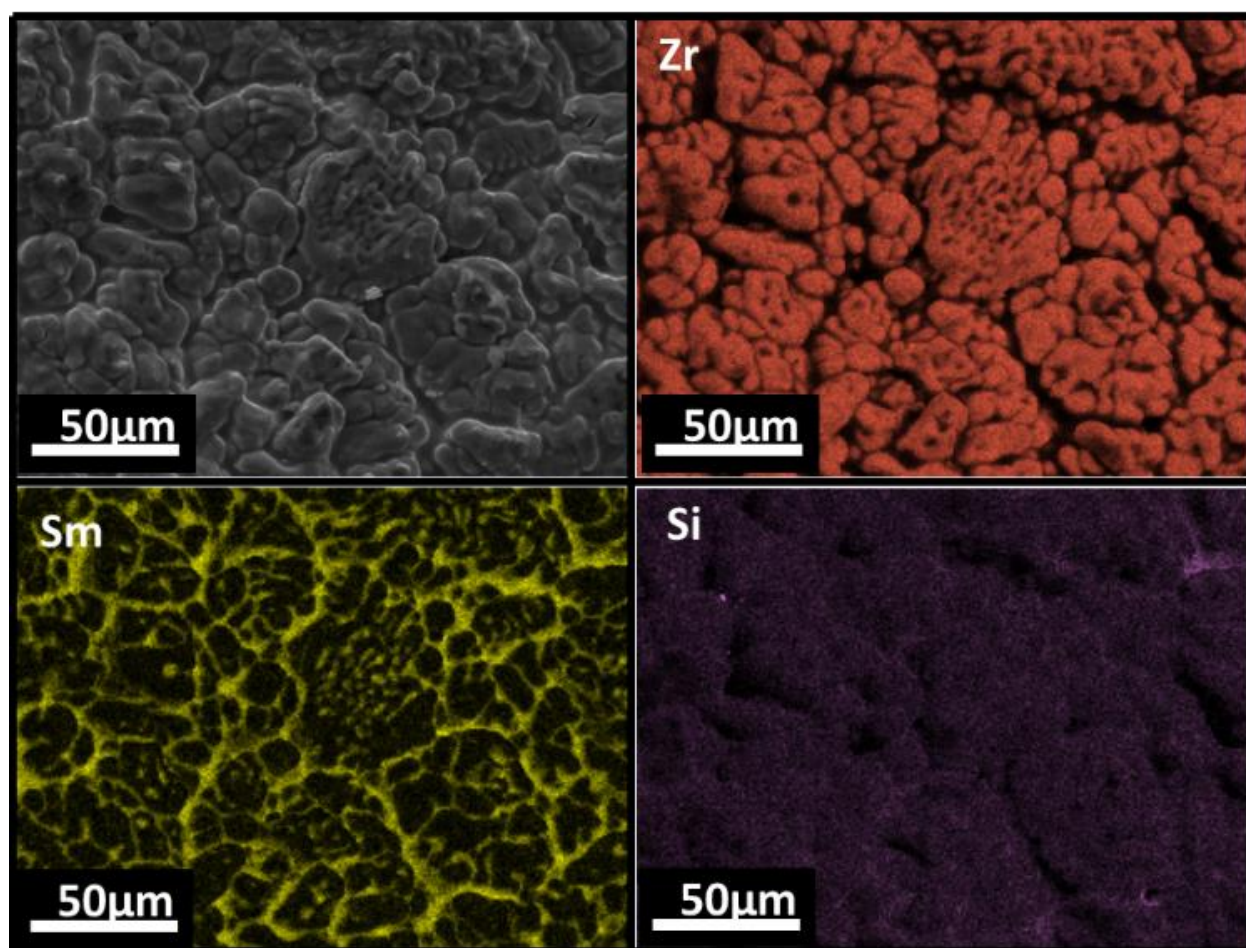
Figure 5.6 SEM SE micrographs of post-laser ablated a) D1R2, b)D1R3, c)D2R1, and d)D3R1.



**Figure 5.7 XRD of pre- and post-ablated billet surfaces of D1R2**

Although Figure 5.6d reveals a different microstructure to Figure 5.6a-c, the post-ablation XRD pattern also was the same as seen in Figure 5.7. The topographical microstructure for Figure 5.6d shows large linear pores like cracks as well as crystalline regions covered by a glassy phase. It is unsure why the microstructure is different than the others, but one possible explanation is that the starting open porosity was large enough that as it oxidized, the glass evaporated quickly, decreasing the chance to cover the surface and precipitate out oxide to fill the gap. It is also important to note that the samples were laser heated on the opposite side of what was done for oxy-acetylene heating. In Figure 5.8, the sample had radiance recorded on the radiance side (Figure 5.8a) and were heated on the laser side (Figure 5.8b), which was clearly more oxidized, as indicated

by the ball of oxide. EDS analysis (Figure 5.9) reveals the crystalline regions consist of mainly Zr while the amorphous regions consist mainly of Sm and Si. The table in Figure 5.9 reveals there is little Si in the system; however, with the temperature exceeding 1900°C, this is expected as after 1600°C the Si starts to evaporate.<sup>29,38,40</sup>



Phase	Zr	Sm	Si	O	C
	At%	At%	At%	At%	At%
Crystalline	21	3	2	49	26
Amorphous	6	16	4	56	17

**Figure 5.8 EDS analysis of D1R1 after 60s of holding at 900W. Table shows the compositions of the crystalline and amorphous phases.**

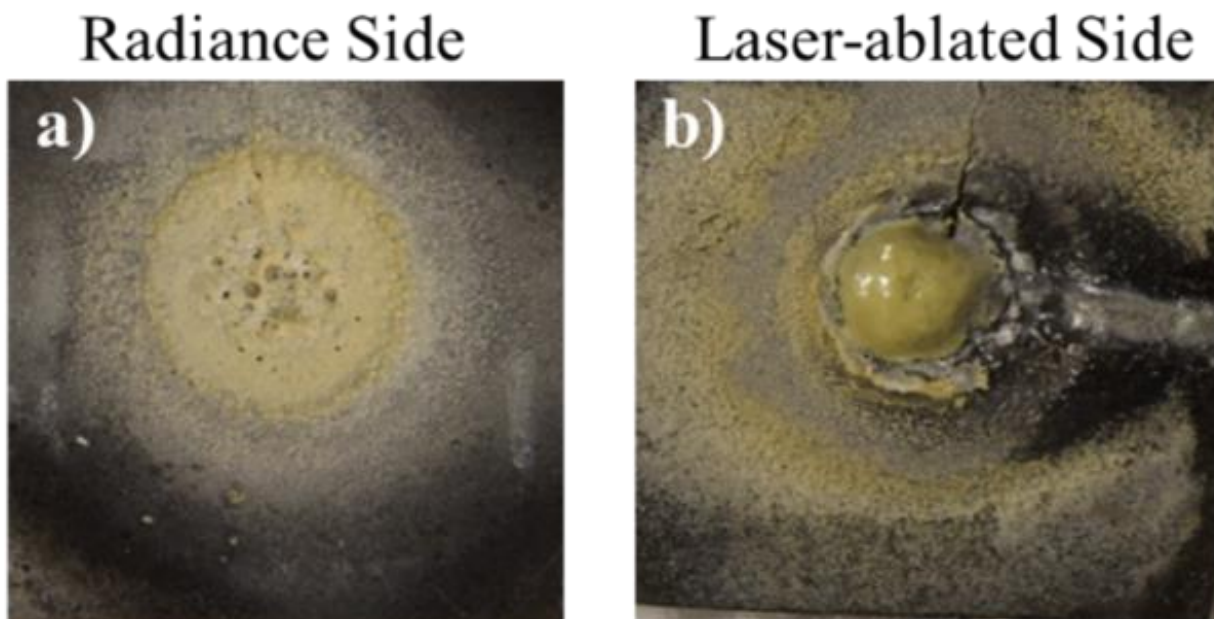


**Figure 5.9** Spectrometer side where radiance data was collected and b) laser ablated side where sample was heated.

#### **5.1.4 Spectral Emittance of Sm-doped ZBS with Different Surface Roughness and Porosities**

Emittance testing resulted in virtually identical results for all samples tested. It should be noted that the large peaks at  $\sim 2200\text{nm}$  are a result of noise in the pixel and are not true peaks. Temperatures experienced by the samples increased as the power setting increased, as seen in Table 5.2. Emittances as a function of wavelength at  $2100^\circ\text{C}$  (Figure 5.10a and 5.10b) reveal, despite changing the surface roughness or porosity, changes in emittance were essentially non-existent. Figure 5.10c and 5.10d showing emittance as a function of wavelength at  $1600^\circ\text{C}$  also show there is little difference in starting surface roughness and porosity, except for D1R3 and D3R1 where the emittance is slightly lower than the other samples.

The slight differences in emittance in Figure 5.10 indicate there may be differences in emittances as a function of time. It can be seen in Figure 5.11 that this is the case, with slight differences in the emittance as a function of wavelength can be seen. As time increases up to 40s,

the emittance drops slightly. After 40s the emittance begins to rise again. This indicates that there was a transformation occurring on the surface of the billet.

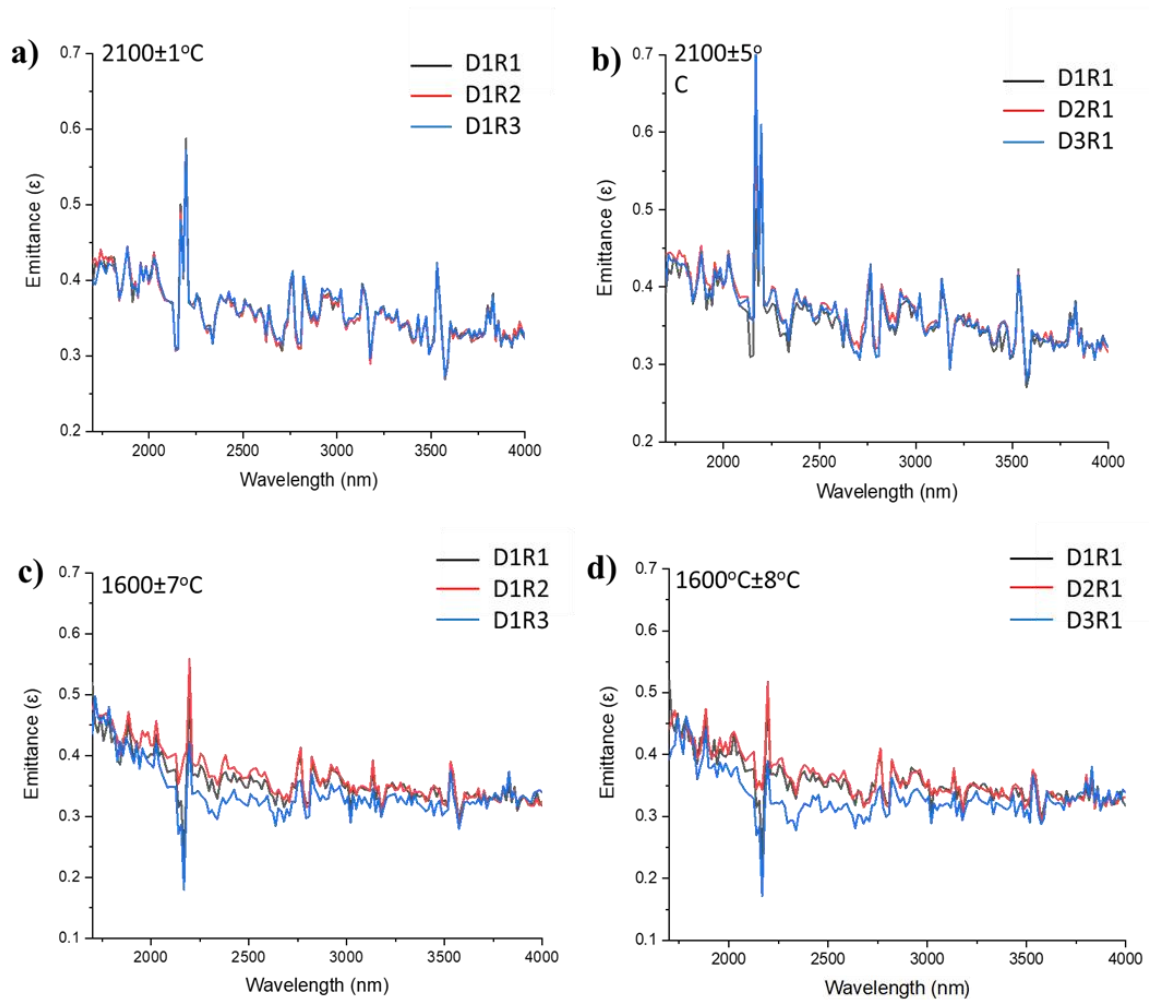


**Figure 5.10 Emittance vs wavelength graphs of a) different surface roughness at 2100°C, b) different porosities at 2100°C, c) different surface roughness at 1600°C, and d) different porosities at 1600°C.**

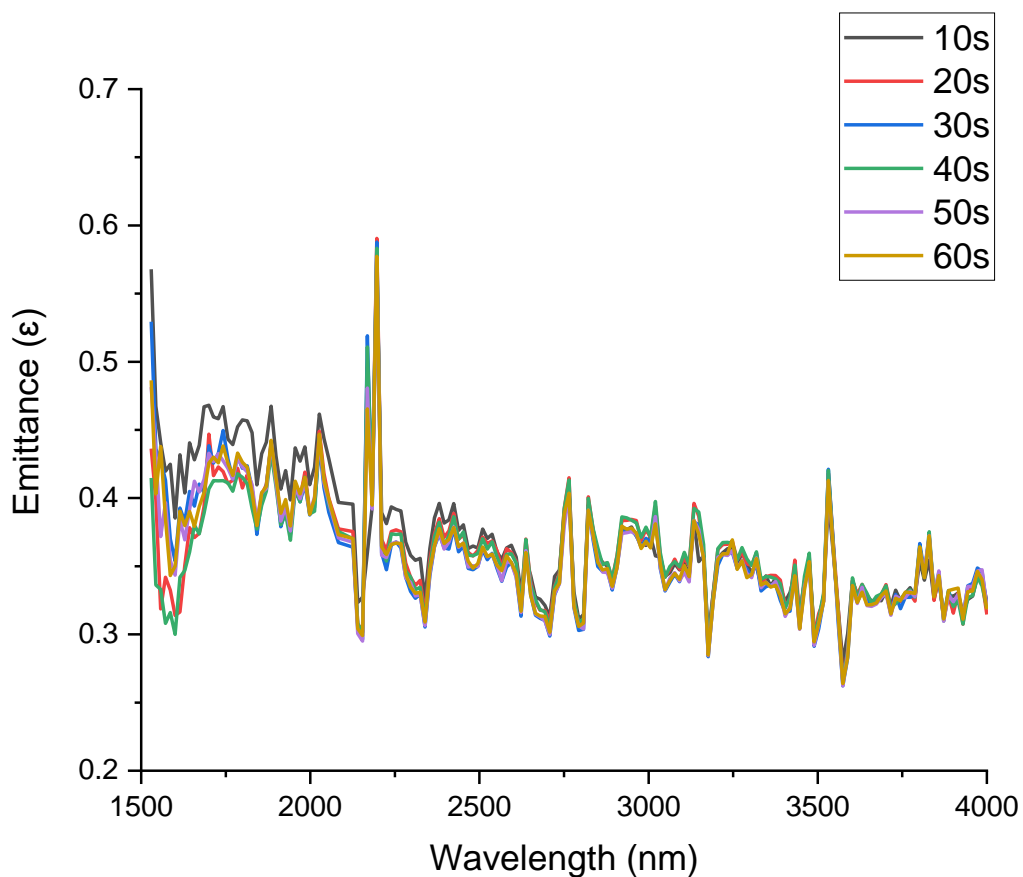


**Figure 5.11 Emittance as a function of wavelength at different time intervals for D1R2**

Differences in temperature due to power were likely due to differences in sample thicknesses. Despite the increase in temperature, sample emittance remained relatively constant, as seen in Figure 5.12. XRD results in Figure 5.6 also show all samples formed  $m\text{-ZrO}_2$  upon laser heating, as mentioned in Section 5.1.2.4. It should be noted again that the side where radiance was measured was the non-laser heated side and conditions were not like the oxyacetylene ablation experiment and was likely the reason for not forming  $c_1\text{-Sm}_{0.2}\text{Zr}_{0.8}\text{O}_{1.9}$  as was seen in the ablation experiments.

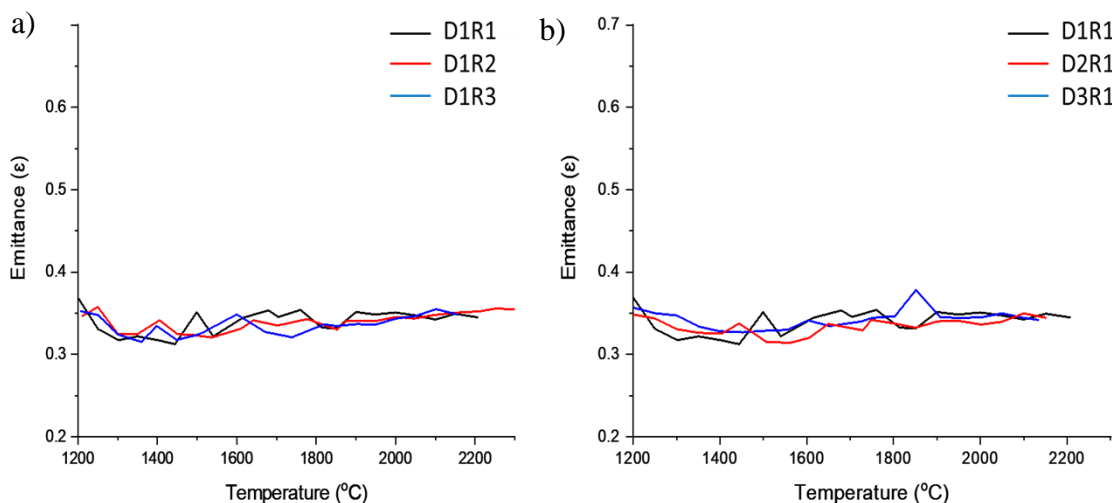


**Figure 5.12 Emittance as a function of temperature for samples of a) different surface roughness and b) porosities.**

## 5.2 Discussion

### 5.2.1 Increase in Surface Roughness and Porosity Results in Higher Surface Temperatures

Table 5.1 displays the maximum ablation temperatures reached for different surface roughness and porosities. It can be seen in Table 5.1 that as Ra and porosity increase, the surface temperature increases. A likely explanation for this may be that a larger exposed surface area absorbs and emits more heat, causing it to heat faster.<sup>51</sup> Because the exposed surface area is increased with increasing R number as well as with increased porosity, this allows for more of the material to be exposed to the flame for heating. In a study performed by Guo et. al. on how the surface roughness affects the heat transfer on film cooled nozzle guides for gas engine turbines, it was found that an increase in surface roughness increased the heat transfer coefficient, therefore increasing the heat output.<sup>52</sup> Also, as mentioned in Chapter 1, as the surface roughness increased in leading edges for wall jets at hypersonic speeds, the skin friction also increased leading to

increased heating of the system.<sup>26,28</sup> Although we were nowhere near turbulent hypersonic conditions in this study, the fact that surface temperatures were increased, can still be applied.

In Figure 5.3b, as Ra increased, the only crystalline phase present was SZO. With increased surface temperatures, this likely allowed for the faster formation of SZO, which forms at  $\sim 1700^\circ\text{C}$ .<sup>53</sup> Figure 5.3b of D1R1 shows residual oxides of m-ZrO<sub>2</sub> and Sm<sub>2</sub>O<sub>3</sub>. As the maximum temperature reached after 60s was  $1656^\circ\text{C}$ , it makes sense that we see these oxides. Figure 5.4b of D1R3 also shows a m-ZrO<sub>2</sub> peak; however, this is believed to be due XRD peaks hitting Zone 2, which contains a high Zr region correlating to the m-ZrO<sub>2</sub>. This is due to a thinner Zone 1, as seen in Figure 5.4 for D1R3. In Figure 5.3c, we also see an abundant amount of m-ZrO<sub>2</sub> post 60s of ablation for D3R1. One possible explanation for the increase in m-ZrO<sub>2</sub> is believed to be due to the starting amount of ZrC in the pre-ablated billet, as seen in Figure 5.3a for D1R3. ZrC begins to oxidize to form m-ZrO<sub>2</sub> at  $\sim 400^\circ\text{C}$ , while ZrB<sub>2</sub> begins to oxidize at  $\sim 600^\circ\text{C}$ .<sup>29,54</sup> Studies done by Liu et. al.<sup>55</sup> also found that in ZBS systems with ZrC, the ZrC acts to mechanically strengthen the outer oxide layer compared to SiO<sub>2</sub> because it is the first phase to oxidize. This then acts to increase the oxidation resistance of the material as well as inhibit the Si depletion region.<sup>55</sup> ZrC has also been found to help form a dense ZrO<sub>2</sub> layer in C-C/SiC/ ZrC systems under oxy-acetylene ablation, which helps protect the system from further oxidation.<sup>56</sup> However, this is not the case for our composite, as the amount of ZrC in our system did not have a significant effect on the oxide scales density, as seen in Figure 5.5.

However, this does not explain why the Sm was not incorporated as much compared to D1R1 and D2R1. A likely explanation is due to the open porosity, oxygen penetration was deeper and oxidized the Si beneath the surface faster. The Si glass likely transported more quickly to the surface, leaving less time for Sm to incorporate into the glassy phase. With the lack of Sm on the

surface, there may have not been enough for it to react with the  $\text{ZrO}_2$  to form SZO. This will be explained in more depth in Section 5.2.3.

### **5.2.2 Surface Roughness Does Not Make a Difference in Post-Ablation Topographical Microstructure Due to Glass Formation, but Does Affects Sm in Oxide Scale**

The post topographical microstructures in Figure 5.1d-f show despite differences in beginning surface features, the resulting microstructure is the same. This is believed to be due to the oxidative behavior of the material. When the Sm-ZBS oxidizes, it initially forms  $\text{Sm}_2\text{O}_3$ ,  $\text{ZrO}_2$  and a Sm-doped borosilicate glassy phase, as described in Chapter 4. The initial crystalline oxides  $\text{Sm}_2\text{O}_3$  and  $\text{ZrO}_2$  can be seen in the XRD for D1R1 in Figure 5.3b. The surface is initially covered by this glassy phase resulting from the formation and bursting of convectional cells.<sup>19,38,40</sup>  $\text{ZrO}_2$  is known to precipitate out of the liquid phase and grow into larger crystals.<sup>19,38</sup> As the boron and silica glass evaporate, the two oxides combine and form SZO, as described in Chapter 4. Because the formation of the oxide is initially covered in glass, and is formed due to the evaporation of the glassy phase as well as oxidation, it is believed the initial surface roughness is negated.

Cross-sectional results in Figure 5.4 show differences in the cross-section due to surface roughness despite having similar topographical features. D1R2 and D1R3 have larger oxide scales than D1R1 by  $\sim 100\mu\text{m}$  and  $200\mu\text{m}$ , respectively. EDS mapping in Figure 5.4 reveals that increased surface roughness results in a larger Sm-depletion region. This also results in a larger Si gap, as the majority of the Sm incorporates into the glassy phase, as described in Chapter 4. One plausible explanation for this could be due to the increased surface temperatures during ablation. As temperatures increase, the amount of silica containing glassy phase that evaporates increases. As the protective glassy layer is removed from the surface, the porous oxide layer underneath is exposed. This leads to deeper O penetration as well as the oxidation of the  $\text{ZrB}_2$  grains underneath.<sup>19,38,40</sup> With the expansion of the  $\text{ZrB}_2$  grains forming the oxides, as well as some

capillary action, the Sm-doped silicate glassy phase is forced to the surface.<sup>19,38,40</sup> This leaves a Sm and Si gap in the sample. Therefore, with increased surface temperature there is a larger gap.

### **5.2.3 Increasing Porosity Results in Glass Pools on Surface and Decrease in Sm-Depletion Region**

Despite higher temperatures for increased porosity, as seen in Figure 5.3d-f, larger pools of Sm-doped silica containing glassy phase remain for D2R1 and D3R1. This can be explained by the pre-ablated microstructure. Higher porosity samples expose more surface area than denser samples.<sup>56</sup> The exposed surface area increases the chance for oxidation to occur, which results in a larger amount of glass formed. When ablation of the sample occurs, oxygen is transported further into the sample. The higher surface area due to porosity exposes additional material of the sample, creating more oxidative products such as Sm-doped and undoped borosilicate glass. As the  $ZrB_2$  grains oxidize and expand, the glass is pushed up to the surface. However, with a higher concentration of glass on the surface, it takes more time to evaporate completely. Figure 5.2e shows a lighter colored glass pool compared to Figure 5.2f. This suggests there is more Sm incorporated into the glass as a lighter back scattered electron image indicates heavier elements. The cause for a higher Si containing glass in Figure 5.2f will be explained later in this section.

The cross-sections in Figure 5.5 reveal D1R1 and D2R1 have similar oxide scales with thicknesses of  $\sim 200\mu\text{m}$ . It is believed despite the exposed surface area, the formation of the extra glass at the surface helps protect the sample from further oxidation. The replenishment of glass in D1R1 during ablation and the penetration depth of the oxygen created by evaporation of the glassy phase thickens the oxide scale (as described in section 5.2.2), explaining the similarity to D2R1. These results suggest there may be a threshold of acceptable porosity.

Studies done by Li et. al.<sup>20,21,56</sup> on C-C/ZrC and ZBS/C-C/ZrC ablated above  $2000^\circ\text{C}$  in an oxy-acetylene rig have shown that samples with lower porosity result in better ablation

performance resulting from a denser oxide scale that is formed. Although a higher oxide density for denser samples was not distinguished in this work, the lower porosity samples obtained a thinner oxide scale post ablation. This indicates higher densities do result in better ablation performance, as suggested by Li et. al.<sup>56</sup>

In D3R1 the amount of  $ZrO_2$  found in the sample increases, as seen in Figure 5.3c and mentioned previously. Again, the exposed surface from the lower density increases the oxygen penetration depth. It is believed that with increased open porosity, the glass transportation of the Si to the surface was faster than D1R1 and D1R2, leaving little time for the Sm to incorporate as much into the glassy phase. This explains the lack of Sm in the glass pools in D3R1, as well as why there is no Sm-depletion region with increasing open porosity. This also explains the high concentrations of trapped Sm in the cross-section, as seen in Figure 5.5. With the Sm trapped beneath the surface, little Sm is left for the formation of SZO, as seen in the XRD of D3R1 in Figure 5.3c. With increased time the Sm may have combined with the  $ZrO_2$  beneath the surface and formed more SZO.

#### **5.2.4 Post Laser Heated Billets of Different Surface Roughnesses and Porosity Result in Same Microstructure**

The post ablated surfaces for all the samples show there is little difference in microstructure, as seen in Figure 5.6, except for D3R1. D3R1 contains smaller oxide grains and large linear pores like cracks. This is likely due to the starting porosity; however, EDS results are consistent with all other samples. Similarity in microstructure is believed to be due to the formation and bursting of convectional cells, as mentioned in Section 5.2.1. Crystalline structures of mainly Zr and O can be seen surrounded by a Sm, O, and Si glassy phase. Atomic% of the different elements in the two distinct phase regions can be seen in Figure 5.9. XRD analysis of the different conditions at powers of 700W, 800W, and 900W all show a main phase of m- $ZrO_2$  with minuscule

peaks of  $\text{Sm}_2\text{O}_3$  and  $c_1\text{-Sm}_{0.2}\text{Zr}_{0.8}\text{O}_{1.9}$  present in the XRD scan seen in Figure 5.7 and Table 5.2. In the  $\text{Sm}_2\text{O}_3\text{-ZrO}_2$  phase diagram, it can be seen the reason we are not forming  $c_1\text{-Sm}_{0.2}\text{Zr}_{0.8}\text{O}_{1.9}$  is because there is simply not enough Sm in the Zr regions on the radiance side of the sample. The amount of Sm necessary to form SZO is  $\sim 8$  mol%, as seen in Figure 5.13 while we only have 3 mol% in the crystalline phase.<sup>53</sup>

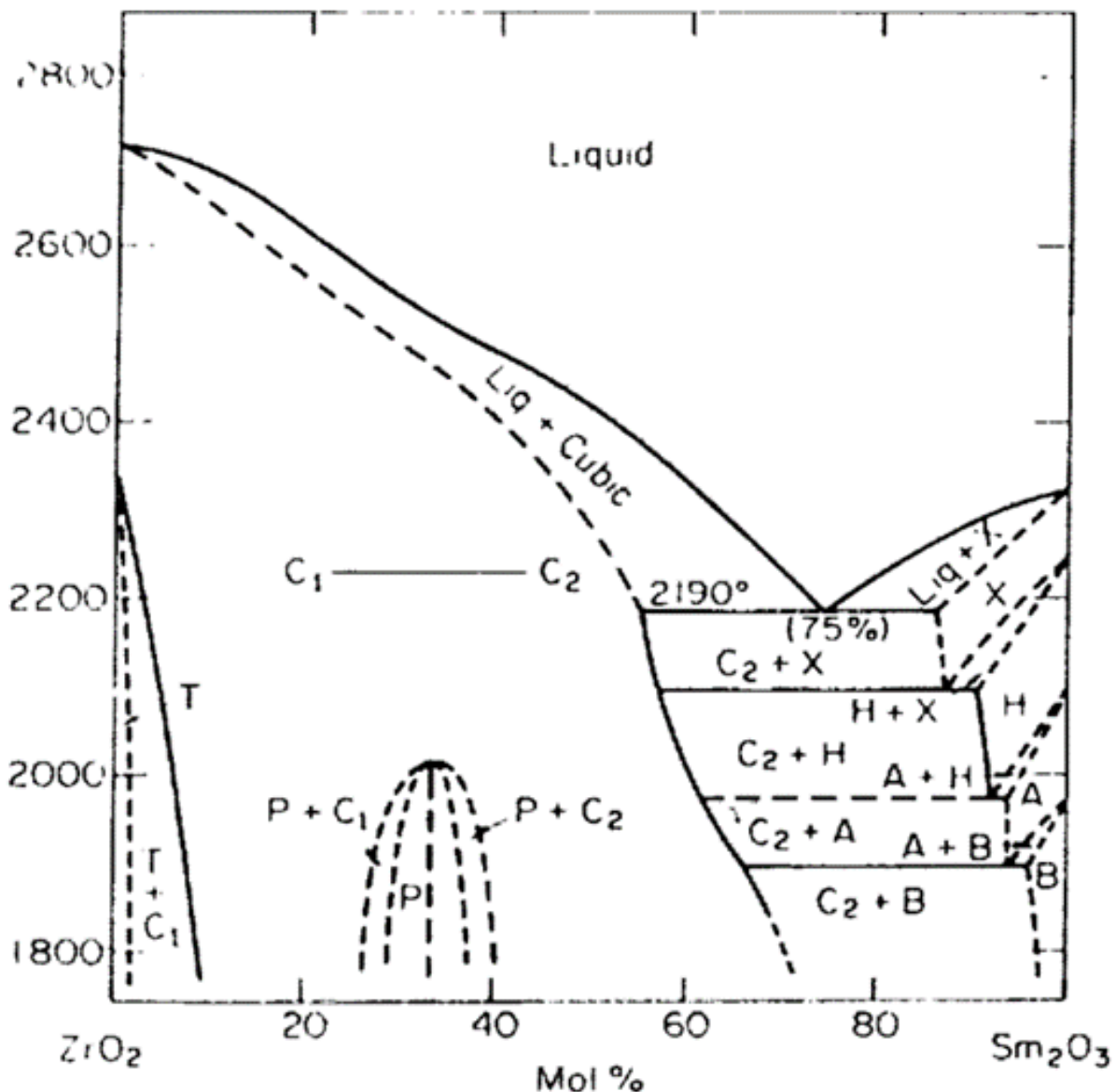


Figure 5.13  $\text{ZrO}_2\text{-Sm}_2\text{O}_3$  phase diagram.<sup>53</sup>  $c_1\text{-Sm}_{0.2}\text{Zr}_{0.3}\text{O}_{1.9}$  is denoted by C1 in phase diagram. Temperature on horizontal axis is in  $^\circ\text{C}$ .

Although a small amount of  $c_1\text{-Sm}_{0.2}\text{Zr}_{0.8}\text{O}_{1.9}$  is formed, as seen in Figure 5.7, there is not enough to dope most of the  $m\text{-ZrO}_2$ . As mentioned in Chapter 4, Sm incorporates into the Si and is pushed up through the expansion of oxidizing  $\text{ZrB}_2$ . As the Si is evaporated off, the Sm is left behind, leaving a higher concentration on the surface. As there should be enough Sm on the surface to form SZO, the non-laser heated sides conditions were not like the oxyacetylene ablation experiments performed on Sm-doped ZBS.<sup>29-31</sup> In these experiments, there was a higher oxygen partial pressure compared to what is normally in the air.

Laser heating of the back side of the billet without the addition of extra oxygen also likely caused the formation of  $m\text{-ZrO}_2$  and not  $c_1\text{-Sm}_{0.2}\text{Zr}_{0.8}\text{O}_{1.9}$ . In studies done on  $\text{ZrB}_2/\text{SiC}$  at lower oxygen partial pressures, it was found that as  $\text{PO}_2$  decreased, the active oxidation of SiC in the sample increased, while the active oxidation of  $\text{ZrB}_2$  decreased.<sup>57,58</sup> With  $\text{ZrB}_2$  not oxidizing as quickly, the Sm likely stayed in the Si phase, as this was the first to oxidize. Before the  $\text{ZrB}_2$  had a chance to oxidize completely to  $\text{ZrO}_2$ , the Si evaporated and left Sm in the glassy phase, as seen in Figure 5.10. It is possible that if the sample would have been heated longer, there may have been more SZO.

Although a large amount Si of was not seen on the surface, this was likely due to two reasons: firstly, that the amount of SiC in the sample to start was low. EDS indicated only 4 atomic% Si was present on the surface. Secondly, as mentioned previously, the sample was heated on the opposite side of what was investigated. It is well known that during oxidation a  $\text{SiO}_2$  scale and depletion layer forms due to the oxidation of  $\text{ZrB}_2$ .<sup>19,38,48,49</sup> The samples investigated were again hit with a laser on the opposite side and formed an oxide that was melted through most of the sample thickness, as seen in Figure 5.9. It is likely that most of the Si was depleted to the other

side first due to the increase in temperature compared to what the investigated side experienced. Despite the likely consumption of Si in the sample on the opposite side, the investigated billets also reached temperatures exceeding 1800°C, most of which exceeded 2000°C. Residual white matter from condensation of the evaporated products was collected from the graphite holder post laser ablation and contained mainly B<sub>2</sub>O<sub>3</sub> as well as SiO<sub>2</sub> and graphite (likely from the graphite holder). It is likely most of the silica that was present on the surface evaporated off.

### 5.2.5 Spectral Emittance of Sm-ZBS with Different Surface Roughness and Porosities

Emittance as a function of wavelength also showed no significant difference between average surface roughness and porosity, as seen in Figure 5.10, at temperatures of 2100°C. However, at 1600°C both D1R3 and D3R1 showed slightly lower emittance values. It is unclear why this is the case, but it may be due to the formation of the oxide structure. A study done by Eldridge et. al.<sup>60</sup> showed, for thick yttrium stabilized zirconia in the 1.5-4μm (1500-4000nm) range, at 1350°C the transmittance was essentially negligible, and the sample showed a reflectance of ~0.7. Assuming emittance is equal to the difference between 1 and reflectance, the emittance value would be ~0.3. Liebert<sup>59</sup> also found that the emittance of ZrO<sub>2</sub> between 1μm-4μm range emittance to be between 0.3-0.4, which matches the data presented in Figures 5.10 and 5.12.

With Sm added to the system, it was expected that the Sm would play a role in increasing the emittance.<sup>11,31</sup> However, Sm appeared to make no difference in this study. Studies done by Advoshenko and Strachen<sup>11</sup> show that Sm<sup>+3</sup> ions in Sm<sub>2</sub>O<sub>3</sub>, and potentially with the addition of Sm<sup>+3</sup> to ZrO<sub>2</sub>, would have high emittances due to the localized f-shell electrons, as well as forming oxygen vacancies in ZrO<sub>2</sub>. However, in our studies, the addition of Sm to the system did not result in increased emittances compared to m-ZrO<sub>2</sub>. This is believed to be because the Sm in the wavelength and temperature range investigated, also has a low emittance (~0.1-0.2).<sup>11</sup>

Spectral emittance as a function of wavelength also reveals little difference as a function of time. In Figure 5.11, in 10s intervals up to 40s, the emittance decreases slightly. This is likely due to a higher Sm-doped silicate glass on the surface. As seen in studies performed by Advoshenko and Strachen<sup>11</sup>, both Sm and Si at these temperature and wavelength ranges exhibit lower emittances. After 40s, the emittance begins to increase again, almost back to the original emittance at (10s). The likely explanation for this is that ZrO<sub>2</sub> is the dominant phase on the surface again.

Spectral emittance testing resulted in almost identical emittances for all samples tested. This was expected, due to the formation of slightly Sm doped m-ZrO<sub>2</sub> for all the samples, as well as similar microstructures. As temperature is increased, the emittance remains relatively unchanged, as seen in Figure 5.12. It can also be seen that both the porosity and surface roughness have little to no effect on the emittance as a function of temperature, as seen in Figure 5.12a and 5.12b. In both graphs, the average emittance was ~0.35 across a temperature range of 1200°C-2200°C. The wavelength was held constant at 3000nm. These results were also consistent for wavelengths held at 1997nm and 4000nm; however, the average emittance at a wavelength of 1997nm increased to ~0.4 from 1600°C to 2200°C. A study done by Liebert<sup>59</sup> on zirconia on the emittance as a function of temperature; it was found that, in the temperature range of 700K-2700K (427°C-2427°C), the total hemispherical emittance decreased as temperature increased. This was also the same the spectral emittance in the range of 1.5µm-4µm for YSZ.<sup>60</sup> However, this was the opposite of what was found by Chekhovskoi et. al.<sup>61</sup> on fused ZrO<sub>2</sub> in the spectral range of 530-650nm. At these wavelengths the average emittance started at 0.3 at 1400°C and increased to 0.6 at 1800°C.

### 5.3 Conclusion

Billets with varying porosities and average surface roughness were sintered and tested in an oxyacetylene torch ablation rig. It was found that increased average surface roughness and open

porosity resulted in higher ablation temperatures. Except for an open porosity of 24%, this resulted in the almost complete formation of  $c_1\text{-Sm}_{0.2}\text{Zr}_{0.8}\text{O}_{1.9}$ . It was also found that starting surface roughness has little effect on topographical microstructure due to the high temperatures and glassy phase covering the surface from oxidation. Despite identical surface features, increasing the average surface roughness resulted in larger oxide scales. This was also the case for increased porosity, due to the increase in exposed surface area, also explaining the glass pools evident in lower density samples.

Billets also were tested for emittance using a laser set-up at the Air Force Research Laboratory in Dayton, OH. Due to how the billets were tested,  $m\text{-ZrO}_2$  was the main phase formed, which resulted in an average emittance of 0.35. All samples resulted in a similar microstructure, which resulted in surface roughness and porosity having no effect on the emittance. Small changes in the emittance as a function of time can be seen, likely due to the formation and evaporation of the Sm-doped silicate glass. It is in the authors opinion that, if an oxide scale was first formed and then had varied surface roughness and porosity, there may have been some differences seen in the emittance data.

## 6. FABRICATION AND ABLATION TESTING OF CUBIC-SAMARIUM(0.2) ZIRCONIUM(0.8) OXYGEN(1.9)

### 6.1 Prior Studies on $c_1\text{-Sm}_{0.2}\text{Zr}_{0.8}\text{O}_{1.9}$

Few studies have been performed on  $c_1\text{-Sm}_{0.2}\text{Zr}_{0.8}\text{O}_{1.9}$  (SZO).<sup>30, 31, 63, 64</sup> Applications for the material have been considered for thermal barrier coatings as well as solid oxide fuel cells. Tan et. al.<sup>30,31</sup> created SZO as a post-ablation oxidation scale like the studies described in this thesis. With the high melting temperature, low chemical reactivity, and potential for high emittance, they concluded that SZO would make an excellent thermal barrier coating. Liu et. al.<sup>63</sup> studied the thermal expansion and thermal conductivity of Sm-doped  $\text{ZrO}_2$  ceramics up to 1673°C in a furnace. The powders were processed by chemical reaction and calcination, then spark plasma sintering to full density. They found that increasing Sm concentration increased the coefficient of thermal expansion (CTE), but decreased the thermal conductivity. They also found it was hard to tell via XRD alone which crystal structure was formed over the other, except for a slight shift as seen in Figure 6.1, hinting another method other than XRD is needed for analysis.<sup>63</sup>

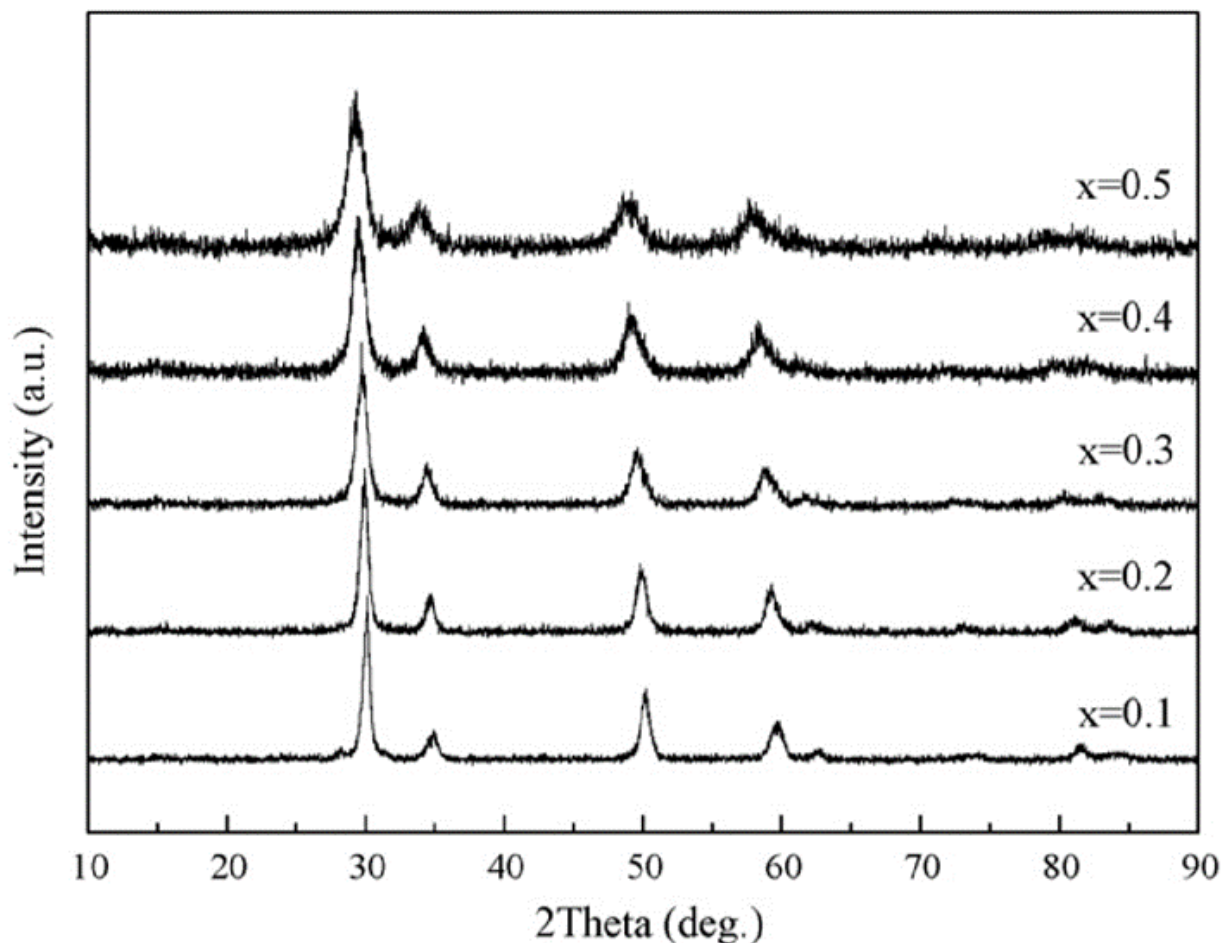


**Figure 6.1** XRD analysis of  $\text{Sm}_x\text{Zr}_{1-x}\text{O}_{2x-1}$ , where  $x$  is the samarium concentration of  $x=1$  to  $x=5$ .<sup>63</sup>

Another study performed by Fenech et. al.<sup>64</sup> investigated CTE and heat capacity of Sm-doped  $\text{ZrO}_2$  (including SZO) processed via a sol-gel and then spark plasma sintered. They found a similar CTE as Liu. et. al.<sup>63</sup> of a value of  $11.3 \times 10^{-6}/^\circ\text{C}$ ; however, they found the opposite of Liu, in that increasing Sm concentration decreased the CTE, showing some discrepancy in the literature. What makes this study unique is that to the authors knowledge, no studies have been performed on the fabrication via the pressureless solid-state sintering technique described in Chapter 3. It is also the authors knowledge that no studies have been performed on the ablation resistance of pure SZO.

## 6.2 Results

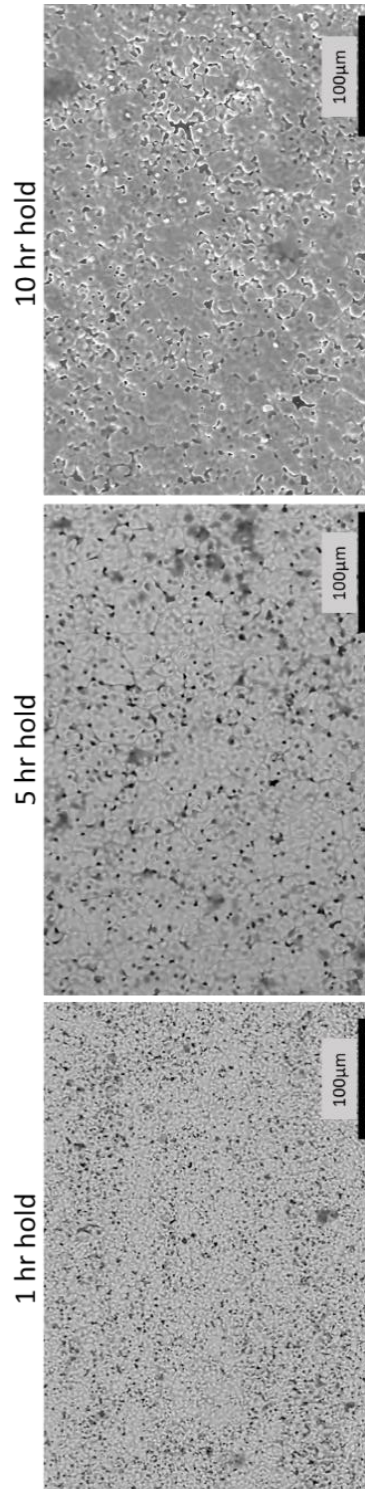
### 6.2.1 Post-Sintered Phases

Table 6.1 shows the several sintering approaches used to attempt to fabricate  $\text{c}_1\text{-Sm}_{0.2}\text{Zr}_{0.8}\text{O}_{1.9}$ . Temperatures 1600°C and lower resulted in the incomplete formation of SZO. At temperatures reaching 1700°C with longer ramp rates, a minimum hold time of 2 hours is required. Incomplete formation of Sample 10 in Table 6.1 is believed to be due to inadequate mixing of the powder, failing adequate hold temperature and time. Sample sizes were 24.5mm x 24.5mm x 8mm.

**Table 6.1 Table showing ramp rate, hold temperature, hold time, and phases present after sintering for powders heated in a furnace in air.**

Sample	Ramp rate	Hold Temperature	Hold Time	Phase(s) Present
1	10°C/min	1700°C	1 hr	SZO, ZrO <sub>2</sub>
2	10°C/min	1700°C	2hr	SZO
3	10°C/min	1700°C	3 hr	SZO
4	10°C/min	1700°C	4 hr	SZO
5	10°C/min	1700°C	5 hr	SZO
6	10°C/min	1700°C	10 hr	SZO
7	5°C/min	1700°C	1 hr	SZO
8	5°C/min	1700°C	2 hr	SZO
9	5°C/min	1700°C	3 hr	SZO
10	10°C/min-nano powder	1700°C	5 hr	SZO, ZrO <sub>2</sub>
11	10°C/min	1600°C	1 hr	SZO, ZrO <sub>2</sub>
12	10°C/min	1500°C	1 hr	SZO, ZrO <sub>2</sub> , Sm <sub>2</sub> O <sub>3</sub>
13	10°C/min	1400°C	1 hr	ZrO <sub>2</sub> , Sm <sub>2</sub> O <sub>3</sub>

Differences in hold time reveal slight differences in microstructure. It can be seen in Figure 6.2 that longer hold times result in larger grains. This was expected, as longer hold times at high temperatures results in grain growth.<sup>62</sup>



**Figure 6.2 SEM-BSE images of samples with different hold times at 1700°C. Dark cloudy regions are debris from the furnace and not part of the actual sample.**

### 6.2.2 Pre-Ablation Results

Sample 5 in Table 6.1, with the conditions of a 5 hour hold at 1700°C, was chosen for ablation analysis based on large grain size and median hold time. The density of the billet was determined to be 81% using Archimedes' method, based on a density of 6.67 g/cm<sup>3</sup>. Figure 6.3a shows the pre-ablated billet to have a yellow hue to it. A chip on the sample was due to mishandling prior to ablation.

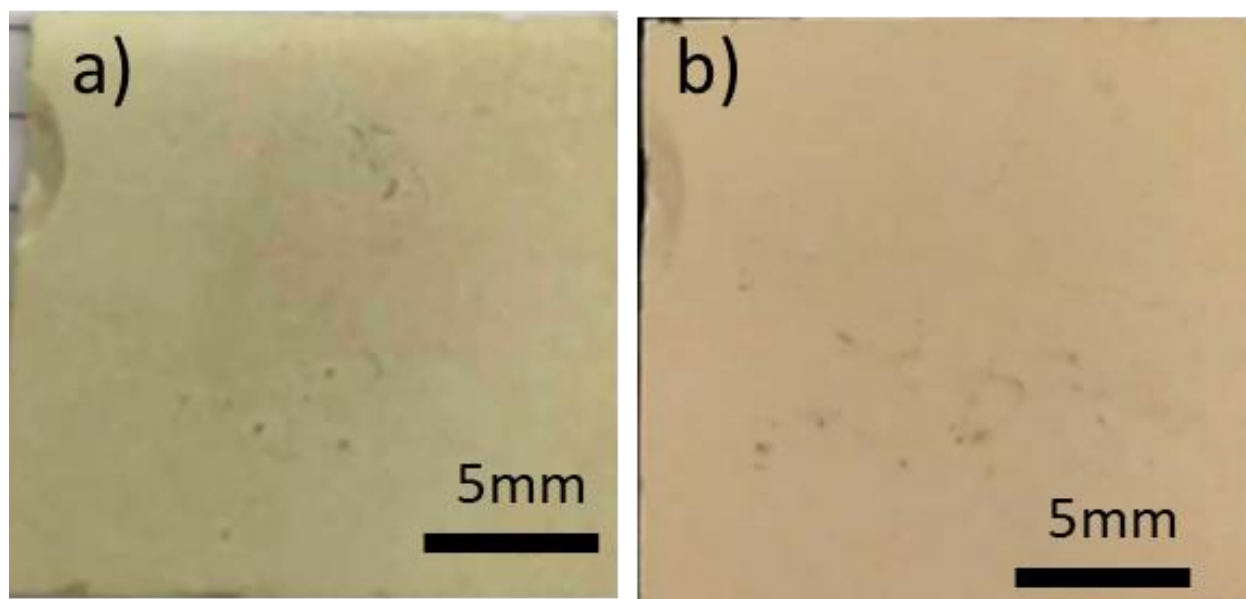


**Figure 6.3 Optical images showing a) pre-ablation and b) post-ablation SZO billets. Differences in coloration are due to camera lighting**

XRD results reveal the only crystalline phase present is SZO, as seen in Figure 6.4a and Table 6.1. However, cross-sectional EDS reveals pockets of ZrO<sub>2</sub>, likely due to agglomeration of powders during mixing. This can be seen in Figure 6.5, where the small-grained pockets are the ZrO<sub>2</sub>, as indicated by the high Zr concentration and lack of Sm in the area. Cracks and large pores can also be seen in the cross-section of the sample, likely due to the density of the sample and the cutting procedure used on the surface grinder.

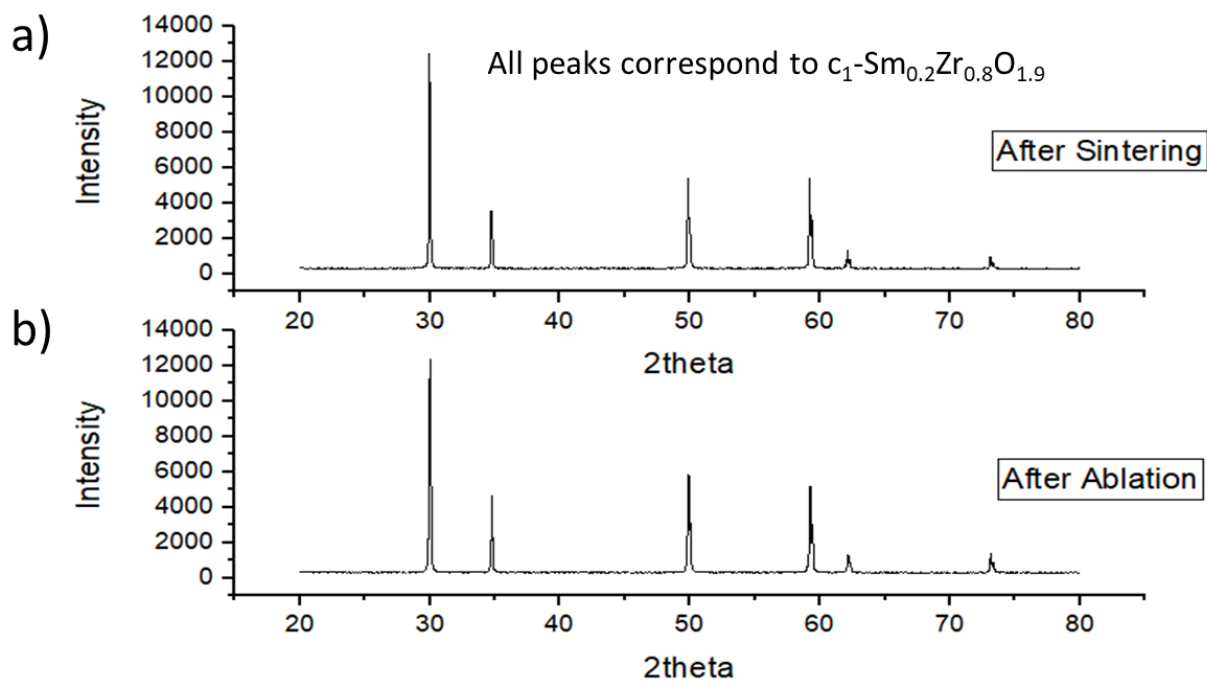


Figure 6.5 XRD patterns of the billet a) pre-ablated and b) post ablated. All peaks correspond to SZO.

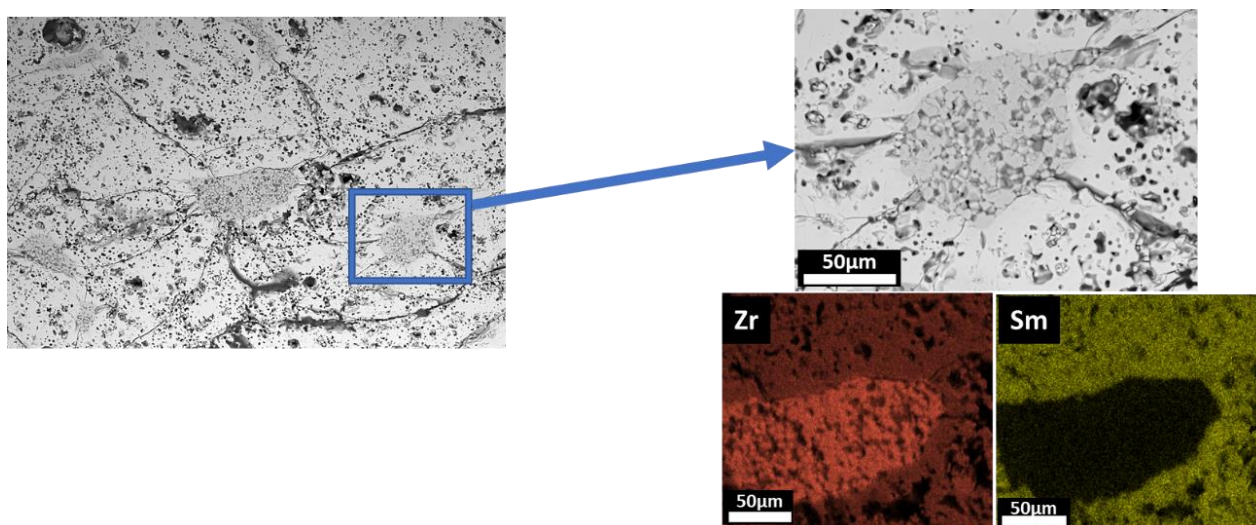
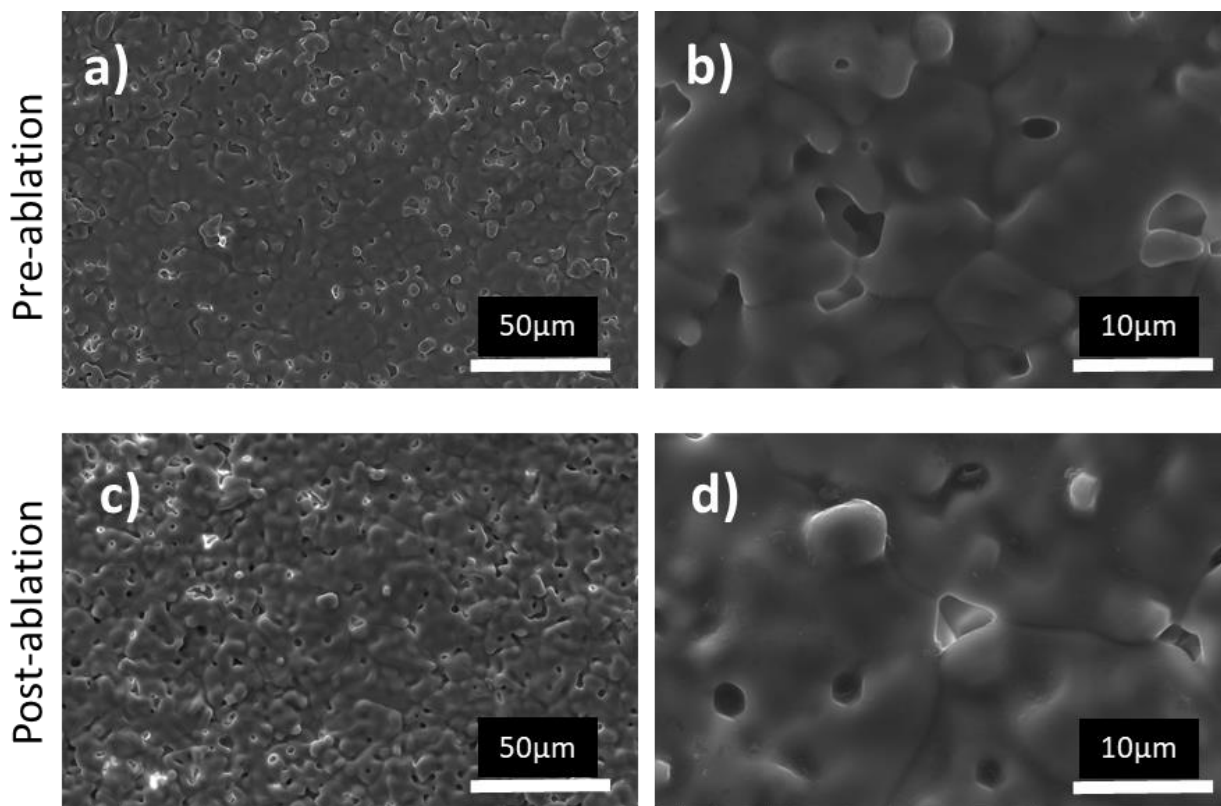


Figure 6.4 SEM-BSE cross-sectional images of the billet. EDS scans reveal small grain pockets are rich in Zr and lacking Sm.

Topographical SEM images reveal a uniform phase and microstructure despite what was seen in the cross-section. EDS analysis reveals a uniform phase with 9 at% Sm, 21 at% Zr, and 70 at% O. Figures 6.6a-b show a large grained microstructure with a significant amount of porosity, as expected by the low density.



**Figure 6.6 SEM images showing a) pre-ablation microstructure, b) higher magnification of a), c) post-ablation microstructure, and d) higher magnification of c).**

### 6.2.3 Post-Ablation Results and Discussion

Ablation of the SZO billet resulted in no changes as seen in Figure 6.3b. The sample was ablated for 600s and reached a stable front-face temperature (side exposed to the flame) of 2209°C after 60s. The back-face temperature reached a maximum of ~600°C, indicating the material has a low thermal conductivity, as concluded by Liu et. al.<sup>63</sup> However, it should be noted that the

porosity likely played a role in the low back-face temperature as well. The sample during ablation also showed no signs of melting or physical change visually.

XRD results reveal no change in the phases present post-ablation, as depicted in Figure 6.5b. This was expected, as the material was already in an oxide form. This was also confirmed via EDS, where the concentrations of Sm, Zr, and O remained unchanged. Topographical SEM images in Figure 6c-d show no change in microstructure either. This was also expected, as the melting temperature of the material is  $\sim 2600^{\circ}\text{C}$  and the maximum temperature reached was  $\sim 2200^{\circ}\text{C}$ . Cross-sectional results, in Figure 6.7, show areas that previously contained a high concentration of Zr (as well as a different microstructure), disappeared and showed a uniform porous microstructure with cracks similar to those seen prior to ablation. As the temperature reached  $\sim 2200^{\circ}\text{C}$  and the billet was heated for 600s, it was expected that the sample fully converted to SZO.

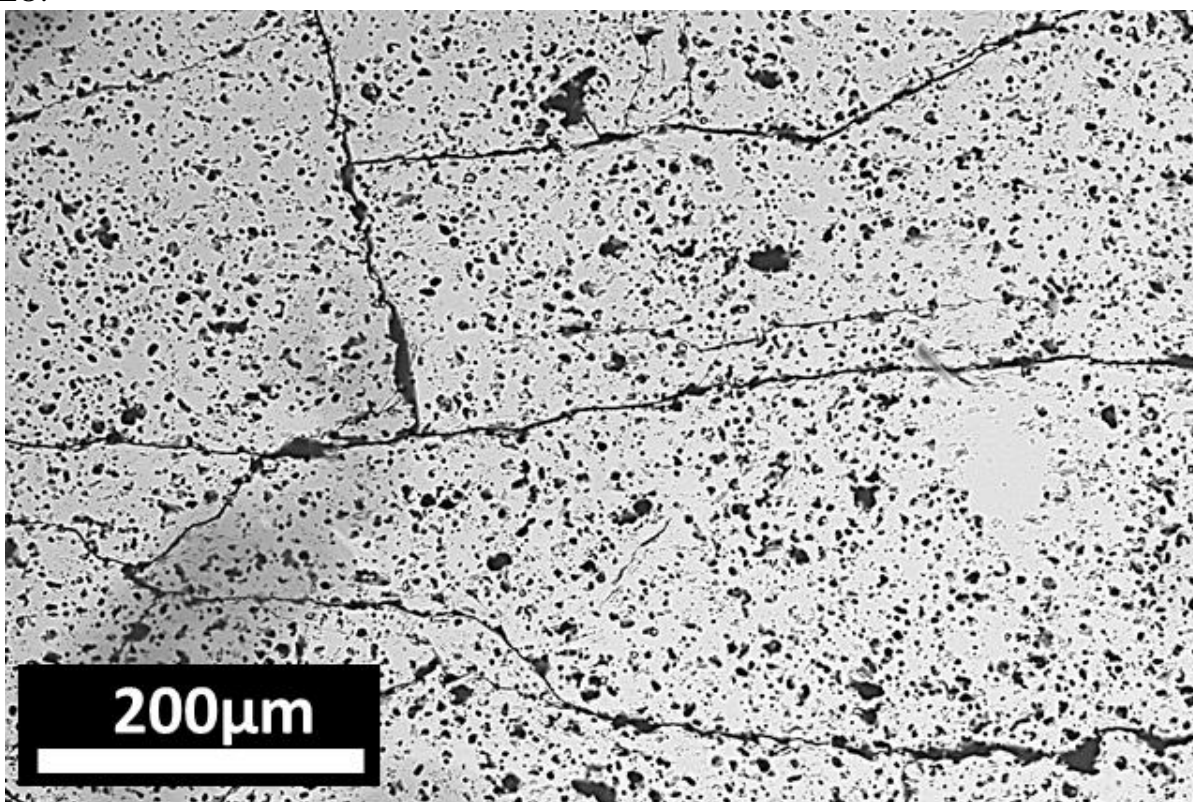


**Figure 6.7** EM-BSE image of the cross-section of the post-ablated SZO billet

LTE experiments to extract the CTE of the material were also performed post-ablation, as seen in Figure 6.8. When compared with the literature, CTE measurements did not match what was reported in the previously mentioned studies, as the results obtained were almost half ( $6.9 \times 10^{-6}/^{\circ}\text{C}$ ). It should be noted that the CTE was the average over the temperature range of  $200^{\circ}\text{C}$ - $1600^{\circ}\text{C}$ . However, the CTE reported by Tan<sup>32</sup> does match what was obtained in this study. It is unclear why different results were obtained by Liu et. al.<sup>63</sup> and Fenech et. al.<sup>64</sup>; however, their processing methods were different as they used spark plasma sintering. One explanation may be that there was Sm ion migration during the spark plasma sintering process, resulting in the different CTE results. They also came up with different conclusions as to the amount of Sm concentration in the system. This material is not well studied or understood, therefore more studies should be done to confirm the actual CTE measurements.

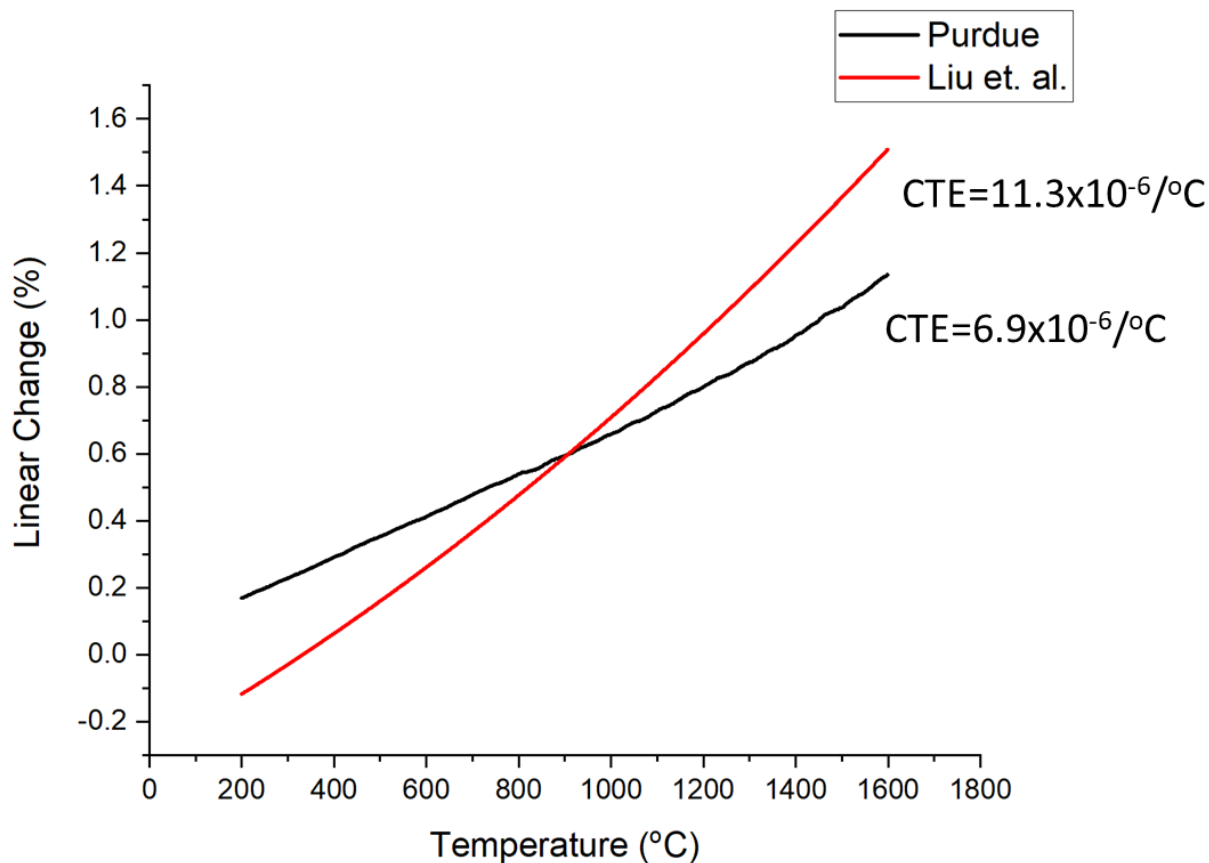


**Figure 6.8 CTE graph of the samples conducted at Purdue compared to those performed by Liu. et. al.<sup>63</sup>**

Post-ablation, the billet also became friable. This is believed to be due to two reasons. The first reason is believed to be due to the starting microstructure. As mentioned previously, cracks and a high quantity of pores were prevalent in the sample. When under compression, this likely caused the samples' cracks to prorogate and cause the fracture. The second reason is believed to be due to how the sample was clamped in the ablation rig. Figure 6.9 depicts how the sample was clamped and heated in the ablation rig. Wear on the graphite plates that were used to clamp the billet in front of the flame caused a higher pressure on the front face of the sample. Coupled with the differences in temperature (where the front face reached ~2200°C and the back face reached ~600°C), the sample likely became more friable.

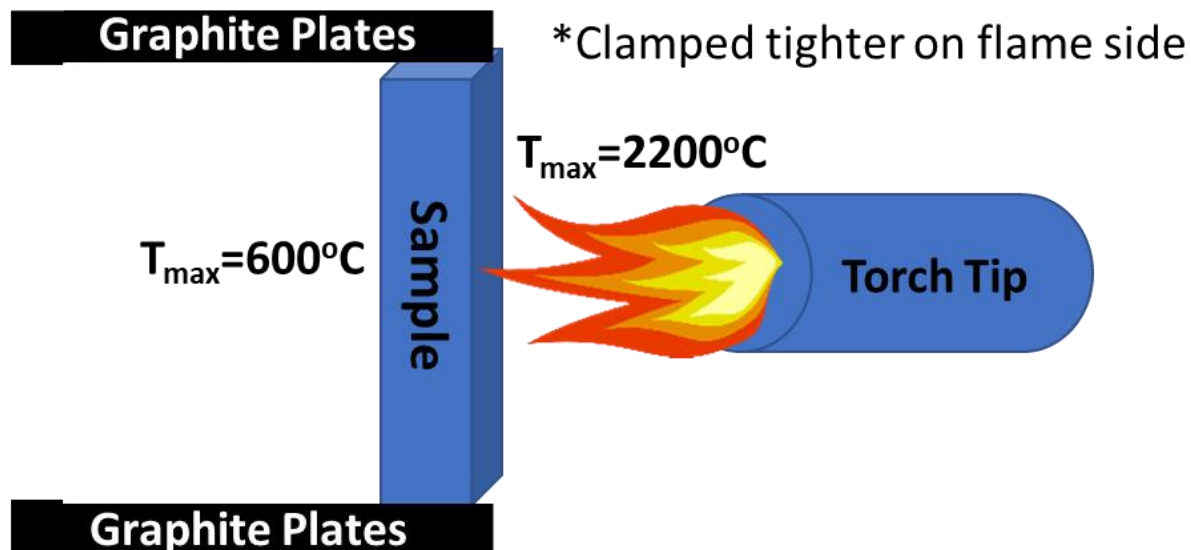


**Figure 6.9** Depiction of how the sample was clamped and heated in the ablation rig. Due to wear of the graphite plates, sample was clamped tighter on the front of the sample (torch side).

### 6.3 Conclusion

In this study,  $c_1\text{-Sm}_{0.2}\text{Zr}_{0.8}\text{O}_{1.9}$  was fabricated using pressureless solid-state sintering in a furnace in air. The minimum temperature requirement for fully converting the  $\text{Sm}_2\text{O}_3$  and  $\text{ZrO}_2$  starting powders to  $c_1\text{-Sm}_{0.2}\text{Zr}_{0.8}\text{O}_{1.9}$  was  $1700^{\circ}\text{C}$ . Maximum temperature hold-time and ramp rate also played a role in fully converting the powder to  $c_1\text{-Sm}_{0.2}\text{Zr}_{0.8}\text{O}_{1.9}$ , as did the grain size. Porosity and cracks were prevalent in the sample post-sintering indicating the processing technique used needs to be modified. Despite flaws in the microstructure, the billet created out of  $c_1\text{-Sm}_{0.2}\text{Zr}_{0.8}\text{O}_{1.9}$  showed promising ablation results. The billet successfully reached a temperature of  $\sim 2200^{\circ}\text{C}$  and showed no signs of change in phase or microstructure after 600s of ablation, except for the full conversion of the unmixed regions in the cross-section, which were fully converted to  $c_1\text{-Sm}_{0.2}\text{Zr}_{0.8}\text{O}_{1.9}$ . Coefficient of thermal expansion results showed similar values to those recorded by Tan et. al.<sup>31</sup>, smaller than those recorded by other studies.<sup>63,64</sup> It is unclear why the results vary, but it is clear more studies on this material are needed. The billet, post-ablation also became friable.

This was likely due both to the starting cracks and porosity of the sample and to how the sample was clamped into the ablation rig. As mentioned previously, more studies on this material are needed, but it appears that, with improvement in processing,  $c_1\text{-Sm}_{0.2}\text{Zr}_{0.8}\text{O}_{1.9}$  has the potential to be an excellent thermal barrier coating.

## 7. SUMMARY AND FUTURE WORK

### 7.1 Summary of Studies Presented

Three main questions remained after Tan<sup>32</sup> had found that samarium dopant ( $\text{Sm}^{+3}$ ) has the potential to increase the emittance and improve the ablation performance. First was how does the  $\text{c}_1\text{-Sm}_{0.2}\text{Zr}_{0.8}\text{O}_{1.9}$  (SZO) oxide scale form, second was how the microstructure effects the emittance and ablation performance of the material, and third was could the SZO phase be used as the starting material for thermal barrier coatings in place of Sm-doped  $\text{ZrB}_2/\text{SiC}$  (ZBS).

Chapter 4 investigated how the oxide scale formed for Sm-doped ZBS. It was found that the microstructure formed through the development and bursting of convectional cells. From the formation of the convectional cells, a Sm-depletion region formed from the combination of Sm with the Si. The Sm then glass-transport with the Si to the surface allowing for the concentration to be high enough for SZO to form as the starting Sm concentration was not enough. It was also found first oxides to form are  $\text{Sm}_2\text{O}_3$  and  $m\text{-ZrO}_2$  which then combine to form SZO.

Chapter 5 explored the effect of surface roughness and porosity on the ablation and emittance performance. During ablation in the oxy-acetylene ablation rig, it was found that rougher and more porous surfaces result in higher surface temperatures during ablation. This is likely due to the increased surface area for absorption to occur. The starting surface roughness was also found to not affect the resulting topographical microstructure. This is believed to be due to again the formation and bursting of convectional cells as described in Chapter 4. However, an increase in surface roughness increases the Sm-depletion region likely due to the increase in surface temperature. Despite an increase in surface temperature with increase porosity, it was found that higher porosity did not form a Sm-depletion region. This was likely due to the lack of Sm

incorporating with the Si and the starting open porosity. The starting open porosity was also believed to cause the glass pools that formed on the surface of more porous samples.

Despite differences found during ablation testing, emittance testing revealed dissimilar results. Despite reaching temperatures exceeding 2000°C for testing the emittance, SZO was not the main crystalline phase that formed. The main crystalline phase that did form was m-ZrO<sub>2</sub> which was likely due to the lower PO<sub>2</sub> compared to an oxyacetylene ablation rig. This likely caused the Sm to stay in the Si phase which evaporated quickly along with the lower active oxidation of ZrB<sub>2</sub> to form ZrO<sub>2</sub>. As concluded in the ablation part of the chapter, the topographical microstructure remained similar negating any emittance differences that may have been expected. It was found that porosity and surface roughness have little to no effect on the emittance of Sm-ZBS using this test method. With the main phase being m-ZrO<sub>2</sub>, the emittance results emulated what the emittance of ZrO<sub>2</sub> would be at ultra-high temperatures in the wavelength range investigated. Slight differences in the emittance as a function of temperature were seen as the emittance lowered up to 40s, then increased back to the original emittance values. This was likely due to the Sm-doped silicate glass covering the surface then evaporating off to the main phase being ZrO<sub>2</sub>. As Sm<sub>2</sub>O<sub>3</sub> and SiO<sub>2</sub> have lower emittances than ZrO<sub>2</sub> at the wavelengths investigated, it is likely this caused the lowering of the emittance values.<sup>11</sup>

Chapter 6 investigated the fabrication and ablation performance of SZO without the addition of ZrB<sub>2</sub> and SiC in the system. As this material is not well understood, it was deemed important to investigate. It was found that a minimum temperature of 1700°C was needed to fully form SZO via pressureless sintering in a furnace in air. Sintering hold time at the maximum temperature was found to affect the grain size, however porosity and cracks remained prevalent in all samples. Ablation in an oxygen rich environment for 600s at ~2200°C revealed no change in phase or

microstructure post-ablation heating. The back-face temperature of the sample also remained relatively cool compared to the front-face temperature indicating it is an insulator. However, it should be noted porosity likely played a role as well. However, the sample became friable post ablation which was likely due to starting microstructure and how the sample was clamped in the ablation rig. Coefficients of thermal expansion tests were conducted and compared with literature which resulted in conflicting results.

## 7.2 Suggestions for Future Work

It should be noted that although the sintering of the chemically doped powders worked for the studies above, the samarium compound,  $\text{SmB}_2\text{C}_2$ , that forms is reactive with water and if exposed will degrade over time. It is suggested a different mechanism to sinter the chemically doped powders be studied.

Based on the results in Chapter 5, it is recommended that oxidized samples of SZO with differing surface roughness and porosity be investigated for emittance effects. As the desired oxide scale was not obtained in this work for emittance testing, it is still unknown what the emittance of SZO is or how surface roughness and porosity truly effect the emittance at ultra-high temperatures. Patterned surfaces of the SZO oxide are also recommended to be looked at. Modeling results based on  $\text{ZrB}_2$  with patterned surfaces of  $R_a$  values in the wavelength range of interest were investigated and were found to potentially increase the emittance of the material at the wavelength of similar surface roughness.<sup>65</sup> Therefore, it is also suggested that emittance values in the lower wavelengths be investigated as well as this is where the visible region lies and where surface roughness may play a more important role. It is also recommended that (FT)IR, or absorbance, in the visible to infrared region be investigated as it could show insight on the emittance vs. wavelength plots

mentioned in Chapter 5 on if changes in structure are affecting the emittance of the samples at ultra-high temperatures.

Based on Chapter 6, it is also suggested that SZO be formed via plasma spraying. Tan et. al.<sup>31,32</sup> found plasma spraying Sm-doped ZBS results in a relatively dense microstructure as well as it is one of the main processes to make thermal barrier coatings. As SZO forms at 1700°C and above, it is believed that a mix of ZrO<sub>2</sub> and Sm<sub>2</sub>O<sub>3</sub> powder in the correct proportions could form using the plasma spray process. As plasma spraying melts the powder during spraying, it is believed that the two powders with the right spray conditions could form a dense microstructure of SZO.

It would also be worth investigating 3D printing of both SZO and the chemically doped powders. The Air Force Research Laboratory in Dayton, OH has a lab called LHIML that has the capabilities of testing leading edges in an environment that simulates a hypersonic situation. As the oxyacetylene ablation rig does not truly simulate re-entry conditions it would be interesting to see how true heat-flux and pressure simulations would affect the oxide and thermal barrier material.

## APPENDIX

It should be noted that prior work done to develop the spray-dried granules was performed to avoid degradation of the powders. Firstly, doping the powder during the spray-drying process was attempted. This does not work as the outlet temperature does not reach a hot enough temperature which results in a mud-like substance instead of granules. Secondly, changing the binder to guar-gum and gum arabic (as well as changing the concentrations) was attempted as these binders do not dissolve as readily in ethanol. It was found that these binders do not hold the powders together as strongly as PVA and should not be used. Thirdly, the solvent ethanol (for the doping step) was changed to isopropyl alcohol (99.99%) as isopropyl alcohol does not dissolve a significant amount of PVA. It should also be noted that any purity less than 99.9% isopropyl alcohol will not work and will result in broken powders as the water content will dissolve the PVA.

Lastly, it should be noted for future work to avoid forming  $\text{SmB}_2\text{C}_2$  during the sintering process. This compound is sensitive to water and will eventually degrade the sintered billets back to powder form. If this method must be used in the future avoiding polishing, sonicating, and cleaning in/with water.

## REFERENCES

- <sup>1</sup> J. Reuther, D. Kinney, S. Smith, D. Kontinos, P. Gage, and D. Saunders. A Reusable Space Vehicle Design Study Exploring Sharp Leading Edges. 35th AIAA Thermophysics Conference. (2001).
- <sup>2</sup> D. M. Van Wie, D. G. Drewry, D. E. King, and C. M. Hudson, "The Hypersonic Environment: Required Operating Conditions and Design Challenges," *Journal of Materials Science*, **39[19]** 5915-5924 (2004).
- <sup>3</sup> E. Wuchina, E. Opila, M. Opeka, W. Fahrenholtz, and I. Talmy, "UHTCs: Ultra-High Temperature Ceramic Materials for Extreme Environment Applications," *The Electrochemical Society Interface [Winter]* 30-36 (2007).
- <sup>4</sup> A. Mack, *Aerospace Science and Technology* **11** 386-95 (2007).
- <sup>5</sup> T. H. Squire and J. Marschall, "Material Property Requirements for Analysis and Design of UHTC Components in Hypersonic Applications," *Journal of the European Ceramic Society*, **30** 2239-2251 (2010).
- <sup>6</sup> W. R. McMahon and D. R. Wilder, "Hemispherical Spectral Emittance of Selected Rare Earth Oxides," *Journal of the American Ceramic Society*, **51[4]** 187-192 (1968).
- <sup>7</sup> D. Alfano, L. Scatteia, S. Cantoni, and M. Balat-Pichelin, "Emissivity and Catalytic Measurements on SiC-coated Carbon Fibre Reinforced Silicon Carbide Composite," *Journal of the European Ceramic Society*, **29** 2045-2051 (2009).
- <sup>8</sup> X. He, Y. Li, L. Wang, Y. Sun, S. Zhang, "High Emissivity Coatings for High Temperature Application: Progress and Prospect," *Thin Solid Films*, **517** 5120-2129 (2009).
- <sup>9</sup> G. E. Guzzoni, "High-Temperature Spectral Emittance of Oxides of Erbium, Samarium, Neodymium, and Ytterbium," *Applied Spectroscopy*, **26** 60-65 (1972).
- <sup>10</sup> R. Blaire, "Determination of Spectral Emissivity of Ceramic Bodies at Elevated Temperatures," *Journal of the American Ceramics Society*, **43.4** 197-203 (1960).
- <sup>11</sup> S. Avdoshenko, A. Strachan, "High-Temperature Emissivity of Silica, Zirconia and Samaria from ab Initio Simulations: Role of Defects and Disorder," *Modeling Simulations Material Science and Engineering*, **22** 1-15 (2014).
- <sup>12</sup> X. Zhao, X. D. He, Y. Sun, L. D. Wang, "Carbon Nanotubes Doped SiO<sub>2</sub>/SiO<sub>2</sub>-PbO Double Layer High Emissivity Coating," *Material Letters*, **65** 2592-2594 (2011).

- <sup>13</sup> M. Tului, G. Marino, and T. Valente, "Plasma Spray Deposition of Ultra High Temperature Ceramics," *Surface & Coatings Technology*, **201** 2103-2108 (2006).
- <sup>14</sup> F. Wang, L. Cheng, Q. Zhang, L. Zhang, "Applied Surface Science Effect of Surface Morphology and Densification on the Infrared Emissivity of C/SiC Composites," *Applied Surface Science*, **313** 670-676 (2014).
- <sup>15</sup> C. D. Wen, I. Mudawar, "Modeling the Effects of Surface Roughness on the Emissivity of Aluminum Alloys," *International Journal of Heat and Mass Transfer*, **49** 4279-4289 (2006).
- <sup>16</sup> L. Scatteia, D. Alfano, F. Monteverde, J. Sans, M. Balat-Pichelin, "Effect of the Machining Method on the Catalycity and Emissivity of ZrB<sub>2</sub> and ZrB<sub>2</sub>-HfB<sub>2</sub> Based Ceramics," *Journal of the American Ceramic Society*, **91** 1461-1468 (2008).
- <sup>17</sup> E. Sani, L. Mercatelli, J. Sans, L. Silvestroni, D. Sciti, "Porous and Dense Hafnium and Zirconium Ultra-High Temperature Ceramics for Solar Receivers," *Optical Materials*, **36** 163-168 (2013).
- <sup>18</sup> W. G. Fahrenholtz, "Thermodynamic Analysis of ZrB<sub>2</sub>-SiC Oxidation: Formation of a SiC-Depleted Region," *Journal of the American Ceramic Society*, **90** [1] 143-148 (2007).
- <sup>19</sup> S.N. Karlsdottir, J.W. Halloran, and A.N. Grundy, "Zirconia Transport by Liquid Convection During Oxidation of Zirconium Diboride-Silicon Carbide Composite," *Journal of the American Ceramic Society*, **91** [1] 272-277 (2008).
- <sup>20</sup> Z. Li, H. Li, S. Zhang, W. Li, and J. Wang, "Microstructures and Ablation Properties of C/C-SiC-ZrC Composites with Various Densities," *Ceramics International*, 8173-8181 (2013).
- <sup>21</sup> Z. Li, H. Li, S. Zhang, J. Wang, W. Li, F. Sun, "Effect of Reaction Melt Infiltration Temperature on Ablation Properties of 2D C/C-SiC-ZrC Composites," *Corrosion Science*, 12-19 (2012).
- <sup>22</sup> D.S.A. Mahmood, N. Glandut, A. A. Khan, and J.C. Labbe, "Surface Oxidation of Porous ZrB<sub>2</sub>-SiC Ceramic Composites by Continuous-Wave Ytterbium Fibre Laser," *Applied Surface Science*, **357** 1982-1990 (2015).
- <sup>23</sup> M. Holden, "Boundary Layer Transition and Surface Roughness Effect in Hypersonic Flow," *Annual Technical Report Advanced Technology Center Arvin Calspan*, 2-37 (1981).

- <sup>24</sup> S. Schneider, "Effect of Roughness on Hypersonic Boundary-Layer Transition," *Journal of Spacecraft and Rockets*, **45** [2] 193-209 (2008).
- <sup>25</sup> R. M. Grabow, and C. O. White, "Surface Roughness Effects on Nostip Ablation Characteristics," *AIAA Journal*, **13** [5] 605-609 (1975).
- <sup>26</sup> D. C. Reda, M. C. Wilder, D. W. Bogdanoff, and D. K. Prabhu, "Transition Experiments on Blunt Bodies with Distributed Roughness in Hypersonic Free Flight," *Journal of Spacecraft and Rockets*, **45** [2] 210-215 (2008).
- <sup>27</sup> N. Rostamy, D. J. Bergstrom, D. Sumner, and J. D. Bugg, "The Effect of Surface Roughness on the Turbulence Structure of a Plane Wall Jet," *Physics of Fluids*, **23** 1-10 (2011).
- <sup>28</sup> B. M. Wheaton, D. C. Berridge, T. D. Wolf, R. T. Stevens, and B. E. McGrath, "Boundary Layer Transition (BOLT) Flight Experimental Overview," *AIAA Aviation Forum*, 1-25 (2018).
- <sup>29</sup> W. Tan, C. A. Petorak, and R. W. Trice, "Rare-Earth Modified Zirconium Diboride High Emissivity Coatings for Hypersonic Applications," *Journal of the European Ceramic Society*, **5**[1] 1-11 (2014).
- <sup>30</sup> W. Tan, M. Adducci, and R. Trice, "Evaluation of Rare-Earth Modified ZrB<sub>2</sub>- SiC Ablation Resistance Using an Oxyacetylene Torch," *Journal of the American Ceramic Society*, **97**[8] 2639-2645 (2014).
- <sup>31</sup> W. Tan, M. Adducci, C. Petorak, A. E. Brenner, and R. W. Trice, "Effect of Rare-Earth Dopant (Sm) Concentration on Total Hemispherical Emissivity and Ablation Resistance of ZrB<sub>2</sub>/SiC Coatings," *Journal of the European Ceramic Society*, 1-9 (2016).
- <sup>32</sup> W. Tan, "Design of High Emissivity Coatings for Hypersonic Applications Using Plasma Spray," in *School of Materials Engineering Ph.D. Thesis, Purdue University, West Lafayette, IN* (2014).
- <sup>33</sup> ASTM F77-69, "Test Method for Apparent Density of Ceramics for Electron Device and Semiconductor Application," *ASTM International*, (1996).
- <sup>34</sup> ASTM E 285-08, "Standard Test Method for Oxyacetylene Ablation Testing of Thermal Insulation Materials." *ASTM International*, (2008).
- <sup>35</sup> A. Pena, "Evaluation of Rare-Earth Element Dopants (Sm and Er) Effect on the Ablation Resistance and Emittance Tailoring of ZrB<sub>2</sub>/SiC Sintered Billets," in *School of Materials Engineering Ph.D. Thesis, Purdue University, West Lafayette, IN* (2019).

- <sup>36</sup> P. Saunders, and D. R. White, "Physical Basis of Interpolation Equations for Radiation Thermometry," *Metrologia*, **40**[4] (2003).
- <sup>37</sup> T. Negano, and K. Kaneko, "Effect of Atmosphere on Weight Loss in Sintered Silicon Carbide During Heat Treatment," *Journal of the American Ceramic Society*, **83** [11] 2781-2787 (2000).
- <sup>38</sup> S. N. Karlsdottir, and J. W. Halloran, "Formation of Oxide Films on ZrB<sub>2</sub>-15vol% SiC Composites During Oxidation: Evolution with Time and Temperature," *Journal of the American Ceramic Society*, **92** [6] 1328-1332 (2009).
- <sup>39</sup> R. Karell, J. Kraxner, M. Chromcikova, "Properties of Selected Zirconia Containing Silicate Glasses," *Ceramics-Silikaty*, **50** [2] 78-82 (2006).
- <sup>40</sup> S. N. Karlsdottir, J. W. Halloran, and C. E. Henderson, "Convection Patterns in Liquid Oxide Films on ZrB<sub>2</sub>-SiC Composites Oxidized at High Temperature," *Journal of the American Ceramic Society*, **90** [9] 2863-2867 (2007).
- <sup>41</sup> M. B. Amar, and E. G. Poire, "Pushing a Non-Newtonian Fluid in a Hele-Shaw Cell: From Fingers to Needles," *Physics of Fluids*, **11** [7] 1757-1767 (1999).
- <sup>42</sup> H. S. Rabbani, D. Or, Y. Liu, C. Lai, N. B. Lu, S. S. Datta, H. A. Stone, and N. Shokri, "Suppressing Viscous Fingering in Structured Porous Media," *PNAS*, **19** 4833-4838 (2018).
- <sup>43</sup> R. Telle, F. Greffrath, and R. Prieler, "Direct Observation of the Liquid Miscibility Gap in the Zirconia-Silica System," *Journal of the European Ceramic Society*, **35** 3995-4004 (2015).
- <sup>44</sup> J. He, Y. Wang, L. Lou, and L. An, "Oxidation Behavior of ZrB<sub>2</sub>-SiC (Al/Y) Ceramics at 1700°C," *Journal of the European Ceramic Society*, **36** 3769-3774 (2016).
- <sup>45</sup> D. B. Epassaka, S. Ohshio, and H. Saitoh, "Morphological Instability of ZrO<sub>2</sub> Crystallites formed by CVD Technique Operated Under Atmospheric Pressure," *Journal of Material Science*, **38** 3239-3244 (2003).
- <sup>46</sup> A. E. Brenner, A. A. Peña, X. L. Phuah, C. Petorak, B. Thompson, and R. W. Trice, "Cyclic Ablation of High-Emissivity Sm-doped ZrB<sub>2</sub>-SiC Coatings on Alumina Substrates," *Journal of the European Ceramics Society*, **38** 1136-1142 (2018).
- <sup>47</sup> L. Liu, Z. Ma, Z. Yan, S. Zhu, and L. Gao, "ZrO<sub>2</sub> Formation in ZrB<sub>2</sub>/SiC Composite Irradiated by Laser," *Materials*, **8** 8745-8750 (2015).

- <sup>48</sup> D. D. Jayaseelan, E. Zapata-Solvas, C. M. Carney, A. Katz, P. Brown, and W. E. Lee, "Microstructural Evolution of HfB<sub>2</sub> Based Ceramics During Oxidation at 1600-2000°C," *Journal of Advances in Applied Ceramics*, **114** 277-295 (2015).
- <sup>49</sup> F. Monteverde, D. Alfano, and R. Savino, "Effects of LaB<sub>6</sub> Addition on Arc-Jet Convectively Heated SiC-Containing ZrB<sub>2</sub>-Based Ultra-High Temperature Ceramics in High Enthalpy Supersonic Airflows," *Corrosion Science*, **75** 443-453 (2013).
- <sup>50</sup> A. R. Mallick, S. Schakraborty, and P. K. Das, "Synthesis and consolidation of ZrC based ceramics: A review," *Review of Advanced Material Science*, **44** 109-133 (2016).
- <sup>51</sup> F. Incropera, D. Dewitt, T. Bergman, and A. Lavine, "Fundamentals of Heat and Mass Transfer" John-Wiley and Sons, Incorporated (2007).
- <sup>52</sup> S. Guo, C. Lai, T. Jones, M. Oldfield, G. Lock, and A. Rawlinson, "Influence of Surface Roughness on Heat Transfer and Effectiveness for a Fully Film Cooled Nozzle Guide Vane Measured by Wide Band Liquid Crystals and Direct Heat Flux Gages," *Journal of Turbomachinery*, **122** 709-716 (2000).
- <sup>53</sup> D. Michel, Y. Rouaux, M. Perez, Y. Jorba, *Journal of Materials Science*, **15** 61-66 (1980).
- <sup>54</sup> S. Shimada, "A Thermoanalytical Study on the Oxidation of ZrC and HfC Powders with the Formation of Carbon," *Solid State Ionics* **149** 319-226 (2002).
- <sup>55</sup> H. Liu, J. Liu, H. T. Liu, and G. Zhang, "Changed Oxidation Behavior of ZrB<sub>2</sub>-SiC Ceramics with the Addition of ZrC," *Ceramics International*, **41** 8247-8251 (2015).
- <sup>56</sup> K. Li, X. Jing, F. Quian-gang, L. He-jun, and G. Ling-jun, "Effects of Porous C/C Density on the Densification Behavior and Ablation Property of C/C-ZrC-SiC Composites," *Carbon*, **57** 161-168 (2013).
- <sup>57</sup> J. Han, P. Hu, X. Zhang, and S. Meng, "Oxidation Behavior of Zirconium Diboride-Silicon Carbide at 1800°C," *Scripta Materialia*, **57** 825-828 (2007).
- <sup>58</sup> D. Gao, Y. Ahang, J. Fu, C. Xu, Y. Song, and X. Shi, "Oxidation of Zirconium Diboride-Silicon Carbide Ceramics Under an Oxygen Partial Pressure of 200 Pa: Formation of Zircon," *Corrosion Science*, **52** 3297-3303 (2010).
- <sup>59</sup> C. H. Liebert, "Emittance and Adsorption of NASA Ceramic Thermal Barrier Coating System," Lewis Research Center, Cleveland, OH, NASA TP 1190c.1 (1978).

- <sup>60</sup> J. I. Eldridge, and C. M. Spruckler, "Determination of Scattering and Absorption Coefficients for Plasma-Sprayed Ytria-Stabilized Zirconia Thermal Barrier Coatings at Elevated Temperatures," *Journal of the American Ceramic Society*, **92** [10] 2276-2285 (2009).
- <sup>61</sup> V. Y. Chekhovskoi, V. D. Tarasov, and N. V. Grigor'eva, "The Spectral Emissivity of an Oxide Film of Zirconium for Wavelengths of 530 and 650 nm in the Temperature Range of 1450-1750 K," *High Temperature*, **42**[2] 252-258 (2004).
- <sup>62</sup> M. Bengisu, "Engineering Ceramics," *Springer* (2001).
- <sup>63</sup> Z.G. Liu, J. H. Ouyang, B. H. Wang, Y. Zhou, and J. Li, "Thermal Expansion and Thermal Conductivity of  $\text{Sm}_x\text{Zr}_{1-x}\text{O}_{2-x/2}$  (0.1-0.5) Ceramics," *Ceramics International*, **35** 791-796, (2009).
- <sup>64</sup> J. Fenech, M. Dalbin, A. Barnabe, J. P. Bonino, and F. Ansart, "Sol-gel Processing and Characterization of (RE-Y)-Zirconia Powders for Thermal Barrier Coatings," *Powder Technology*, **208** 480-487, (2011).
- <sup>65</sup> K. Sendur, "Patterned Surface Roughness Effects in Reflectivity and Emissivity in  $\text{ZrB}_2$ ," *unpublished work* (2018).
- <sup>66</sup> Y.Cengel, "Heat and Mass Transfer," *New York: Mc Graw Hill*, 2007.

## VITA

Anneliese Emma (Laskowski) Brenner was born April 22, 1993 and was mainly raised in Foster, WI. She completed her primary education at Osseo-Fairchild High School in Osseo, WI. Anneliese continued to get her bachelor's degree in Materials Science at the University of Wisconsin-Eau Claire. She then moved to Lafayette, IN to attend Purdue University for her Doctor of Philosophy in Materials Engineering earned in May 2019. As a graduate student Anneliese was involved in the Purdue Graduate Student Government as a senator as well as sat on the recruitment committee for Materials Science and Engineering Purdue Graduate Student Government. She was also heavily involved with the President's Council of Student Advisors for the American Ceramic Society where she sat on both the finance committee and programming committee where she helped plan and run several student competitions and promoted ceramic research.

## PUBLICATIONS

- <sup>1</sup> W. Tan, M. Adducci, C. Petorak, A. E. Brenner, and R. W. Trice, “Effect of Rare-Earth Dopant (Sm) Concentration on Total Hemispherical Emissivity and Ablation Resistance of ZrB<sub>2</sub>/SiC Coatings,” *Journal of the European Ceramic Society*, 1–9 (2016).
- <sup>2</sup> A. E. Brenner, A. A. Peña, X. L. Phuah, C. Petorak, B. Thompson, and R. W. Trice, “Cyclic Ablation of High-Emissivity Sm-doped ZrB<sub>2</sub>-SiC Coatings on Alumina Substrates,” *Journal of the European Ceramics Society*, **38** 1136-1142 (2018).
- <sup>3</sup> A.E. Brenner, and R. W. Trice, “In-Situ Oxide Scale Investigation of Sm-Doped ZrB<sub>2</sub>/SiC Billets,” in preparation.
- <sup>4</sup> A.E. Brenner, J. P. Vernon, J. Pitz, and R. W. Trice, “Microstructural Effects on Ablation and Emittance Behavior of Sm-doped ZrB<sub>2</sub>/SiC Ceramics,” in preparation.